Arthur Alencastro Puls

Unveiling Fluorine Abundances in the Milky Way

Revelando Abundâncias de Flúor na Via Láctea

MSc dissertation taken under the supervision of Dr. Alan Alves Brito, submitted to the Graduate Program of Instituto de Física – Universidade Federal do Rio Grande do Sul (UFRGS) as part of the fulfillment to obtain the master's degree in physics with emphasis in astrophysics.

Universidade Federal do Rio Grande do Sul

Instituto de Física

Departamento de Astronomia

Porto Alegre, RS, Brasil

2018

*This work has received financial support from Conselho Nacional de Desenvolvimento Científico e Tecnológico (CNPq) and from Coordenação de Aperfeiçoamento de Pessoal de Nível Superior (CAPES).

Acknowledgements

To my supervisor, Dr. Alan Alves Brito, who has been supervising my work since the second year of my undergraduate course, for the intellectual and professional support.

To our collaborators, Dr. David Yong and Dr. Amanda Karakas, as well as my colleague Gustavo Ourique, for help with productive ideas, suggestions and references.

To all the people in the UFRGS Astronomy Department, for the excellent and productive environment.

To my family, particularly grandma Saly, for the love and logistic support.

Last but not least, to my lifemate Gabriela Gehlen, with whom I am sharing intense years (and nights full of academic work).

'Our posturings, our imagined self-importance, the delusion that we have some privileged position in the Universe, are challenged by this point of pale light. Our planet is a lonely speck in the great enveloping cosmic dark. In our obscurity, in all this vastness, there is no hint that help will come from elsewhere to save us from ourselves. The Earth is the only world known so far to harbor life. There is nowhere else, at least in the near future, to which our species could migrate. Visit, yes. Settle, not yet. Like it or not, for the moment the Earth is where we make our stand.'

Carl Sagan – Pale Blue Dot

Abstract

The element Fluorine has several proposed sites of nucleosynthesis, and the main discussed ones are: (1) stars of the Asymptotic Giant Branch, (2) Wolf-Rayet stars and (3) Type II Supernovae. Observational measurements of its abundances and theoretical predictions in the context of the chemical evolution of the Galaxy have been carried out in the last three decades, but the contributions from each of the proposed sites are not clear yet. The most up-to-date models show some disagreement with the observations. We make a detailed chemical analysis – divided in three parts – of a sample of stars through measurements of Fluorine and several other chemical species in their atmospheres. First, we explore the chemistry of giants located in the outer disc of the Milky Way and, for the first time, Fluorine abundances were measured in this region of the Galaxy. Also, we are taking advantage of the assumption of chemical homogeneity (at least to the 0.1 dex level) of the Hyades open cluster to evaluate if the adopted models are well calibrated for K-dwarfs. Finally, a chemical analysis of objects with peculiar composition give results useful to – in the near future – constrain nucleosynthesis models. The entire sample consists of K-dwarfs from the Hyades open cluster, normal cool giants from the Galactic outer disc, barium stars, CH stars and Carbon Enhanced Metal Poor stars. We are using high-resolution (R $\sim$ 25000), high signal-to-noise ratio (> 150) infrared spectra of 25 targets, obtained with NIRSPEC on the 10-m Keck II Telescope. A full 1D-LTE spectrum synthesis using Kurucz stellar atmospheres is carried out to infer the chemical abundances. Also, we employ astrometry from Gaia DR2 to check the kinematics of the targets. For the outer disc, our results suggest a smaller slope in the F versus O plot, which would imply a different chemical enrichment of Fluorine in this region of the Galaxy. On the other hand, our results for the F versus Fe plot suggest that the relationship between these elements in the outer disc is similar to that found in the solar neighbourhood. In the Hyades an unexpected star-to-star spread is found for several elements, including Fluorine. We investigate the role of the adopted atmospheric parameters in these results. Fluorine is detected only in two of the peculiar objects. For some of these stars, models of chemical pollution available in the literature are fitted to the observations. More observations are needed in the outer disc to investigate the suggestion of different chemical evolution in this region, at least for Fluorine. Further studies of cool dwarfs in open clusters will put our unexpected results for the Hyades in context. Finally, our results for stars with peculiar chemstry will help to fine tune models of stellar evolution, nucleosynthesis and binary systems.

Keywords: Fluorine. The Galaxy. Chemical Abundances.

Resumo

O elemento Flúor possui vários sítios de nucleossíntese propostos, e os mais discutidos são: (1) estrelas do ramo assintótico das gigantes, (2) estrelas Wolf-Rayet e (3) Supernovas do Tipo II. Medições observacionais de suas abundâncias e previsões teóricas no contexto da evolução química da Galáxia foram realizadas nas últimas três décadas, mas as contribuições de cada um dos sítios propostos ainda não estão claras. Os modelos mais atualizados mostram algum desacordo com as observações. Fazemos uma análise química detalhada – dividida em três partes – de uma amostra de estrelas através de medições de Flúor e várias outras espécies químicas em suas atmosferas. Primeiro, exploramos a química de estrelas gigantes localizadas no disco externo da Via Láctea e, pela primeira vez, abundâncias de Flúor foram medidas nesta região da Galáxia. Além disso, estamos aproveitando a suposição de homogeneidade química (pelo menos para o nível de 0,1 dex) do aglomerado aberto Híades para avaliar se os modelos adotados estão bem calibrados para estrelas anãs do tipo K. Finalmente, uma análise química de objetos com composição peculiar fornece resultados úteis para – em um futuro próximo – restringir modelos de nucleossíntese. A amostra inteira consiste de anãs K do aglomerado aberto de Híades, gigantes frias normais do disco externo Galáctico, estrelas de bário, estrelas CH e estrelas Pobres em Metais Ricas em Carbono. Estamos usando espectros no infravermelho em alta resolução (R $\sim$ 25000) e alta razão sinal/ruído ($>$ 150) de 25 alvos, obtidos com o NIRSPEC no Telescópio Keck II de 10-m. Uma síntese completa do espectro 1D-LTE usando atmosferas estelares de Kurucz é realizada para inferir as abundâncias químicas. Além disso, empregamos astrometria do Gaia DR2 para verificar a cinemática dos alvos. Para o disco externo, nossos resultados sugerem uma inclinação menor na relação F versus O, o que implicaria um enriquecimento químico diferente do Flúor nessa região da Galáxia. Por outro lado, nossos resultados para a relação F versus Fe sugerem que a relação entre esses elementos no disco externo é semelhante àquela encontrada na vizinhança solar. No Híades, um espalhamento estrela-a-estrela inesperado é encontrado em vários elementos, incluindo o Flúor. Investigamos o papel nesses resultados dos parâmetros atmosféricos adotados. O Flúor é detectado apenas em dois dos objetos peculiares. Para algumas dessas estrelas, modelos de poluição química disponíveis na literatura são ajustados às observações. Mais observações são necessárias no disco externo para investigar a sugestão de evolução química diferente nessa região, pelo menos para o Flúor. Novos estudos de anãs frias em aglomerados abertos colocarão nossos resultados inesperados no Híades em contexto. Finalmente, nossos resultados para estrelas com química peculiar ajudarão a refinar modelos de evolução estelar, nucleossíntese e sistemas binários.

Palavras-chave: Flúor. A Galáxia. Abundâncias Químicas.

List of Figures

List of Tables

List of abbreviations and acronyms

2MASS	2 Micron All-Sky Survey
ΛCDM	Lambda Cold Dark Matter
AGB	Asymptotic Giant Branch
TP-AGB	Thermal Pulse Asymptotic Giant Branch
ASCII	American Standard Code for Information Interchange
BD	Bonner Durchmusterung (catalog)
BF	Birthrate Function
CEMP	Carbon Extreme Metal-Poor
CNO	Carbon Nitrogen Oxygen
DR2	Data Release 2
FWHM	Full width at half-maximum
FGKM	Set of spectral types F, G, K and M
HD	Henry Draper (catalog)
HE	Hamburg/ESO Survey
HIP	Hipparcos (catalog)
HR	Hoffleit Bright (catalog)
IMF	Initial Mass Function
IRAF	Image Reduction and Analysis Facility
LTE	Local Thermodynamic Equilibrium
M 67	Messier 67
MCMC	Markov Chain Monte Carlo
NIRSPEC	Near InfRared echelle SPECtrograph
NSDRP	NIRSPEC Data Reduction Pipeline

RGB	Red Giant Branch
RMS	Root Mean Square
SFR	Star Formation Rate
SGB	Sub-Giant Branch
SNe	Supernovae
SN1987A	Supernova 1987A
WD	White Dwarf
WR	Wolf-Rayet

List of symbols

α	alpha element set; alpha particle; linear absorption coefficient; angle of incidence of light beam
β	diffraction angle
β^+	positron
γ	photon; damping constant; tilt angle
λ	wavelength
κ	mass absorption coefficient
μ_α,μ_δ	proper motion
ν	neutrino
ϖ	parallax
ρ	mass density
τ	optical depth
Θ_B	blaze angle
ν_e	electron neutrino
A_t,A_c	airmass
A_V	reddening
$A(X)$	chemical abundance of species X
$A(X)_\odot$	solar chemical abundance of species X
e	orbital ellipticity
$\mathcal{F}$	total flux
f(m)	binary mass function
g	surface gravity
Gyr	10^9 years
I,I_ν,I_λ	specific intensity

j	emission coefficient
k_B	Boltzmann constant
L	Luminosity
m	spectral order
M	mass
M	absolute magnitude
$\mathrm{M}_\odot$	solar mass
n	neutron
N_X	particle number density of species X
p	proton
P	orbital period
R	spectral resolution
s	scale factor
S_ν	source function
$\mathrm{T}_{\mathrm{eff}}$	effective temperature
v_t	microturbulence
V,J,H,K	V-, J-, H- and K-band apparent magnitude
X	when in square brackets – [X] – the quantity X is represented w.r.t. its respective solar quantity in logarithmic scale
Z	global metallicity

Contents

1 Introduction

The evolution of the field of Astrophysics has brought to us a massive amount of information in the last century. Among all this information, one of the most spectacular is the knowledge that almost all chemical elements are made inside the stars, in their dramatic deaths, or, even, in cataclysmic collisions of compact objects (Burbidge et al., 1957; Drout et al., 2017). Apart from the primordial Hydrogen, Helium and Lithium produced in the Big Bang, nearly all the heavier elements[1] have been created by successive generations of stars, whose death processes enrich the interstellar medium with processed material (see, e.g., Wheeler, Sneden & Truran Jr. (1989) and Matteucci (2012)). The observed abundances of the lightest elements indeed confirm the quantities predicted by the ΛCDM model for the contemporary Universe, this result being one of the strongest evidences for the Big Bang theory (Coc; Vangioni, 2017).

In the context of the Milky Way Galaxy (hereafter, the Galaxy), the determination of chemical abundances sheds light on its evolution and structure. This happens because each of the identified (baryonic) Galactic structures – Halo, Bulge, and the two components of the Disc, Thin and Thick Disc – have different chemical, kinematical, among others, signatures (see, e.g., the review of McWilliam (1997)).

For instance, in the Halo (see Fig. 1 for a schematic view of the Galaxy), stars are poor in metals (elements heavier than Helium) and present a chemical composition that, when studied in detail, suggests a series of accretion events of dwarf galaxies, confirmed by several kinematic analysis (Bland-Hawthorn; Gerhard, 2016). The Bulge has chemical patterns that suggest a fast star formation rate, a vertical gradient in Fe (McWilliam, 2016) and a complex internal structure (see Barbuy, Chiappini & Gerhard (2018) for an up-to-date review), discovered despite the observational challenges that arise on the direction of the Galactic centre due to interstellar extinction. Also, a chemical continuity between the Bulge and the Thick Disc has been suggested (Alves-Brito et al., 2010).

In the chemistry of the Galactic disc there is a clear separation in two distinct structures (e.g., Fuhrmann (2011)), which seems to correlate with kinematic properties (Gratton et al., 2000), although the claim that this separation is discrete is in dispute (Bovy; Rix; Hogg, 2012). One structure, the Thick Disc, is older, with enhancement in the so-called α-elements (O, Mg, Si, Ca, Ti) w.r.t. the Sun. The other structure, the Thin Disc, is kinematically colder, more metal-rich, less α-enhanced and seems to be younger than the Thick Disc (Bensby; Feltzing; Oey, 2014). A phase transition between the Thick and Thin Discs is suggested to have occurred around 8 Gyr ago – see, e.g., Linden et al.

---

[1] More precisely, those with atomic number $Z \geq 6$.

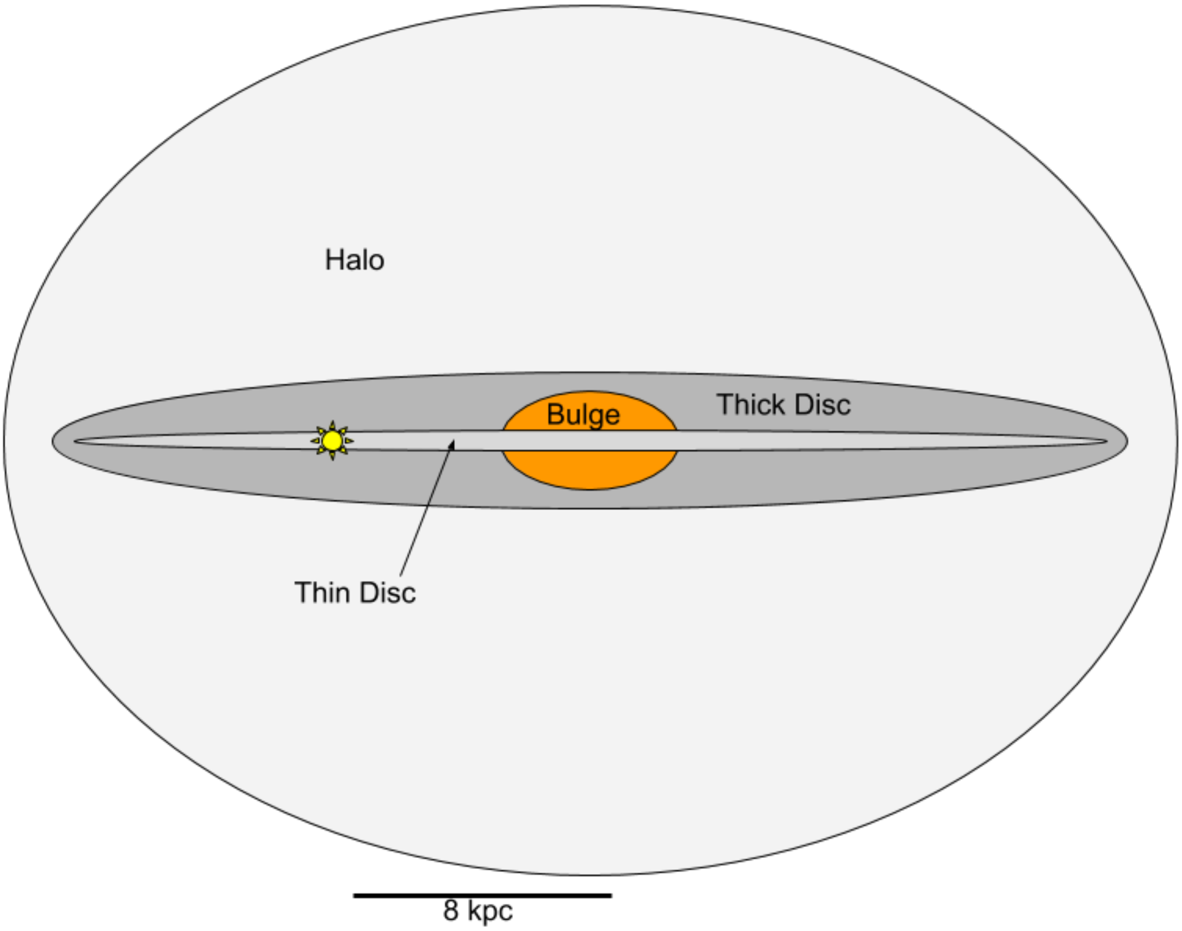

Figure 1 – Schematic view of the Galaxy, edge-on, with its main components represented. The yellow star gives the approximate position of the Sun, with a scale for a rough reference.

(2017), who uses the age and chemistry of open clusters as tracers.

At this point, a first-time reader may be asking: how do qualitative conclusions are taken from quantitative chemical abundance measurements? The answer is that we rely on models of Galactic chemical evolution, which are constrained by observations. According to Matteucci (2012), the basic concepts for a model describing chemical evolution of galaxies are:

- The birthrate function (BF), which describes how fast the stellar generations renew themselves and how massive the stars of a newborn group are. In its turn, the BF is composed by other functions – the star formation rate (SFR) and the initial mass function (IMF). The SFR is usually defined as a function of time, gas density and empirically adjustable parameters. Meanwhile, the IMF gives the distribution of mass of a newly formed stellar population. The first model for an IMF was proposed by

Salpeter (1955), consisting in a simple power law with the form $p(m)\mathrm{d}m \propto m^{-\alpha}\mathrm{d}m$, where m is stellar mass and α is constant, implying that low-mass stars are much more common. Later, other authors introduced corrections in the lower mass range (< 1 $\mathrm{M}_\odot$) because Saltpeter's IMF seems to overpredict the number of low mass stars. Among the most commonly used low-mass-corrected IMF are those from Kroupa (2001) – which, for masses lower than 0.5 solar masses, uses smaller (constant) values of α than the 2.3 given by Salpeter – and Chabrier (2003), which, contrary to Kroupa, employs a smooth correction for Salpeter IMF for masses lower than one solar mass. Also, Chabrier presents IMF for individual stars and binary systems separately.

- Stellar yields: the sum of pre-existing and processed quantities of chemical elements released by stars into the interstellar medium. The yields are required to evolve the chemistry of the system of interest, because the elements processed by the previous generations feed the gas where the newer stellar generations are formed. Their net quantities may be both positive or negative – stellar yields are negative for elements whose destruction by nuclear reactions is surpassed by creation from other nuclear reactions, giving a negative net result. For instance, the net yield of H is negative, and usual star formation is expected to end in 10^{14} years due to exhaustion of the interstellar H (Adams; Laughlin, 1997). The stellar yields depend on stellar structure (defined by the initial mass of the star and metallicity – see, e.g., Salaris & Cassisi (2005)), as the nuclear reactions which process the chemical elements are dependent on quantities such as temperature and pressure (Clayton, 1983). Also, initial mass (and, in second order, metallicity) define how the stars die, and, by consequence, how and what elements are released in the interstellar medium[2].

- Gas flows: a simple closed-box model for galactic chemical evolution, where an initially pristine gas has evolved homogeneously as a closed system through series of stellar generations with constant IMF (Tinsley, 1980), despite being didactic and analytically simple, underpredicts the observed quantity of metal-poor G-dwarfs – which is the classical G-dwarf problem, now 'GKM-dwarf problem', see Woolf & West (2012). Thus, a model needs to account for gas inflows and outflows, as well as internal (radial) flows. Inflow/outflow of pre-enriched gas may explain the observed lack of metal-poor stars in comparison with what it is predicted by a closed-box model. Radial gas flows may play a role in chemical gradients, but with a final result dependent on the SFR, and the interaction between radial flows and SFR do not seem to be trivial (Edmunds; Greenhow, 1995). The double gas infall model was introduced by Chiappini, Matteucci & Gratton (1997) to explain the different timescales, and, hence, different chemical evolution, involved in the formation of Thick and Thin discs.

---

[2] Here, we are considering single stellar evolution.

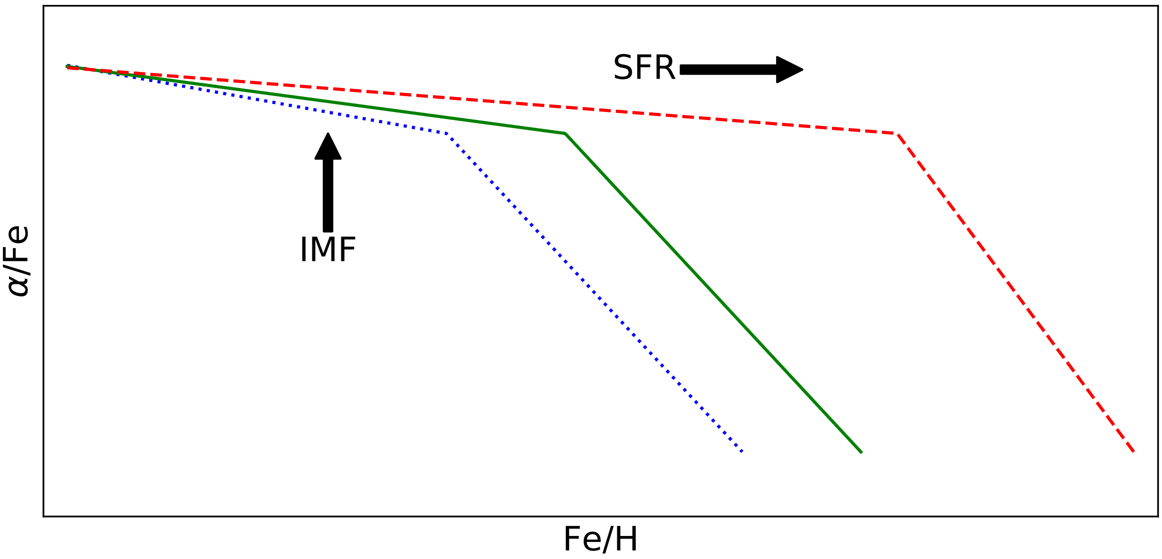

Figure 2 – The α-elements vs Fe space, which can be used as diagnostic plot (see text for discussion). *Blue dotted line*: Abundance trend typical of dwarf galaxies. *Green solid line*: The same, but for the solar neighbourhood. *Red dashed line*: galactic bulges and elliptical galaxies. Abscissae increase from left to right and ordinates increase from bottom to top. Adapted from McWilliam (2016) and Matteucci & Brocato (1990).

Also crucial for galactic chemical evolution models are the stellar evolution and nucleosynthesis models. Their immediate impact are on stellar yields, as discussed above. When analysed in detail and put in galactic context, stellar nucleosynthesis may unveil some interesting information. For instance, a classical result is the 'α-Fe knee', illustrated in Fig. 2, which describes the relation between α elements such as O and Mg with Fe. In Type II Supernovae (SNe) occur the bulk of production of cosmic O and Mg, in quiescent hydrostatic burning, while the net production of Fe comes mostly from Type Ia SNe (Woosley; Weaver, 1995; Woosley; Heger; Weaver, 2002; Nomoto; Kobayashi; Tominaga, 2013). Due to the faster evolution of the massive stars which die as Type II SNe – Type Ia SNe need a pair of evolved low-mass stars (Salaris; Cassisi, 2005) – and to the fact that Type II SNe Fe yields are independent from the initial mass of the star for a given metallicity (see, e.g., the results from Kobayashi et al. (2006)), the ratio α/Fe will take some time to decrease through the evolution of the Galaxy. Thus, in a first approximation, older stars tend to have a higher α/Fe ratio. If star formation occurs at a relatively fast rate, the succesive generations of stars will have their Type II SNe enriching the interstellar medium with metals before the very first Type Ia SN explodes. On the other hand, if the SFR is slow, Type Ia SNe will enrich the medium with their progeny at a relatively low metallicity. Thus, the position of the knee in the α-Fe plot traces the SFR of a galaxy or a galactic component, as first predicted by Matteucci & Brocato (1990). The IMF may be traced through this plot as well, because in general the yields of the α-elements in Type II SNe increase with mass. Hence, the α/Fe ratio in the low metallicity plateau is sensitive to the initial mass distribution of the stars. A higher plateau will imply a more top-heavy IMF, i.e., an IMF where a high-mass star has a greater probability of formation, while a lower plateau implies a bottom-heavy IMF.

1.1 Fluorine

The light element Fluorine, atomic number Z = 9, is stable as only one isotope, ^{19}F. Its unstable isotopes with the longest half-lives are ^{18}F ($\approx$ 110 minutes) and ^{17}F ($\approx$ 1 minute), both decaying by positron emission (Audi et al., 2003). F[3] atomic mass is A = 18.998403 amu (Laeter et al., 2003).

Denoting N_X as the number density of element X, we define the abundance $A(X)$ of a given element as $A(X) = \log N_X/N_H + 12$, i.e., a logarithmic scale where the abundance of Hydrogen is 12 dex. This definition will be adopted from now on. The solar abundance $A(F)_\odot$ is 4.56 ± 0.3 dex according to Grevesse & Sauval (1998), with the more recent review of Asplund et al. (2009) giving the same value for photospheric abundance and reporting the Solar System meteoritic abundance of 4.42 ± 0.06 dex from Lodders, Palme & Gail (2009). In this work, we will adopt the solar value $A(F)_\odot = 4.40 \pm 0.25$ found by Maiorca et al. (2014) through measurements of several lines in the spectrum of a sunspot, because it has the best agreement with the meteoritic abundance. For the other elements analysed in this work, the solar abundances adopted are those from Asplund et al. (2009).

In the solar atmospheric composition, the abundance of F is rather low when compared with chemical elements having similar atomic numbers. For instance, each of the CNO elements, and Ne as well, is more abundant than F in the Sun by 3-4 orders of magnitude ($A(X) > 7.5$, see Fig. 3). The reason for this relative underabundance is that F is bypassed in common chains of nucleosynthesis – e.g., a simple proton-capture of the most common isotope of Oxygen, ^{16}O, creates the unstable ^{17}F. The CNO cycle creates F isotopes in some of its loops, but none of them are the stable ^{19}F. On the other hand, the stable ^{15}N appears in the CNO-cycle (Clayton, 1983), and the capture of an α particle by this isotope creates ^{19}F, but the accumulation of the transmuted element depends on the environment where the reaction takes place, as will be discussed ahead.

The observation of the neutrino burst coming from the supernova SN1987A (Bionta et al., 1987; Hirata et al., 1987) triggered new science, including the hypothesis that F may be produced in SNe explosions through neutrino spallation (Woosley; Haxton, 1988). The huge amount of neutrinos released by the supernova would counterbalance the tiny

---

[3] Hereafter, for ’F’ we mean ^{19}F, unless the isotope is explicitly identified.

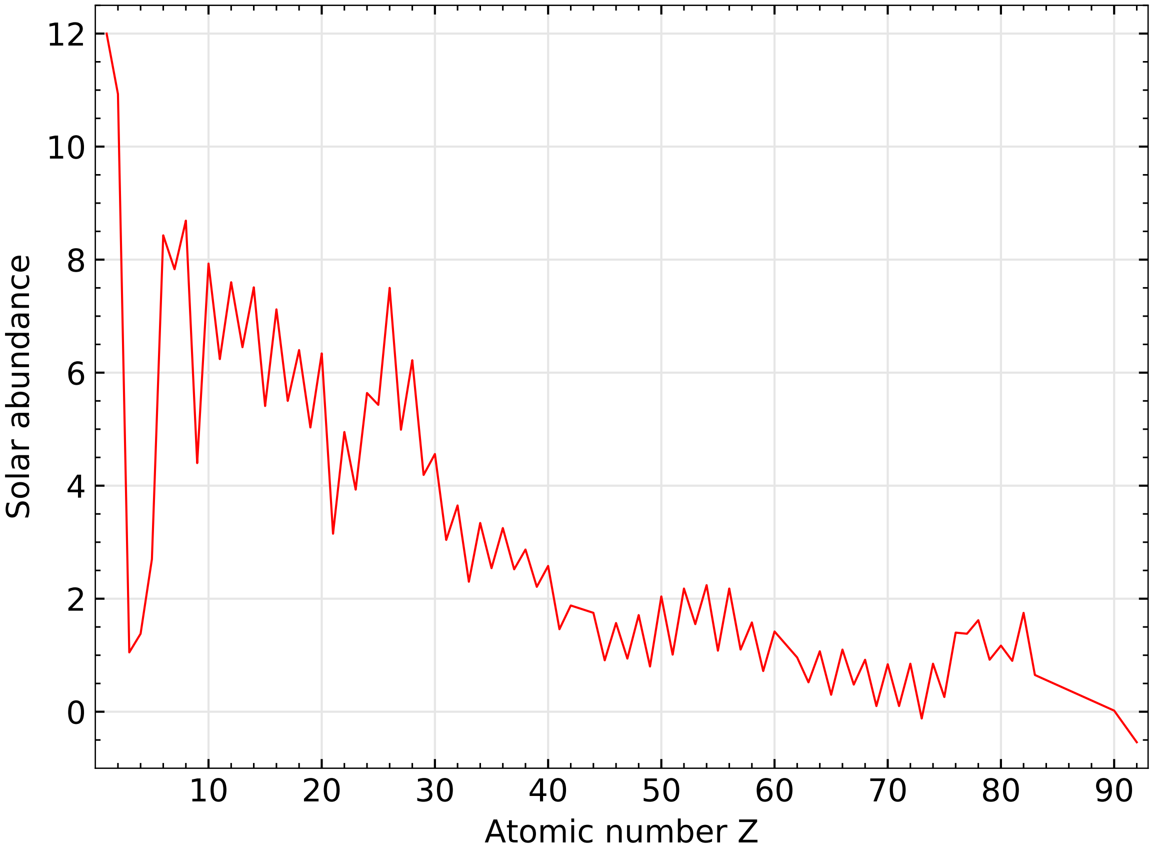

Figure 3 – Abundance of chemical elements in the solar system in the scale of $A(X) = \log N_X/N_H + 12$. The abundances are photospheric – in the abscence of photospheric values, meteoritic abundances were plotted (Asplund et al., 2009; Maiorca et al., 2014). Notice the relative low abundance of F (Z = 9).

cross-section of the particle, paving the way for the so called ν-process: a neutrino would be scattered by a ^{20}Ne from the Ne shell of the exploding star. The interaction would result in energy transfer from the neutrino to the Ne nucleus, generating an excited state ^{20}Ne*, with one possible outcome being a proton decay into ^{19}F. Another possible outcome would be a neutron decay of ^{20}Ne* into ^{19}Ne, an unstable isotope which would then suffer β-decay into ^{19}F. Woosley & Haxton, after taking into account possible ^{19}F destruction channels, concluded that the ν-process could account for the Galactic F abundance.

However, four years later on, the pioneering work from Jorissen, Smith & Lambert (1992) – the first reliable measurements of F outside the Solar System – found evidence of F nucleosynthesis in the interior of evolved intermediate-mass stars, more precisely in stars from the asymptotic giant branch (AGB). They measured normal K giants – cool giants which have not started to burn He in their cores yet, Ba-stars – characterized by strong Ba II absorption lines – and AGB stars (see a more in-depth description of AGB stars ahead) of different classes regarding atmospheric Carbon abundances (M, MS, S, SC, C-N and C-J) and found that stars experiencing thermal pulses (TP-AGB), i.e., those in more evolved stages and affected by the third dredge-up, had much higher F abundances – 30 times the solar value. A correlation between F and C was found as well, indicating that the atmospheric enrichment of F in evolved stars may be caused by the same mechanism that brings C to the outer layers of the star. This also points the nucleosyhtesis site to some layer in and/or between the He- and H-burning shells (see discussion ahead). Their work also found overabundance of F in Ba-stars. Coupled with the evidence for AGB nucleosynthesis of F, this result suggests, as the authors argued, that mass transfer from a former AGB companion is the source of the peculiar composition of Ba-stars.

Later, Meynet & Arnould (2000) suggested that a non-negligible quantity of cosmic F may be produced in Wolf-Rayet (WR) stars. WR stars are massive (> 10 M$_\odot$) stars, evolved from O-type main-sequence stars, which present broad emission lines due to strong stellar winds (Crowther, 2007). One branch of the CNO cycle produces and destroys F in massive stars by ^{18}O(p,γ)^{19}F(p,α)^{16}O, giving a zero net result. Nevertheless, Meynet & Arnould proposed F production by WR stars in the early phase of core *He* burning, in a chain reaction starting with ^{14}N(α,γ)^{18}F. The ^{18}F may suffer β-decay, and it is also possible that it captures a neutron or a proton. Both three possibilities may result in chain reactions leading to ^{19}F, but the authors argue that the timescale of the β-decay is several orders of magnitude faster. Thus, the preferred reaction path is ^{18}F($\beta^{+}\nu_e$)^{18}O(p,α)^{15}N(α,γ)^{19}F. This reaction chain needs a source of protons, provided by ^{14}N(n,p)^{14}C, which itself needs a source of neutrons, guaranteed by ^{13}C(α,n)^{16}O. However, in a later evolutionary stage, the ^{19}F(α,p)^{22}Ne reaction becomes efficient, destroying F. The proposed solution is that the created F is carried away by its stellar winds before total destruction of this chemical species takes place, polluting the interstellar medium with this element. Also, Meynet & Arnould made a rough estimation that WR stars may account for most of the solar system F, but one must be careful with this conclusion, because the calculations were made from rather uncertain F yields and performed with a simple, closed-box model of Galactic chemical evolution.

Despite the other proposed sites, as far as we are concerned the only observed production site of F are AGB stars. Thus, let's take a more detailed look at these objects. Complete descriptions on the topics covered in the next paragraphs may be found in Kippenhahn & Weigert (1990), Salaris & Cassisi (2005) and in the review from Karakas & Lattanzio (2014).

AGB stars are evolved low- and intermediate-mass[4] stars whose lower initial mass limit is ~ 0.8 M$_\odot$. The upper mass limit varies between ~ 7 M$_\odot$ and ~ 10 M$_\odot$, depending

---

[4] The adopted criterion is the mass limit for the He-flash. Low-mass stars experience He-flash at the end of the Red Giant Branch, while intermediate-mass stars do not. For solar metallicity, the mass limit is ~ 2.2 M$_\odot$.

on chemical composition and if we also consider stars which experience core C burning without exploding as core-collapse SNe (i.e., that go through the super-AGB phase). For the purpose of this work, we will focus on those stars which end their lives as C-O white dwarfs after the AGB phase (i.e., those not experiencing the super-AGB phase). The stars that eventually evolve into the AGB begin their lives, as usual, burning H into He in their cores, in the main-sequence phase. From a certain metallicity-dependent mass threshold onwards – 1.3 $M_\odot$ for solar metallicity, their H fusion becomes dominated by the CNO cycle instead of the p-p chain. After leaving the main-sequence, the star passes through the Sub-Giant Branch (SGB) and reaches the Red Giant Branch (RGB) burning H in a thin shell around the core, and experiencing its first mixing events (first dredge-up; also non-convective extra mixing for those objects in the low-mass range). These events alter mostly the proportions of He, Na and CNO isotopes in their atmospheres, and the mixing effect is stronger in more massive pre-AGB stars[5]. After the RGB, the star burns He through the triple-α reaction, accumulating C and O in its core.

The star reaches the AGB after the exhaustion of He in its core, and He-burning continues in a shell around it. Most intermeadiate-mass stars experience a second mixing event (second dredge-up) in the early-AGB phase through the penetration of the convective zone into the H-depleted region, affecting C, N, He and H surface abundances. At this point, the internal structure of the star may be summed up as: an inert C-O core; a thin shell where He burns in triple-α; an He-rich intershell region with processed material from H burning; the H-burning shell, mostly inactive; and the H-rich envelope. The He-burning shell then shuts down after approaching the H-He border. Hence, the star contracts, and this contraction leads to an increase in temperature and pressure in the H-burning shell, which becomes fully efficient again. The processed material begins to accumulate on top of the C-O core and the triple-α reignites in thermonuclear runaway mode, generating the *thermal pulse*. A massive amount of energy is released because the geometric thickness of the He burning shell is so small that an expansion of the shell induces an increase in temperature, and H-burning shuts down again. The thermonuclear runaway mode turns into quiescent burning after the He-shell expands to a critical thickness where the expansion induces a decrease in temperature, and the process is repeated several times while the envelope has enough mass. It is the TP-AGB phase.

The TP-AGB phase is of great interest here because the shutting down of H-burning after He-burning reignition allows the convective zone to expand inwards, deep into the intershell. The processed material from this region – C, F, s-process elements, among others – is then mixed by convection and goes up to the surface in the so-called third dredge-up. This mechanism is responsible for the formation of intrinsic Carbon stars[6]. Its efficiency

---

[5] The description is not appropriate for metal-poor intermediate-mass stars. In these stars, the conditions for He-burning are reached before the RGB, and, thus, they do not experience the first dredge-up.

[6] The *extrinsic* Carbon stars are believed to acquire their chemistry through mass transfer from an AGB

depends on metallicty – what makes AGB yields metallicity-dependent. The dredged up material is expelled through the mass loss, which is strong in the AGB phase. More massive ($M > 5\ M_\odot$) AGB stars experience the so-called *hot bottom burning*, whose main result is to prevent the formation of Carbon stars, as a large quantity of C is converted in N through the CN cycle.

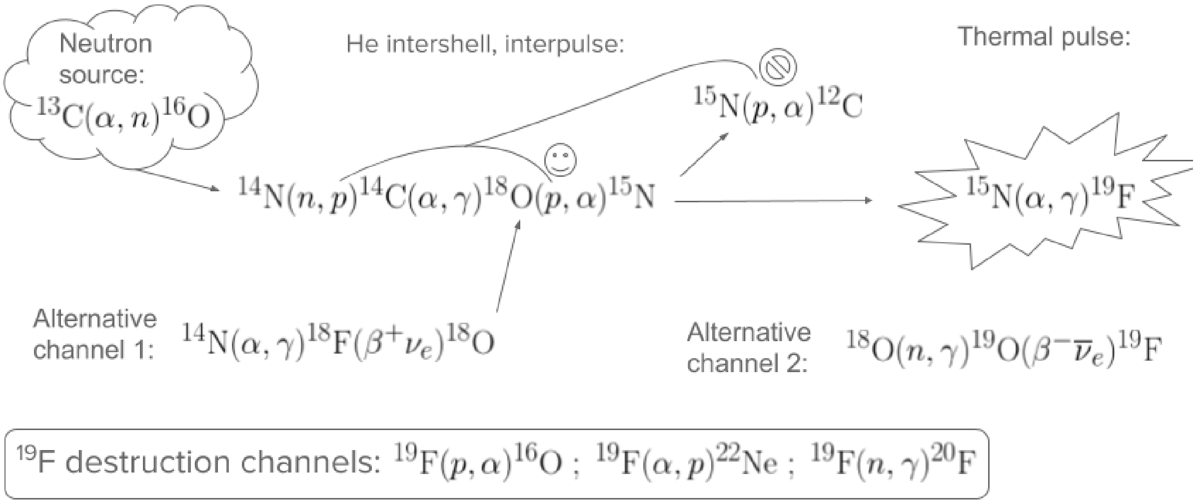

Figure 4 – Nuclear paths leading to the production of F in AGB stars according to Cristallo et al. (2014).

Cristallo et al. (2014) describe the reaction chain leading to F in AGB stars as ’quite complex’. Although their work focus on the F nucleosynthesis in AGB stars with a particular metallicity (global metallicity Z=0.001)[7], one may get the big picture from their description. A schematic view of the reaction path is shown in Fig. 4. The slowest reaction of the CNO cycle is $^{14}N(p,\gamma)^{15}O$ (Salaris; Cassisi, 2005), turning the He-intershell relatively rich in ^{14}N. This isotope is an efficient neutron absorber (Karakas; Lattanzio, 2014) that relies on the neutron source $^{13}C(\alpha,n)^{16}O$ to fire the sequence $^{14}N(n,p)^{14}C(\alpha,\gamma)^{18}O(p,\alpha)^{15}N$ during the interpulse[8]. The first reaction of the chain releases a proton, which may be absorbed in $^{15}N(p,\alpha)^{12}C$, but also feeds $^{18}O(p,\alpha)^{15}N$. As the thermal pulse begins, the remaining ^{15}N may capture an α particle instead of a proton, producing F through $^{15}N(\alpha,\gamma)^{19}F$. Cristallo et al. (2014) cite other paths for F production as well, one being $^{14}N(\alpha,\gamma)^{18}F(\beta^+\nu_e)^{18}O$, which contributes with ^{18}O seeds. Gallino et al. (2010) argue for non-negligible contributions from proton and neutron capture by ^{18}O, the latter being responsible for $\sim$ 10 percent of AGB F (Gallino et al., 2010; Cristallo et al., 2014). Also known as a neutron source in AGB stars, the reaction $^{22}Ne(\alpha,n)^{25}Mg$ does not play a role

---

companion.

[7] In this notation, the global metallicity Z represents the fraction of chemical elements in the star that are not H or He. For the Sun, $Z \approx 0.014$, i.e., metals compose ≈ 1.4 % of the Sun.

[8] The H-burning step of the TP-AGB.

in F production because it is active in the thermal pulse (Cristallo et al., 2009), and the neutrons needed by the reaction chain are consumed in the interpulse period.

Any calculations on F production must take into account reactions which destroy it. Cristallo et al. (2014) mention reactions involving proton, neutron and α-capture by ^{19}F, of which ^{19}F(α,p)^{22}Ne seems to be preponderant. The efficiency of both creation and destruction of F is tied to the temperature at the base of the He shell (Mowlavi; Jorissen; Arnould, 1996), with optimal values ranging between $\sim 2.2 \times 10^8$ K and $\sim 2.6 \times 10^8$ K. At lower temperatures the creation through ^{15}N(α,γ)^{19}F is inneficient, while at higher temperatures ^{19}F(α,p)^{22}Ne becomes efficient. Another parameter that affects the presence of F in the intershell is the amount of third dredge-up (Lugaro et al., 2004). Coupled, both parameters generate an optimum for AGB F yields between 2 and 4 $M_\odot$, whose peak changes with metallicity (Lugaro et al., 2004; Karakas, 2010; Karakas; Lugaro, 2016), a result observationally confirmed (see, e.g., Abia et al. (2015)). The yields are subject to uncertainties in reaction rates, which are still high in several reactions relevant to F production, including the destruction channel ^{19}F(α,p)^{22}Ne (Lugaro et al., 2004; Cristallo et al., 2014). Improvements may be achieved by combining both laboratory experiments to measure the reaction rates in the range of energies of astrophysical relevance (see, e.g., the recent measurements from Indelicato et al. (2017) and D'Agata et al. (2018)) with spectroscopic-based observational results of chemical analysis.

After the first measurements by Jorissen, Smith & Lambert (1992), several works found additional evidence for F nucleosynthesis in AGB stars through the observation of objects such as post-AGB stars, planetary nebula, binary systems and extragalactic AGB stars as well (Werner; Rauch; Kruk, 2005; Zhang; Liu, 2005; Pandey, 2006; Schuler et al., 2007; Abia et al., 2009; Abia et al., 2010; Lucatello et al., 2011; Abia et al., 2011; Alves-Brito et al., 2011). However, some works have found results incompatible with exclusive chemical enrichment by AGB stars, such as the lack of s-process enhancement in F-rich stars from the bulge (Cunha; Smith; Gibson, 2008). Also, a steep dependence of the F/O ratio with metallicity probed by observations in ω Centauri, which may be interpreted as evidence of WR influence in chemical evolution of F, because WR yields are expected to be metallicity-dependent (Cunha et al., 2003).

The early set of measurements had been in disagreement with predicted abundances of F in AGB stars, a dispute partially solved by the results from Abia et al. (2009). These results revised downward, by 0.8 dex, the previous published abundances such as those from Jorissen, Smith & Lambert. The difference was attributed by Abia et al. (2009) to unnacounted blends with C-bearing molecules in earlier works, an hypothesis later reinforced by the results from Abia et al. (2010). Afterwards, a revision of quantum mechanical parameters of the Hydrogen Fluoride (HF) molecule further decreased observed F abundances by ~ 0.35 dex (Nault; Pilachowski, 2013; Abia et al., 2015). The HF molecule is needed to estimate the abundances of F because atomic lines of this element are not detectable in stellar atmospheres (Jorissen; Smith; Lambert, 1992). It has several transitions available in the infrared, detectable in cool stars – usually those with effective temperature $T_{\rm eff} < 4700$ K (see, e.g., Pilachowski & Pace (2015)). Of these transitions, the most widely used is the HF 1-0 R9 line[9] at 23358.3 Å. The advantage of this transition over other HF transitions observable in cool stars is being a weak line free from blends (e.g., Nault & Pilachowski (2013)) – except for rare cases where a neighbour $^{12}C^{17}O$ line is too strong. Its disadvantage is being undetectable in metal-poor stars – to circumvent this, Jönsson et al. (2014b) suggests the use of a stronger line in the 12.2 μm region (N-band).

In the context of chemical evolution of the Galaxy there are still open questions. Kobayashi et al. (2011) published models of chemical evolution based on observations in solar neighbourhood (Cunha; Smith, 2005), bulge (Cunha; Smith; Gibson, 2008) and globular clusters (GC) (Cunha et al., 2003; Smith et al., 2005; Yong et al., 2008; Alves-Brito et al., 2012). They focused on the chemical evolution of F through the ν-process and AGB yields, while the WR contribution was discarded because F yields in WR stars are subject to stellar rotation (Heger; Woosley; Spruit, 2005; Palacios; Arnould; Meynet, 2005). They concluded that the contribution from AGB stars is minimal in the metal-poor regime, [Fe/H][10] < -1.5 (see also Kobayashi, Karakas & Umeda (2011) and Travaglio et al. (1999)), an expected result due to the longer evolutionary timescales of low- and intermediate-mass stars. When including the ν-process, there is a [F/O] plateau at low metallicities ([O/H] < -1.2), followed by an increase in the [F/O] ratio due to the AGB contribution. The low metallicity plateau is expected because of the exclusive production of both F and O by the Type II SNe environment in the low metallicity regime. The position of the plateau is dependent on neutrino luminosity, but observational data for field stars is required in this metallicity interval, therefore any calibration of the neutrino luminosity is pending. Regarding globular clusters, Kobayashi et al. (2011) argues that GC data is not a *bona fide* tracer of Galactic chemical evolution of F due to peculiarities in star formation and chemical history in these environments – e.g., different contribution from low-mass SNe to local gas enrichment.

Meanwhile, Abia et al. (2015) built a Galactic chemical evolution model of F accounting only for AGB yields. In comparison with available observational data, their models show that the AGB contribution is insufficient to explain F abundances in the solar neighbourhood, and other nucleosynthesis sites are needed, a result that had already been found by Jönsson et al. (2014a), whose analysis focused on bulge stars. It is also noteworthy to point out that their models were fed with two sets of F yields, from Karakas (2010) and Cristallo et al. (2015). The yields from Karakas generate higher [F/Fe] abundances in

---

[9] This notation indicates a ro-vibrational transition in a molecule. See, e.g., Demtröder (2010).

[10] Standard spectroscopic notation: [X] represents the logarithmic ratio of quantity X w.r.t. the Sun, i.e., $[X] = \log(X)_* - \log(X)_\odot$. Naturally, the quantity X may be some ratio such as Fe/H.

the chemical evolution model: Abia et al. attribute the discrepancy to different treatments in the amount of third dredge-up and hot bottom burning efficiency. Therefore, if one succeeds to isolate the contribution from AGB stars in chemical enrichement – e.g., by observing binary systems subject to mass transfer – there is the possibility of fine-tuning these parameters in stellar evolution codes through observational constraints. On the other hand, Jönsson et al. (2014b) suggested that AGB nucleosynthesis might account for all F in the solar neighbourhood. Their results were in agreement with AGB-only models from Kobayashi et al. (2011). However, the authors emphasized that their conclusions were provisional – they analysed seven giants – and more observations were needed.

The work by Pilachowski & Pace (2015) was the first large-scale survey of F in normal G and K stars – 51 targets, both dwarfs and giants of the solar neighbourhood. In comparison with the models from Kobayashi et al. (2011), they found agreement with the prediction of significant contribution from the ν-process in the solar neighbourhood in the [F/Fe] vs. [Fe/H] plot, with a barely negative slope in the solar metallicity interval, as predicted by the ν-process+AGB model from Kobayashi et al.. However, one must note that a zero slope – i.e., a flat trend – is inside the estimated uncertainty.

Later, Jönsson et al. (2017) published F, O and Fe measurements in another large sample – 49 K giants from the solar neighbourhood – and found results totally different from Pilachowski & Pace (2015). Jönsson et al. found a *positive* trend in the [F/Fe] vs. [Fe/H] plot, in contrast with both Kobayashi et al. models and Pilachowski & Pace observations. From these results, they argue against the hypothesis of ν-process dominated F enrichment in the solar neighbourhood, because a large contribution of Type II SNe would imply an α-like behaviour of F, with decreasing [F/Fe] after the onset of Type Ia SNe, which produces large amounts of Fe relative to Type II SNe. Also, they argue that the contribution from AGB stars is expected to correlate with metallicity and that mass loss in WR stars – therefore their F yields – increases with metallicity. Thus, these sites should be dominant in F production.

Their suggestion is further strengthened by the comparison between F and O abundances: one would expect a flat behaviour of [F/O] against [O/H] if most F came from the ν-process (i.e., Type II SNe). The results from Jönsson et al. indicate a steep increase of [F/O] with Oxygen, even greater than that predicted by the AGB-only model from Kobayashi et al., hence, they argue, the contribution from WR stars, not present in Kobayashi et al. models, should be taken into account. Finally, Jönsson et al. suggest that F has a secondary behaviour in comparison with Oxygen: the production of a primary element should be insensitive to the initial chemical composition of the star, while a secondary element has its production tied to the initial composition. In AGB and WR stars, the reaction chain leading to F depends on ^{14}N, which may be a byproduct of the CNO cycle inside the star, i.e., secondary. That is, more CNO implies greater ^{14}N production, therefore, greater F production. In the ν-process, they argue, F is primary, as O. Their results show a slope of ~ 2 in the A(F) vs. A(O) plot, while a ν-process dominated primary behaviour would generate a slope of 1. The results from Jönsson et al. present less scatter than those from Pilachowski & Pace. The reason, as Jönsson et al. argue, may be the determination of the atmospheric parameters[11]: their atmospheric parameters were determined from the same set of observations, i.e., they are homogeneous, while those from Pilachowski & Pace had to be determined by a compilation from literature results.

To evaluate the recent observational results, Spitoni et al. (2018) published a series of Galactic chemical evolution models for F, considering yields from several sites – Type Ia (Iwamoto et al., 1999) and II SNe (Kobayashi et al., 2006), AGB (Karakas, 2010) and WR stars (Meynet; Arnould, 2000). They tested models considering both two-infall and one-infall scenarios, the later because the sample from Jönsson et al. (2017) is supposed to be composed mostly by thin disc stars. Their best-fitting models are those from the one-infall scenario, and the model that best fits the observational data has the WR yields from Meynet & Arnould doubled. However, this model overestimates the solar composition, while the model with 'normal' WR yields and doubled AGB yields fits well the solar region while still gives acceptable results in comparison with observational data. They also suggested the possibility of contribution from Novae, using the yields from José & Hernanz (1998). However, they point out that these yields are highly uncertain and need to be multiplied by three to fit the observations. Thus, fine tuning of stellar yields is still needed, i.e., efforts should be made to both confirm (or disprove) F production in WR stars and to fine tune the already known F nucleosynthesis in AGB stars. Though, none of the models from Spitoni et al. is able to reproduce the positive correlation between F and Fe found by Jönsson et al. (2017) in the solar metallicity, a problem they share with the models from Kobayashi et al. (2011).

From what has been presented in this section, one must therefore conclude that the quest to unravel the mystery about the cosmic production and evolution of F is far from over.

1.2 Aims

This work relies on high quality spectroscopic observations of 27 stellar targets made in 2013 – see Section 2.3 for observational details. The sample is divided in three groups of targets:

- Cool giants from the Galactic outer disc, whose galactocentric distances range from 10 to 14 kpc. These objects were previously analysed with optical spectra by Bensby

---

[11] Atmospheric parameters will be discussed in more depth in Ch. 2.

et al. (2011). They published abundances of Mg, Si, Ti and Fe, as well as atmospheric parameters.

- Cool dwarfs from the Hyades open cluster, none of them with F abundances determined, to our knowledge. Most of these objects already have published chemical abundances from optical spectra.
- A variety of binary systems which are suspected (or have been confirmed) to have suffered mass transfer by the (now) white dwarf component. All of them were previously studied in the optical, and some have published results in the infrared, useful for comparisons.

The objectives of this work reflect the heterogeneity of its sample, but, in general, revolve around the common theme of F.

First, we will perform a kinematic analysis using fresh astrometric data from Gaia DR2 (Gaia Collaboration et al., 2018) for all studied targets – focusing more on those which are not in binary systems. With kinematics, we intend to complement the chemical analysis of the outer disc giants, e.g., inferring if they are indeed from the Galactic disc. Also, the astrometric data will be employed to check if all dwarfs in the Hyades subsample are from the open cluster.

The chemical analysis will take advantage of the large observed spectral interval (several orders in two photometric bands). Several species of different nucleosynthesis origins will also be observed (CNO, α, odd-Z, Fe-peak and one s-process element). The results for these species will help to support the findings for F (when possible) and will be useful in comparisons with already published results for our targets.

The study of the outer disc stars will be exploratory. We will look for gradients in [F/Fe], both radial and vertical. A comparison of F with Oxygen abundances, similar to that made by Jönsson et al. (2017), will be presented for those stars with available information on these two elements.

The study of the Hyades is interesting because, being an open cluster, it is assumed that its stars share the same chemical composition, at least at the uncertainty level we are aiming (0.1-0.2 dex). Thus, the analysis of its cool dwarfs will allow us to test if the models whose the measurements are dependent are well calibrated. Since the F abundances rely on one weak, clean line, we assume that this element may be a trustworthy benchmark for star-to-star comparison.

Finally, the binary systems are composed of both metal-poor – CH-stars, Carbon Extreme Metal-Poor stars (CEMP) – and relatively metal-rich – Ba-stars – chemically peculiar objects. F has been studied in these systems in the last decade (e.g., Schuler et al. (2007), Lucatello et al. (2011), Alves-Brito et al. (2011)). In this work we intend to present results that will, in the very near future, help to constrain the models of AGB nucleosynthesis. The reason is that the stars from this subsample are expected to be polluted by a former AGB companion, thus their atmospheric chemistry must reflect the yields from an AGB star. When possible, we will test the validity of the spectroscopic analysis using simple atmospheric models in these chemically peculiar, C-enhanced objects, through comparisons with results from the literature.

2 Methodology and observations

In this Chapter we will review what allows us to reach the results presented in Ch. 3. We will start reviewing the physical model behind the spectroscopic analysis of chemical abundances, describing qualitatively the models of stellar atmospheres and line formation. This will be followed by a very brief generic description of the spectrograph class where the data for this work was acquired. Then, the observations and data reduction process will be discussed. Finally, we will describe the analysis method adopted in a 'high-level language' approach.

2.1 Stellar atmospheres and spectral lines

The purpose of this section is to give a qualitative review of the physical phenomena behind the measurement of chemical abundances in stellar atmospheres. A rigorous formalism is developed in several textbooks and it is beyond the scope of this work. The content of the following paragraphs is well covered in (and it is based on) Mihalas (1970), Gray (2005) and Tatum (2017), except when indicated.

First of all, what is a spectrum? Here, we are referring to the *electromagnetic spectrum*, a consequence of the wave nature of the electromagnetic radiation, which is described by the Maxwell equations. The electromagnetic spectrum is a continuum composed of waves of infinite wavelengths, from gamma rays to very long-wavelength radio waves (Carroll; Ostlie, 1996).

Mathematically, we may describe the spectrum of a stellar point source as a function $F(\lambda)$, which represents the luminous flux emmited from some source at wavelength λ. This is the 'original' spectrum, but it is not the observed spectrum which we analyze after collecting it through a telescope. The electromagnetic radiation will be collected by a detector of finite size, so we need to multiply $F(\lambda)$ by a rectangular function $\Pi(\lambda)$, which equals one in the recorded wavelength interval $\Delta\lambda$ and zero otherwise. Spectra are recorded by detectors composed by arrays of discrete elements, i.e., they are sampled. This sampling is well described by the *Dirac comb*:

$$III(\lambda) = \sum_{n=-\infty}^{\infty} \delta(\lambda - nT), \tag{2.1}$$

where n is an integer and T is the separation between the sampling points[1]. Finally, the instrument blurs the signal, and the nominal resolution is linked to this blurring, which

---

[1] Rigorously, T increases with λ, but it may be considered constant for a short interval $\Delta\lambda$.

may be described by a convolution with a function $I(\lambda)$ representing the instrumental broadening. Thus, the observed spectrum $S(\lambda)$ may be described by:

$$S(\lambda) = F(\lambda)\Pi(\lambda)III(\lambda) * I(\lambda). \tag{2.2}$$

$S(\lambda)$ from Eq. 2.2 is usually stored as two arrays (for S and for the sampled λ) in an ASCII file or as a vector for S in a .fits file with parameters for the λ vector defined in its header. It is worthy to note that, because of the $III(\lambda)$ component, the observed spectrum is subject to the Nyquist–Shannon sampling theorem (Nyquist, 1928; Shannon, 1949), and the relation between T and the size of the resolution element $\delta\lambda$ must be taken into account to avoid undersampling when designing an instrument.

Having defined what the observed spectrum is, we may proceed to the description on the formation of stellar spectra, i.e., we will discuss what is needed to model $F(\lambda)$ for a given star. This work is focused on absorption lines, i.e., those regions where the flux is subtracted from the continuum, and we will briefly discuss their causes.

Some basic assumptions are needed here. They are not rigorously correct, but they work as satisfactory approximations for the purpose of this work, and are crucial for the atmospheric models used here. The first assumption is that a star is spherically symmetric, so we may treat its flux as isotropic regardless of the line of sight of the observer. This isotropy allows us to discard two dimensions and concentrate only on variations dependant on the radial component of the atmosphere. The next assumption is that the volume of the photosphere is a tiny fraction of the volume of the star, i.e., $\Delta r \ll R_*$, where Δr is the distance between the upper and lower limits of the photosphere and R_* is the stellar radius. As a consequence, we are allowed to employ plane-parallel atmospheric models, as we are dealing with phenomena happening in a tiny fraction of stellar radius, and the curvature is not crucial[2]. Observationally, plane-parallel and spherical models yield the same results, at least for cool giants (Alves-Brito et al., 2010). Other assumptions are the lack of temporal variabillity, allowing a time-independent atmosphere, the lack of spatial variability – i.e., negligible rotation or spatial structures such as starspots – and the conservation of energy: no sources or sinks of energy exist in the stellar atmosphere, the energy transported in the outer layers of the star comes from its core. For the sake of simplicity and brevity, mechanisms of energy transport other than radiation will be neglected. The equation of state is the ideal gas law. Finally, we will assume *Local Thermodynamic Equilibrium* (LTE): the modelled atmospheres are stratified in layers, each one in thermodynamic equilibrium and defined by a single temperature.

The first step to model the formation of spectral lines is the definition of the

---

[2] This is analogous to the approximation of the gravitational acceleration being constant near the surface of the Earth.

quantity called *specific intensity* I_ν:

$$I_\nu = \frac{\mathrm{d}E}{\cos\theta \mathrm{d}A \mathrm{d}\Omega \mathrm{d}\nu \mathrm{d}t}. \tag{2.3}$$

That is, the specific intensity corresponds to the energy $\mathrm{d}E$ propagating by an area $\mathrm{d}A$, to a solid angle $\mathrm{d}\Omega$ projected from $\mathrm{d}A$, through a time $\mathrm{d}t$, in a direction whose projection to the normal unit vector $\hat{\boldsymbol{n}}$ of the area element is defined by the angle θ. The subscript ν is used to refer to a monochromatic specific intensity, and integrating $I_\nu d\nu$ over all frequencies gives the total specific intensity. For those using wavelength instead of frequency, the relation $I_\nu \mathrm{d}\nu = I_\lambda \mathrm{d}\lambda$ holds, where $\mathrm{d}\nu = -(c/\lambda^2)\mathrm{d}\lambda$.

The specific intensity is defined in a manner which is *invariant* if no emission or absorption occurs, i.e., it can be understood as a proportionality constant relating the radiation field evaluated with $\mathrm{d}E$ and the geometry described in Eq. 2.3. To understand that, imagine in some radiation field a monochromatic quantity $\mathrm{d}E$ of energy moving in a direction defined by the unit vector $\hat{\boldsymbol{s}}$ – whose projection in $\hat{\boldsymbol{n}}$ is described by an angle θ, i.e., $\hat{\boldsymbol{s}} \cdot \hat{\boldsymbol{n}} = \cos\theta$ – passing through some point P in space in an interval of time $\mathrm{d}t$. Because of the conservation of energy, the monochromatic quantity $\mathrm{d}E'$, of same frequency as $\mathrm{d}E$, from the same radiation field, passing through a point P' in a direction $\hat{\boldsymbol{s'}}$ in the same time interval must be equal to $\mathrm{d}E$. Then, we may write the relation:

$$\mathrm{d}E = I_\nu \mathrm{d}\nu \cos\theta \mathrm{d}A \mathrm{d}\Omega \mathrm{d}t = I'_\nu \mathrm{d}\nu \cos\theta' \mathrm{d}A' \mathrm{d}\Omega' \mathrm{d}t = \mathrm{d}E'. \tag{2.4}$$

The definition of solid angle may be employed to argue that the solid angle projected by $\mathrm{d}A$ for an observer in P' detecting $\hat{\boldsymbol{s}}$ is $\mathrm{d}\Omega' = \mathrm{d}A\cos\theta/r^2$, with r being the distance between P and P'. The reciprocal is valid for $d\Omega$ as well. substituting the solid angles as described in the two previous sentences, Eq. 2.4 simplifies to $I_\nu = I'_\nu$.

The invariance of the specific intensity in a vacuum becomes an useful tool to model the absorpion and emission of radiation in a given radiation field. Let s be the direction of travel of a quantity I_ν of radiation. In case of absorption, this quantity changes by:

$$\mathrm{d}I_\nu = -\kappa_\nu \rho I_\nu \mathrm{d}s, \tag{2.5}$$

where ρ is the mass density of the medium and κ_ν is a mass absorption coefficient. The solution of this differential equation is an exponential decay. Defining the *optical depth*, with L being the length of the absorbing slab:

$$\tau_\nu = \int_0^L \kappa_\nu \rho \mathrm{d}s, \tag{2.6}$$

the solution of Eq. 2.5 may be written as:

$$I_\nu = I_\nu(0)e^{-\tau_\nu}, \tag{2.7}$$

where $I_\nu(0)$ is the specific intensity right before the beggining of the absorbing slab. The interpretation of the optical depth may be taken as how transparent the slab is. Let $I_\nu(0)$ be an arbitrary intensity. According to Eq. 2.7, the fraction of photons arriving at the end of the slab equals the ratio $I_\nu/I_\nu(0)$, i.e., we may think of $e^{-\tau_\nu}$ as the probability that a photon arrives at the end of a slab with optical depth τ_ν.

Also, radiation may be emmited inside the slab. The change in I_ν is described, analogously, as:

$$\mathrm{d}I_\nu = j_\nu \rho \mathrm{d}s, \tag{2.8}$$

where j_ν is the respective emmision coefficient. Notice the lack of the I_ν term: the emission is independent of the incoming radiation, its occurrence being due to the properties of the material inside the slab. Eq. 2.5 and Eq. 2.8, combined, give the *equation of radiative transfer*:

$$\mathrm{d}I_\nu = -\kappa_\nu \rho I_\nu \mathrm{d}s + j_\nu \rho \mathrm{d}s. \tag{2.9}$$

Taking advantage of the definition of optical depth, Eq. 2.9 is simplifying if divided by $d\tau_\nu$:

$$\frac{\mathrm{d}I_\nu}{\mathrm{d}\tau_\nu} = -I_\nu + \frac{j_\nu}{\kappa_\nu}. \tag{2.10}$$

Notice that j_ν/κ_ν works as a source funcion in the differential equation. Indeed, a source function S_ν is defined by this ratio:

$$\frac{\mathrm{d}I_\nu}{\mathrm{d}\tau_\nu} = -I_\nu + S_\nu. \tag{2.11}$$

The source function S_ν describe all processes of absorption and emission: destruction (covered by κ_ν), creation (encompassed in j_ν) and scattering (both) of photons. They account for both spontaneous and stimulated emission, as well as absorption processes. In LTE, each layer of the atmosphere is in thermodynamic equilibrium. This implies $j_\nu = \kappa_\nu B_\nu$, i.e., $S_\nu = B_\nu$, where $B_\nu = B_\nu(T)$ is the Planck function with an associated temperature.

In a plane-parallel geometry, we want a model atmosphere stratified in layers, whose borders are normal to a coordinate x. Because we are assuming spherical symmetry, we are allowed to define the path s in Eq. 2.9 as being in the cartesian z axis. Then:

$$\frac{\partial}{\partial z} = \cos\theta\frac{\partial}{\partial r} - \frac{\sin\theta}{r}\frac{\partial}{\partial\theta}. \tag{2.12}$$

where θ is the polar coordinate. With I_ν spherically symmetric, the second term in Eq. 2.12 may be discarded if we derivate the specific intensity. Thus:

$$\frac{\mathrm{d}I_\nu}{\mathrm{d}s} = \frac{\mathrm{d}I_\nu}{\mathrm{d}z} = \cos\theta\frac{\mathrm{d}I_\nu}{\mathrm{d}r}, \tag{2.13}$$

and, in plane-parallel geometry, the equation of radiative transfer is written as:

$$\cos\theta\frac{\mathrm{d}I_\nu}{\mathrm{d}\tau_\nu} = I_\nu - S_\nu. \tag{2.14}$$

The sign change in the right-hand side is due to the (usual) definition of $x = -r$. The coordinate x is a geometric depth and its definition is chosen in this way so that x grows with the optical depth, which increases to the stellar interior. Angle θ projects the radiation path s in x. Proper modelling of stellar spectra in a plane-parallel geometry is, basically, an exercise of solving the equation of radiative transfer.

In the form given by Eq. 2.11, the equation of radiative transfer is a linear first-order differential equation with a well known solution. For an undefined source function, it can be written in an integral form:

$$I_\nu(\tau_\nu) = \int_0^{\tau_\nu} S_\nu(t_\nu)e^{-(\tau_\nu - t_\nu)}\mathrm{d}t_\nu + I_\nu(0)e^{-\tau_\nu}. \tag{2.15}$$

In plane-parallel geometry, Eq. 2.15 translates to:

$$I_\nu(\tau_\nu) = \int_{\tau_\nu}^{\infty} S_\nu(t_\nu)e^{-(t_\nu-\tau_\nu)\sec\theta}\sec\theta\mathrm{d}t_\nu - \int_0^{\tau_\nu} S_\nu(t_\nu)e^{-(t_\nu-\tau_\nu)\sec\theta}\sec\theta\mathrm{d}t_\nu, \tag{2.16}$$

with the distribution of the integration in two intervals due to the boundary conditions differing for radiation going outwards ($\theta < \pi/2$, first integral) and inwards ($\theta > \pi/2$, second integral). The second integral is null at the surface of the star ($\tau_\nu = 0$), as it is assumed that the star receives negligible radiation from the universe.

Before we proceed, the definition of three quantities related to I_ν are needed. The mean intensity J_ν is the average of the specific intensity (its zeroth moment) over a unit shell:

$$J_\nu = \frac{1}{4\pi}\int_\Omega I_\nu \mathrm{d}\Omega. \tag{2.17}$$

The concept of flux has already been used in this section. Now it is appropriate to define it formally – the monochromatic flux is all the energy of a given frequency that flows through a given area in a given amount of time:

$$F_\nu = \frac{\int \mathrm{d}E}{\mathrm{d}A\mathrm{d}\nu\mathrm{d}t} = \int_\Omega I_\nu \cos\theta \mathrm{d}\Omega, \tag{2.18}$$

with F_ν being the first moment of I_ν. Finally, the second moment is:

$$K_\nu = \frac{1}{4\pi}\int_\Omega I_\nu \cos^2\theta \mathrm{d}\Omega. \tag{2.19}$$

Eq. 2.18 is important because it integrates I_ν over all angles, i.e., it allows us to collapse the specific intensity from all θ into a single quantity. Thus, for a point source – most resolved stars in the universe – we must use flux instead of specific intensity to model its spectrum. However, it must be taken into account that, since we are giving up the unitary solid angle, the flux decreases in an inverse-square law. Written for flux, Eq. 2.16 becomes:

$$F_\nu(\tau_\nu) = 2\pi\int_{\tau_\nu}^{\infty} S_\nu E_2(t_\nu - \tau_\nu)\mathrm{d}t_\nu - 2\pi\int_0^{\tau_\nu} S_\nu E_2(\tau_\nu - t_\nu)\mathrm{d}t_\nu, \tag{2.20}$$

where $E_n(x)$ is defined as:

$$E_n(x) = \int_1^\infty \frac{e^{-xt}}{t^n}\mathrm{d}t, \tag{2.21}$$

and the flux escaping the surface ($\tau_\nu = 0$) is:

$$F_\nu(0) = 2\pi\int_0^\infty S_\nu(t_\nu)E_2(t_\nu)\mathrm{d}t_\nu. \tag{2.22}$$

The interpretation of Eq. 2.22 is that the surface flux is the sum of the source functions from all internal layers, weighted by E_2, which works as an extinction coefficient – the shape of E_2 is an exponential decay. The monochromatic flux F_ν or F_λ given in Eq. 2.20, corresponds to the $F(\lambda)$ for a given λ from Eq. 2.2. The total flux $\mathcal{F}$ is the integral of F_ν over all frequencies. The moments J_ν and K_ν may also be described in terms of S_ν as we made for flux, and their expressions will be omitted for brevity.

At the begining of this section, we stated that we are assuming no sources or sinks of energy in the atmosphere. This implies that, in the spherical shell under consideration,

$\nabla \cdot \mathbf{F} = 0$, and in the context of stellar atmospheres this condition is known as *radiative equilibrium*. In the unidimensional geometry of our approach, we have:

$$\frac{\mathrm{d}\mathcal{F}}{\mathrm{d}x} = \frac{\mathrm{d}}{\mathrm{d}x}\int_0^\infty F_\nu \mathrm{d}\nu = 0. \tag{2.23}$$

This condition also implies that the integration of Eq. 2.20 over frequency yields a constant in its left-hand side.

Then, integrating Eq. 2.14 over solid angle, we have:

$$\frac{\mathrm{d}}{\mathrm{d}\tau_\nu}\int_\Omega I_\nu \cos\theta \mathrm{d}\Omega = \int_\Omega I_\nu \mathrm{d}\Omega - \int_\Omega S_\nu \mathrm{d}\Omega. \tag{2.24}$$

The integral in the left-hand side gives the flux F_ν. In the right-hand side, the integral of the specific intensity gives $4\pi J_\nu$. We are assuming S_ν isotropic, thus the second integral results in $4\pi S_\nu$. Substituting $\mathrm{d}\tau_\nu = \kappa_\nu \rho \mathrm{d}x$ and integrating over all frequencies, it becomes clear that the left-hand side of the above equation is zero. Therefore:

$$\int_0^\infty \kappa_\nu (J_\nu - S_\nu) d\nu = 0. \tag{2.25}$$

Multiplying Eq 2.24 by $\cos\theta$ yields the integral for K_ν in the left-hand side of que equation. In the right-hand side, because of the assumption of isotropic S_ν, the second integral is null, as we are integrating $\cos\theta$ over the entire unit sphere. The other integral if the flux integral. The result is:

$$4\pi \int_0^\infty \frac{\mathrm{d}K_\nu}{\mathrm{d}\tau_\nu} \mathrm{d}\nu = \mathcal{F}. \tag{2.26}$$

As mentioned before, J_ν and K_ν may be written in terms of S_ν as made for flux in Eq. 2.20. The appropriate S_ν for a given optical depth τ_ν is found when the conditions described by Eqs. 2.20, 2.25 and 2.26 are satisfied. In LTE, knowing the source function of an atmospheric layer allows us to know its respective temperature, because, as aforementioned, in LTE the source function is the Planck function.

We need to know the stellar flux $\mathcal{F}$ to solve the above equations. The value for $\mathcal{F}$ is estimated through the Stefan-Boltzmann law, $\mathcal{F} = \sigma T_{\mathrm{eff}}^4$, where σ is the Stefan-Boltzmann constant. That is, given a single value of *effective temperature*, S_ν may be calculated for each layer of the atmosphere, a step needed to build the atmospheric model. The effective temperature is an *atmospheric parameter*, an input value needed to create the model.

When solving the above equations in order to build the atmospheric model, we need to evaluate κ_ν, which may be interpreted as the distribution of the absorption coefficient over the spectral continuum. This quantity encompasses several phenomena ocurring in the atmosphere, which may be summarized in two types of transitions. The first is a *bound-free* transition, i.e., a ionization process, which enriches the atmosphere with electrons, and absorbs photons itself, contributing with the overall opacity. The other one is a *free-free* transition, ocurring during the interaction of free charges in the gas. The free-free transitions depend on the existence of free electrons. Metals work as electron donors more efficiently in cool stars than the more abundant Hydrogen and Helium despite accounting for less than 2% of the composition of the atmosphere, since the first ionization energies are usually smaller for metals. These heavy elements also work as electron donors for the H^- ion, itself an important opacity source in cool stars, because of its low ionization potential (0.754 eV). Therefore, an atmospheric model must account for the chemical composition of the atmosphere, usually in terms of the metallicity[3], this being another atmospheric parameter.

The opacity due to the presence of ions such as H^- depends on the presence of ionized species in the atmosphere. Under LTE, the ion-to-neutral ratio is modeled through the Saha equation, which may be written in the logarithmic form as:

$$\log\frac{N_j}{N_k}P_e = -\frac{5040}{T}I + 2.5\log T + \log\frac{Z_j}{Z_k} - 0.1762, \tag{2.27}$$

where N_j/N_k is the ratio between two ionization states, N being the number of particles per volume unit, T is the temperature of the gas (not to be confused with T_{eff}), Z_j and Z_k are the partition functions of the ionization states, I is the ionization potential, i.e., the energy needed to switch from one ionization state to the other and P_e is the electron pressure of the gas. To solve the Saha equation we need to know P_e. For this task, we take advantage of the assumption of hydrostatic equilibrium:

$$\mathrm{d}P = \rho g \mathrm{d}x = \frac{g}{\kappa_\nu}\mathrm{d}\tau_\nu, \tag{2.28}$$

where g is the surface gravity, another atmospheric parameter. The simplistic description adopted here imposes the approximation $P \approx P_{gas}$, with P_{gas} being gas pressure, neglecting radiation pressure, magnetic pressure and other components of the total pressure. Thus, P_{gas} may be calculated for a given τ_0 by:

$$P_{gas} = \left(\frac{3}{2}g\int_0^{\tau_0}\frac{\sqrt{P_{gas}}}{\kappa_0}\mathrm{d}t_0\right)^{\frac{2}{3}}. \tag{2.29}$$

---

[3] It would not make sense to give the detailed composition of the atmosphere as input, because this is exactly what a spectroscopist is trying to discover when he/she adopts an atmospheric model. Some models accept a metallicity value as input and scale them to the solar composition. The more refined ones also accept CNO and α abundances, and their use imply a iterative process of adjusting the input and output abundances.

where the quantities with zero in the subscript denote reference quantities from distributions (τ_ν, κ_ν) in a given frequency/wavelength, since pressure is frequency-independent. From inspection of Eq. 2.29 it becomes clear that it must be solved iteratively. The value of κ_0 comes from κ_ν, which in turn depends on the chemical composition and on ionization levels, as briefly discussed above. The modelling of ion composition requires the Saha equation and, thus, P_e. Fortunately, there is a relation between P_{gas}, P_e and T, derived from the Saha equation itself and from the ideal gas law, also solvable iteratively, which yields P_e for a given set of P_{gas}, T and chemical composition. Having completed the iteration for P_e from a initial guess of P_{gas}, κ_0 is estimated and the next iteration of the integral in Eq. 2.29 is made. The whole process continues until convergence of $P_{gas}(\tau_0)$, being repeated for each optical depth.

After the calculation of gas and electron pressures, the continuum opacity κ_ν may be properly determined, and, as a consequence, also the continuum flux. In practice, due to the computer-intensive nature of atmospheric modelling, the atmosphere of a single star is usually interpolated from a grid of pre-computed models, under the input of a set of atmospheric parameters. All the above discussion is a brief and simplified review on how to build a model of the continuum of a stellar spectrum, whose flux is subtracted by atoms and molecules in the atmosphere generating spectral lines through bound-bound transitions.

A naïve interpretation of quantum phenomena involving bound-bound transitions would describe a spectral line as a δ-function[4]. The spectral line has a natural broadening owing to the finite-time nature of the interaction between light and matter. The full quantum-mechanical treatment describes the interaction between an atom and an electromagnetic wave as a sinusoidal perturbation in the atomic system. The description adopted here is based on a classical dipole oscillator, driven by the electric field component of the electromagnetic wave polarized in the cartesian x axis. It is justified for non-forbidden transitions because the matrix element of the electric dipole component of the perturbed hamiltonian is dominant for transitions with associated wavelenghts much larger than the Bohr radius. Also, the evolution of the position operator calculated with the perturbed hamiltonian through the Ehrenfest theorem yields the equation of a driven harmonic oscillator (Cohen-Tannoudji; Diu; Laloe, 1986). Classical electromagnetic theory yields for the dipole oscillator the following equation of motion, in complex form:

$$\frac{\mathrm{d}^2 x}{\mathrm{d}t} = -(\omega_0^2 + i\gamma\omega_0)x, \tag{2.30}$$

---

[4] This hypothetical naïve interpretation does not even take into account the Heisenberg uncertainty principle, anyway.

where:

$$\gamma = \frac{2q^2\omega_0^2}{m_e c^3}, \tag{2.31}$$

ω_0 is the angular frequency of the oscillation of the electric field, c is the speed of light and q and m_e are, respectively, charge and mass of the electron.

The solution of Eq. 2.30 is known:

$$x(t) = x_0 e^{i\omega_0 t - \frac{1}{2}\gamma t}, \tag{2.32}$$

being the solution for a damped oscillation. Defining $F(\omega)$ as the Fourier transform of the oscillator, we can take its energy spectrum as $E(\omega) = \frac{1}{2\pi}F^*(\omega)F(\omega)$. The energy spectrum of the solution given by Eq. 2.32 is a *Lorentz profile*, and is the line profile associated with natural broadening. Written in a normalized form and as function of angular frequency, the Lorentz profile is:

$$L(\omega) = \frac{\gamma/2\pi}{(\omega-\omega_0)^2 + (\gamma/2)^2}. \tag{2.33}$$

Now, we introduce two new quantities: the line mass absorption coefficient l_ν and the absorption coefficient per atom α. Both quantities are related by $l_\nu \rho = N_i \alpha$, where ρ is mass density and N_i is the number of absorbers in state i[5]. The rationale for l_ν is analogous to what has been discussed for κ_ν. While κ_ν relates to the continuum, l_ν describes absorption for some line of interest. Integrating α over the entire spectrum gives us the fraction of energy per second per atom per steradian subtracted from the incoming radiation. For the Lorentz profile, integrated over wavelength, the result is (in cgs units):

$$\int_0^\infty \alpha \mathrm{d}\lambda = \frac{\pi q^2}{m_e c^2}\lambda^2. \tag{2.34}$$

The above result poses a problem. It imposes that the energy absorbed by some amount of atoms and, hence, line strength, increases with the wavelength squared. A simple visual inspection of the solar spectrum shows that this is not true, with neighbour doublet/triplet lines with almost the same value of λ showing different strengths. The result given by Eq. 2.34 may be corrected by multiplying its right-hand side by a quantity called *oscillator strength*, denoted by f. To understand its concept, let's define the equivalent width W_λ:

$$W_\lambda = \int_0^\infty \frac{F_{c,\lambda} - F_\lambda}{F_{c,\lambda}} \mathrm{d}\lambda, \tag{2.35}$$

---

[5] The absorbers need to be in a particular state to generate some transition. For instance, the absorption lines of the Balmer series are generated only by Hydrogen atoms in the second energy level.

where $F_{c,\lambda}$ is the continuum flux and F_λ the observed flux. In an optically thin gas, the equivalent width of a spectral line whose broadening profile is described only by natural broadening is equal to the integral in Eq. 2.34 times $N_i f$. Thus, for a given transition generated by number of N_i absorbers, the oscillator strength may be understood as the ratio between the observed equivalent width and the equivalent width predicted by the classical oscillator model. In the formalism of quantum mechanics, f is proportional to the matrix element describing the transition (Cohen-Tannoudji; Diu; Laloe, 1986), and is related to the Einstein coefficients of absorption, stimulated and spontaneous emission. Hence, it is a quantity tied to transition probability.

However, natural broadening is not the end of history. There are several processes influencing line profile (pressure broadening, stellar rotation broadening and others). We will now focus on two broadening mechanisms essential to weak[6] lines: thermal broadening and microturbulence.

The gas has some positive temperature, implying that the absorbers have some distribution of velocity of thermal origin. It is assumed, then, that this distribution is maxwellian. In the unidimensional line of sight, the number $N_v \mathrm{d}v$ of absorbers with velocity w.r.t. the observer between v and $v + \mathrm{d}v$ is given by:

$$N_v \mathrm{d}v = \frac{N_i}{v_m\sqrt{\pi}} e^{-(v/v_m)^2} \mathrm{d}v, \tag{2.36}$$

with:

$$v_m = \sqrt{\frac{2k_B T}{m}}, \tag{2.37}$$

being the modal speed of the Maxwell-Boltzmann distribution. The mass of the absorber is m, the gas temperature is T and k_B denotes the Boltzmann constant. In atmospheres of cool stars, v_m is of the order of a few km s^{-1}. The existence of absorbers with different radial velocities w.r.t. the observer implies the existence of different Doppler shifts in the observed spectrum. For sufficiently small velocities, i.e., $2k_B T \ll mc^2$, the Dopper shift relation may be written as $(\lambda - \lambda_0)/\lambda_0 = v/c$, with λ_0 being the wavelength in the rest frame. Defining:

$$\Delta\lambda_d = \lambda_d - \lambda_0 = \frac{v_m \lambda_0}{c}, \tag{2.38}$$

we have:

$$N_\lambda \mathrm{d}\lambda = \frac{N_i}{v_m\sqrt{\pi}} e^{-\left(\frac{\lambda-\lambda_0}{\Delta\lambda_d}\right)^2} \mathrm{d}\lambda. \tag{2.39}$$

---

[6] Optically thin.

The distribution of Doppler shifts is Gaussian. In case of negligible thermal or any effects other than natural broadening, the absorption profile is distributed in a Lorentzian curve. With thermal broadening, there are the same number of absorbers, but with an absorption profile distributed in a Gaussian curve. That is, the original Lorentzian profile of natural broadening *is smoothed* by a Gaussian. Mathematically, there is a convolution, and the result of the convolution between a Gaussian and a Lorentzian is a Voigt profile. In terms of the convolution, the absorption coefficient α – corrected by the oscillator strength – is written as:

$$\alpha = \frac{\pi q^2 \lambda^2 f}{m_e c^2} L(\lambda, \gamma) * G(\lambda, v_m), \tag{2.40}$$

with γ and v_m being proportional to the widths of their respective profiles. A Voigt profile dominated by the Gaussian has a strong core and weak wings, while a Lorentzian-dominated curve has strong wings – see Fig. 5 for an illustration. All broadening mechanisms have profiles described by a Gaussian or a Lorentzian, thus, the true shape of a spectral line is a Voigt profile[7]. To include these other mechanisms in the estimation of the Voigt profile, one needs only to correct γ and v_m to new values that account for the influence of these other mechanisms[8].

One example of these other mechanisms is the microturbulence v_t. The unidimensional nature of the atmospheric models adopted in works such as ours prevents us to peer into details of the turbulent behaviour of the gas. It is assumed the existence of small-scale turbulence cells which are not modeled by thermal broadening. The size of these cells is smaller than the mean free path of the photon, thus they may be treated as particles themselves, with their own distribution of velocities. This distribution is assumed gaussian, where v_t is equivalent to the v_m parameter of thermal broadening. To account for the microturbulence, one needs to add v_t to v_m by quadrature. The result is a larger Gaussian component of the Voigt profile. Hence, the transition between weak-line Gaussian-dominated profiles and saturated-line Lorentzian-dominated profiles is delayed and the spectral line needs more absorbers to saturate its core for greater values of v_t. The microturbulence is an atmospheric parameter and needs to be included as input in 1D atmospheric models.

Let's now turn our attention to the number of absorbers N_i. How do we estimate this value? First, we need to take a look at the line source function $S_l = j_{l,\nu}/l_\nu$ for a given transition between a lower level i and an upper level k. Writing the line absorption and

---

[7] For weak lines, it is very common that a Gaussian fits very well the line profile. This happens because, for these lines, the Gaussian-shaped broadening mechanisms dominate the Voigt profile.

[8] Because the convolution of two Gaussians is another Gaussian, and the convolution of two Lorentzians is a third Lorentzian.

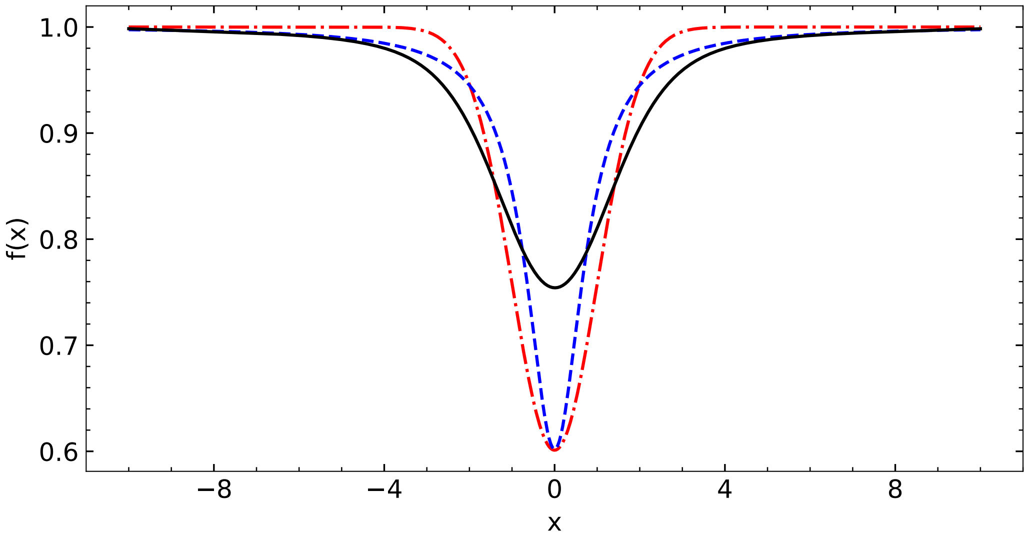

Figure 5 – Comparison of line profiles. *Red dash-dotted curve*: a Gaussian profile, with stronger core. *Blue dashed curve*: a Lorentzian profile, with stronger wings. *Black solid curve*: Voigt profile, the convolution of the other two. All profiles are normalized.

emission coefficients in terms of the Einstein coefficients, we have:

$$S_l = \frac{N_k A_{ki} \Psi(\lambda)}{(N_i B_{ik} - N_k B_{ki})\Phi(\lambda)}, \tag{2.41}$$

where $\Psi(\lambda)$ and $\Phi(\lambda)$ represent the wavelength dependence of emmited and absorbed photons, respectively. Using the well known identities between the Einstein coefficients, the line source function may be written as:

$$S_l = \frac{2h\nu^3 \Psi(\lambda)}{c^2[(N_i g_k)/(N_k g_i) - 1]\Phi(\lambda)}. \tag{2.42}$$

The above equation is the general case for the line source function. The g parameters are the statistical weights of the levels. We may restrict Eq. 2.42 to LTE if we impose S_l equal to the Planck function. This is achievable equalizing $\Psi(\lambda)$ and $\Phi(\lambda)$ – which is justifiable in equilibrium – and describing the ratio between the level populations with the Boltzmann excitation equation:

$$\frac{N_k}{N_i} = \frac{g_k}{g_i} e^{-\frac{h\nu}{k_B T}}. \tag{2.43}$$

The Boltzmann equation may be generalized as:

$$\frac{N_i}{N} = \frac{g_i}{Z(T)} e^{-\frac{\chi}{k_B T}}, \tag{2.44}$$

where N is the entire population of the atom/molecule in a given ionization state. The full population N_E of an atom needs the combination of Boltzmann and Saha to be evaluated. In the case of molecules, there is the need to account for molecular equilibrium as well, which is modelled through an equation whose functional form is similar to the Saha equation, with the dissociation energy substituting the ionization energy. Molecular equilibrum is calculated by a system of these equations whose size increases with the complexity of the molecule, because the number of possible combinations between the species composing the molecule increases. The quantity χ in Eq. 2.44 is called *excitation potential.* It represents the energy difference between the ground state and the initial level of the transition[9].

Combining Boltzmann, Saha and molecular equilibrium equations, we have an expression for N_i, and the evaluation of l_ν becomes possible. Both g_i, f and χ are transition-dependent. The first two are usually tabulated as $\log gf$, and all these values need to be given as input parameters, along with molecular dissociation energy in a line list when we are analysing spectra. From these equations we note that the population levels, and, hence, line strength, are dependent of temperature, pressure and, obviously, chemical composition.

The surflace flux, accounting for spectral lines, may be finally calculated:

$$F_\nu = \int_0^\infty B_\nu(T) E_2(\tau_\nu) d\tau_\nu \tag{2.45}$$

and τ_ν is evaluated from a pre-computed reference scale τ_0:

$$\tau_\nu(\tau_0) = \int_{-\infty}^{\log\tau_0} \frac{l_\nu + \kappa_\nu}{\kappa_0} t_0 \frac{\mathrm{d}\log t_0}{\log e}. \tag{2.46}$$

Accounting for the l_ν coefficient of several spectral lines at the same time turns possible to build a full synthetic spectrum. Convolving this synthetic spectrum with an instrumental profile allows us to compare the synthetic and the observed spectra.

2.2 The echelle spectrograph

There are several methods to disperse the light from a source in its spectrum and record it. Although it is not in the scope of this work discussing the fundamentals of this

---

[9] For instance, in the case of Balmer absorption lines, $\chi = 10.2$ eV, which is the difference between the first and second levels of Hydrogen. Absorption lines from the Lyman series have $\chi = 0$ eV.

branch of optics, in this section we will make a brief digression on echelle spectroscopy. We intend to give the reader a minimal notion on how the instrument used for data acquisition works. For a more in-depth discussion on spectroscopic techniques, the reader is referred to books such as Eversberg & Vollmann (2015), Gray (2005) and Léna et al. (2012), from which the content of this section is based.

Except for slitless spectroscopy, a general astronomical spectrograph consists on an entrance slit receiving electromagnetic radiation (hereafter, 'light'), followed into the optical path by an optical device which collimates the received light into a diffraction grating. The diffracted light is, then, directed to a camera mirror which focuses the resulting spectrum into a detector. The echelle spectrograph is based on a diffraction grating built from grooves (blazed grating) evenly spaced by a distance d, and, thus, its dispersion can be modelled from the grating equation for a reflective grating:

$$m\lambda = d(\sin\alpha + \sin\beta), \tag{2.47}$$

where α is the angle of incidence of the incoming beam of light w.r.t. the normal of the grating surface and β is the respective angle of diffraction of the outgoing light. The grating diffracts the light, with the multiple grooves creating an interference pattern. For a given monochromatic beam of wavelength λ the interference is fully constructive if the path difference $d(\sin\alpha + \sin\beta)$ between the beams diffracted by two grooves is an integer multiple m of λ. Thus, for a given incoming monochromatic beam, the grating diffracts the outgoing beams in multiple angles β_m, each beam belonging to a spectral *order*. For order zero ($m = 0$), $\beta_0 = -\alpha_0$, and the beam path follows the reflection law of geometric optics. If the light source is extended, its spatial profile in the direction parallel to the entrance slit will be reproduced after diffraction. For instance, if light of two resolved point sources pass by the slit, the detector will register two spectra, both separated in the spatial axis. Sufficiently extended 'monochromatic' sources such as sky emission lines are recorded in the detector as images of the entrance slit.

The efficiency of the grating can be improved for a specific wavelength by building the grooves in such a manner which both the direction of constructive interference and specular reflection are the same. The direction of specular reflection requires that, for a blaze angle Θ_B:

$$\alpha - \Theta_B = \beta + \Theta_B, \tag{2.48}$$

in which the blaze angle is the angle between the grating normal and the groove surface normal. If we assume the *Littrow condition* $\alpha = \beta = \Theta_B$, Eq. 2.47 becomes:

$$m\lambda = 2d\sin\Theta_B. \tag{2.49}$$

The Eq. 2.47 may be generalized for the case where the plane generated by the incoming and outgoing beams is tilted by an angle γ w.r.t. the orientation of the grating, i.e., w.r.t. to the plane generated by the normal of the grating surface and the normal of the blaze surface. Then, the grating equation may be rewritten as:

$$m\lambda = d\cos\gamma(\sin\alpha + \sin\beta). \tag{2.50}$$

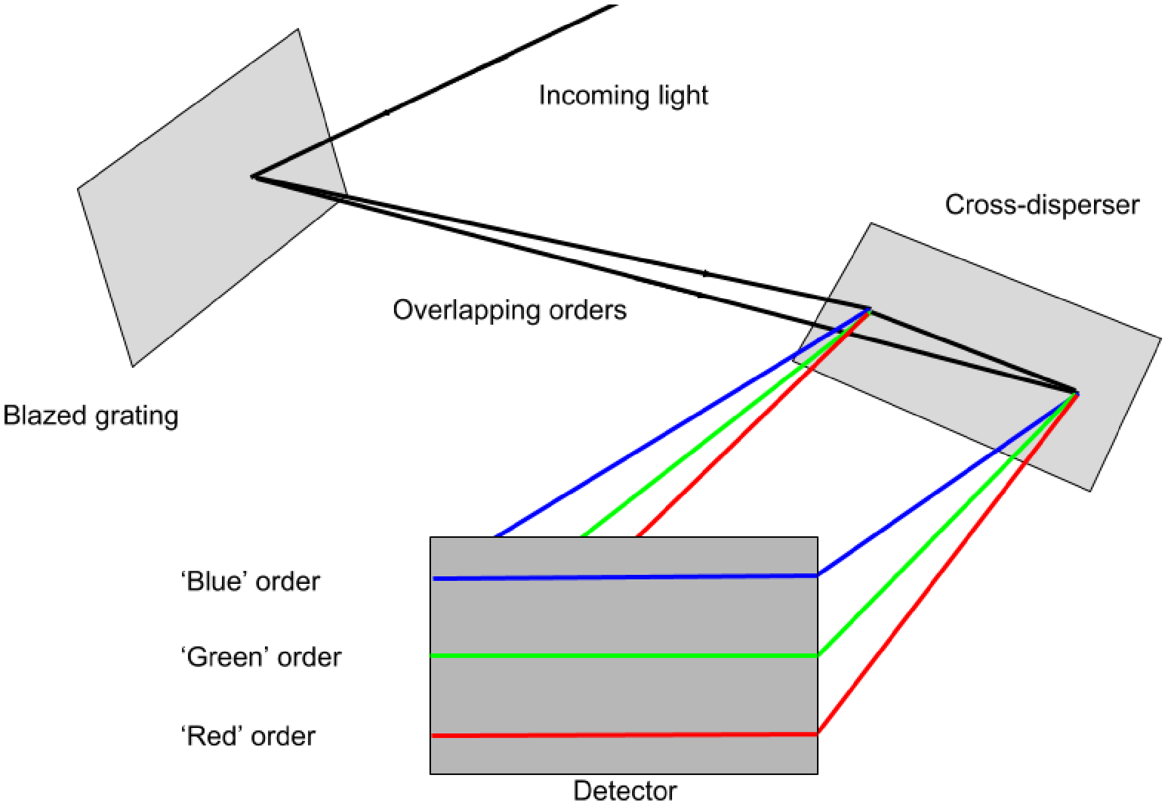

Figure 6 – Schematic view of the echelle spectrograph. The incoming light enters by a slit (not shown), and the high orders dispersed by the blazed grating are then separated by the cross-disperser.

Taking the derivative of β w.r.t. λ in Eq. 2.50 we have the angular dispersion of the grating:

$$\frac{d\beta}{d\lambda} = \frac{m}{d\cos\gamma\cos\beta} = \frac{\sin\alpha + \sin\beta}{\lambda\cos\beta}. \tag{2.51}$$

implying that angular dispersion is proportional to the order number. In the Littrow configuration, Eq. 2.51 becomes:

$$\frac{d\beta}{d\lambda} = \frac{2}{\lambda}\tan\Theta_B. \tag{2.52}$$

From Eq. 2.52 we take the information that large blaze angles yield large angular dispersions, which are useful for high-resolution spectroscopy. Indeed, echelle spectrographs use such large ($>$ 45 degrees) blaze angles. Thus, a spectrograph can be optimized to high dispersion through the use of higher orders and large blaze angles.

One should note that the blaze angle is constant for a grating, and, thus, according to Eq. 2.49 – or Eq. 2.50 if we make α and β constant – the product $m\lambda_B$, where λ_B is the blaze wavelength, is also a constant. The consequence is that, for a given dispersion angle, the spectral orders overlap, and the maximum efficiency wavelengths for a given blaze angle become closer with a rate of $1/m^2$. The solution is to insert another diffraction grating (or a prism) in the optical path, the cross-disperser, whose dispersion direction is perpendicular to that of the echelle grating. The cross-disperser separates the different orders in (ideally) parallel bands in the detector – see Fig. 6. In reality, the result on the detector consists of a parabolic spectral axis and a tilted spatial axis due to the geometry of the echelle + cross-disperser system. Both aberrations can be attenuated by rotating the slit w.r.t. to the camera of the instrument, and they are fully corrected in the process of data reduction.

2.3 Observations and data reduction

The data under analysis in this work has been taken from medium-to-high-resolution, high signal-to-noise ratio ($\geq$ 150) near-infrared spectra of 27 stellar targets, listed in Table 1. The images were obtained in two full nights with the Near InfRared echelle SPECtrograph (NIRSPEC) on the 10-m Keck II Telescope, located at the summit of Mauna Kea, Hawaii. NIRSPEC (McLean et al., 1998) is a cross-dispersed echelle spectrograph which uses an ALADDIN-3 InSb 1024x1024 array as detector, covering a spectral range in the near-infrared (9500-55000 Å). The instrument has both low- (R = $\lambda/\delta\lambda \sim 2500$) and high-resolution (R $\sim$ 25000) modes, the later being the chosen configuration for the current observations. In high resolution mode, the image scale is 0.144"/pixel in the spectral axis and 0.193"/pixel in the spatial axis. That is, for a slit width of 0.432", each (spectral) resolution element contains three pixels.

Spectra were acquired in H- and K-bands, employing the N-5 and N-7 filters, which are centered at 15873.3 and 21768.7 Å, respectively. The resulting images have 9 observed spectral orders in the H-band, covering $\sim$ 200 Å in each order, resulting in a spectral interval ranging from $\sim$ 14250 to 17000 Å. The echelle (blaze) and cross-disperser angles were, respectively, 62.66 ($m\lambda_B = 76.29$ μm) and 36.24 degrees. In the K-band, 6 spectral orders were observed, covering $\sim$ 300 Å individually, giving a spectral interval from $\sim$ 21200 to 24900 Å. The echelle and cross-disperser angles used in K-band observations were, respectively, 63.84 ($m\lambda_B = 77.08$ μm) and 36.09 degrees. The orders are separated by gaps of non-observed spectra – see Appendix A.2 for the available spectral intervals.

The observations were carried out on December 2013, using special observing time from the Australian National University, under program ID Z282NS, with Alan Alves Brito – the supervisor of this work – registered as the Principal Investigator. In the first night, a total of 313 images were acquired in the K-band. Science images for 25 targets, telluric standards and other exposures for calibration purposes were acquired as well, with average seeing of 0.48 arcseconds, implying a slit-limited spectral resolution. The observations were impaired in the second night by bad weather: the dome was closed by four hours due to high humidity, and only 200 images of 16 science targets, telluric standards and calibration exposures were taken. No seeing estimation is recorded for the second night. The calibration images consist of flat field frames (see discussion about flat fielding ahead) and two sets of arc lamp images per night – one set at the beginning, the other set at the end. No bias or dark frames were taken.

Table 1 – Program stars, coordinates, 2MASS photometry and observed bands (H, K or both). In the last column the classification used in this work is shown. The status of HR 8878 will be discussed in Ch. 3.

ID	RA (J2000) (hms)	Dec (J2000) (dms)	J (mag)	H (mag)	K_s (mag)	Bands	Class.
HD 224959	00 02 08.0224	-02 49 12.239	7.863	7.432	7.303	H,K	CH-star
HD 26	00 05 22.2077	+08 47 16.096	6.540	6.106	6.032	H,K	CH-star
HE 0002+0053	00 05 24.9992	+01 10 03.824	11.018	10.386	10.118	K	CEMP
HE 0017+0055	00 20 21.5999	+01 12 06.814	9.309	8.698	8.498	H,K	CEMP
HD 5223	00 54 13.6094	+24 04 01.522	6.372	5.845	5.673	H,K	CH-star
HD 5424	00 55 43.9269	-27 53 37.267	7.664	7.148	7.015	K	Ba-star
BD 44	02 26 49.7388	+44 57 46.526	7.659	7.269	7.202	H,K	CEMP
HE 0310+0059	03 12 56.9141	+01 11 09.602	9.871	9.296	9.196	K	CEMP
HIP 17766	03 48 11.8635	+07 08 46.476	8.273	7.624	7.509	H,K	Hyades
HIP 19082	04 05 25.6704	+19 26 31.746	8.889	8.259	8.107	K	Hyades
HIP 19316	04 08 26.6673	+12 11 30.646	8.818	8.171	8.046	K	Hyades
HD 27271	04 18 33.8263	+02 28 13.914	5.839	5.373	5.270	H,K	Ba-star
HIP 21138	04 31 52.4722	+15 29 58.133	8.667	8.034	7.895	K	Hyades
HIP 21256	04 33 37.1805	+21 09 03.064	8.427	7.835	7.686	H,K	Hyades
outer 1	04 34 29.9237	+03 06 01.449	9.579	8.760	8.599	K	Outer disc
outer 2	04 37 30.5963	-00 15 00.429	9.390	8.640	8.491	K	Outer disc
outer 3	04 50 16.4864	-03 25 01.532	9.243	8.510	8.361	K	Outer disc
outer 16	06 58 26.2870	+09 13 58.335	9.543	8.750	8.599	H,K	Outer disc
outer 17	07 03 02.9760	+08 13 10.733	9.832	9.066	8.918	H,K	Outer disc
outer 18	07 04 51.6820	+08 29 16.659	9.532	8.770	8.604	H,K	Outer disc
outer 19	07 22 00.4550	+07 21 51.476	9.367	8.600	8.494	H,K	Outer disc
outer 20	07 22 23.6070	+07 26 10.531	9.358	8.590	8.476	H	Outer disc
M67-0141	08 51 22.8037	+11 48 01.780	8.560	8.070	7.942	K	M 67
M67-0223	08 51 43.8875	+11 56 42.531	8.618	8.110	8.000	K	M 67
μ Leo	09 52 45.8162	+26 00 25.021	1.930	1.327	1.220	H	Other
HD 210946	22 13 50.1539	+01 36 32.150	6.332	5.837	5.666	H,K	Ba-star
HR 8878	23 20 20.5830	+05 22 52.700	2.891	2.120	1.993	H,K	Ba-star???

Data reduction was performed with the version 0.9.17 of the NIRSPEC Data

Reduction Pipeline[10] (NSDRP) for flat fielding, cosmic ray cleaning, order location, tracing, rectification and extraction. The rationale behind data reduction of a spectroscopic image is the transformation of a 2D raw data image composed of signal from both the target, the instrument (e.g., dark current), the sky and other processes (e.g., cosmic rays) into a 1D reduced spectrum composed of, *ideally*, only the target signal.

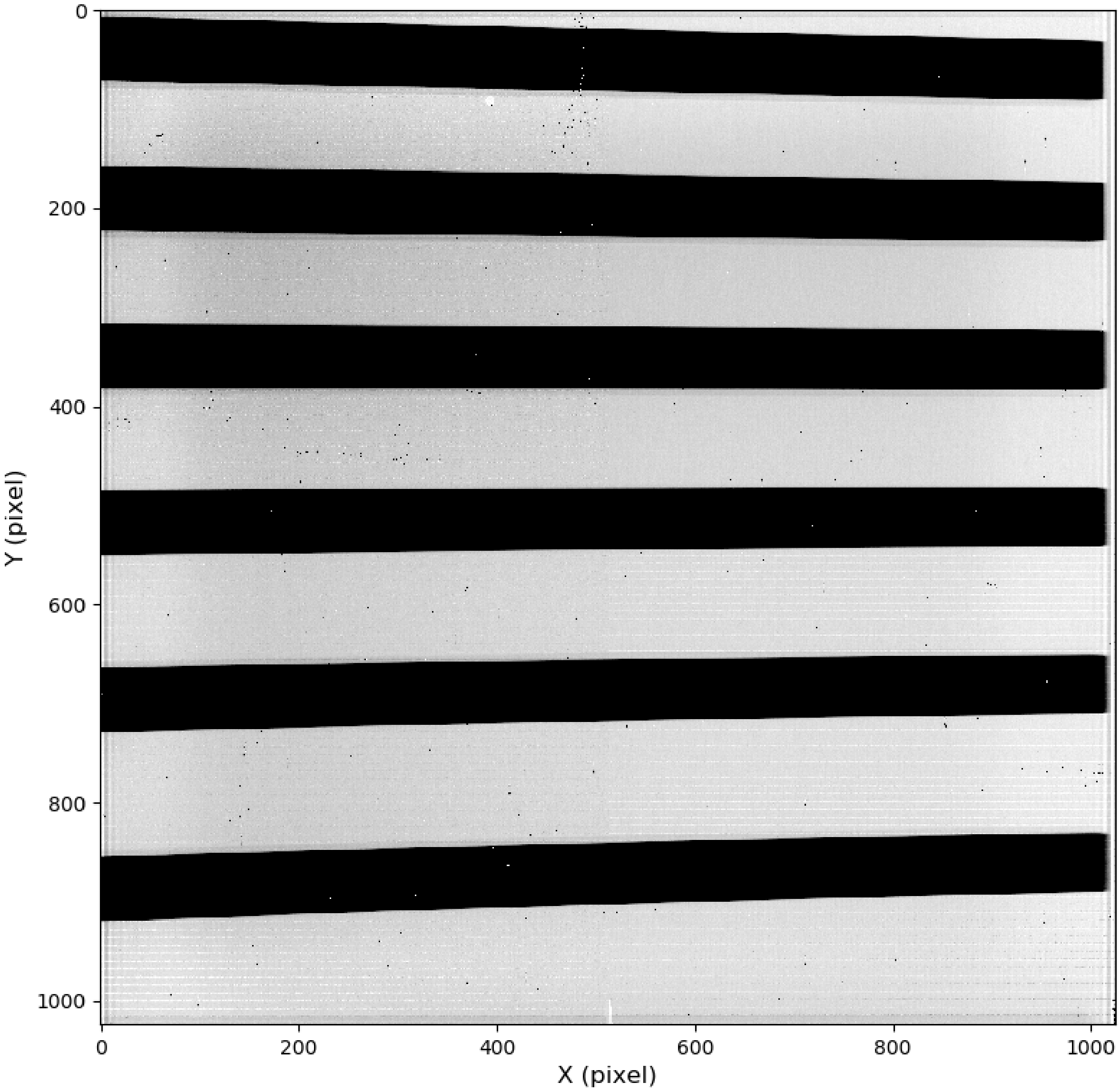

Figure 7 – Negative image of the master flat used in K-band data reduction. The black bands are the illuminated areas, i.e., the regions on the detector ocuppied by the echelle orders. The upper and lower borders of the black bands are used to find the traces of the orders. The abscissae have the spectral axis, while the ordinates have the spatial axis.

---

[10] <https://www2.keck.hawaii.edu/koa/nsdrp/nsdrp.html> (accessed on 10.11.2018).

Flat fielding is required because the quantum efficiency of the detector and optical transmission of the system fluctuate spatially (Léna et al., 2012). An usual correction technique consists in acquiring frames from a uniformly illuminated field with the same instrumental configuration used throughout the observation. Then, the series of flat field frames are averaged in a master flat frame – usually by the median – to minimize the noise. Considering that the only relevant source of inhomogeneity in the master flat is the unwanted spatial fluctuation in the resulting counts, the science frames are 'flat-fielded' dividing them by the master flat. Indeed, in the observations carried out with NIRSPEC, flat field frames were acquired at the beggining and the end of both nights, a total of eight per night. The NSDRP used these flat frames to create a master flat for each night of observation, and then flat-fielded the other frames[11].

The pipeline also employs the flat frames to locate the region of the detector occupied by the observed echelle orders. After finding the regions of the detector associated with each order, the NSDRP locates the order borders for each pixel column using the count profile of the flat frame. The flat frames have $\sim$ 6000 counts per pixel in the illuminated areas – the areas associated with the echelle orders – against a few hundred counts per pixel in the non-illuminated areas. Fig. 7, which shows a flat frame, illustrates the order borders. After finding the locations of the order borders in a flat frame, the pipeline applies these borders for all object frames acquired with the same instrumental configuration. Then, cosmic ray cleaning is performed and the reduction proceeds order-by-order.

For each order, the code averages the pixel coordinates from lower and upper borders of each pixel column, generating a set of 'mean coordinates'. Then, it produces a polynomial fit of these mean coordinates. This polynomial fit is the *trace*, and its purpose is to rectify the echelle order in the spatial axis – in Figs. 8 and 10 the curvature in the spatial axis is evident for some orders.

In addition to spatial axis rectification, a similar procedure must be performed in the spectral axis. The spectral axis is subject to shear, related to the geometry of the instrument according to the pipeline documentation. As a result, some spectral lines can show a spurious broadening (see Fig. 9 for a simulation). Also, the OH sky emission lines present in the spectra are slightly tilted after rectification in the spatial axis. The pipeline exploits this tilt to eliminate the shear and finish the order rectification by tracing the OH lines.

However, not all observed spectra had OH lines strong enough to be identified (see, e.g., Fig 10), and rectification in the spectral axis was not performed by the pipeline in orders lacking these sky features. Several of the exposures taken were not long enough to show these emission lines. We tried to circumvent this issue because one of the orders

---

[11] Detailed explanation on NSDRP can be found at <https://www2.keck.hawaii.edu/koa/nsdrp/documents/NSDRP_Software_Design.pdf> (accessed on 10.11.2018).

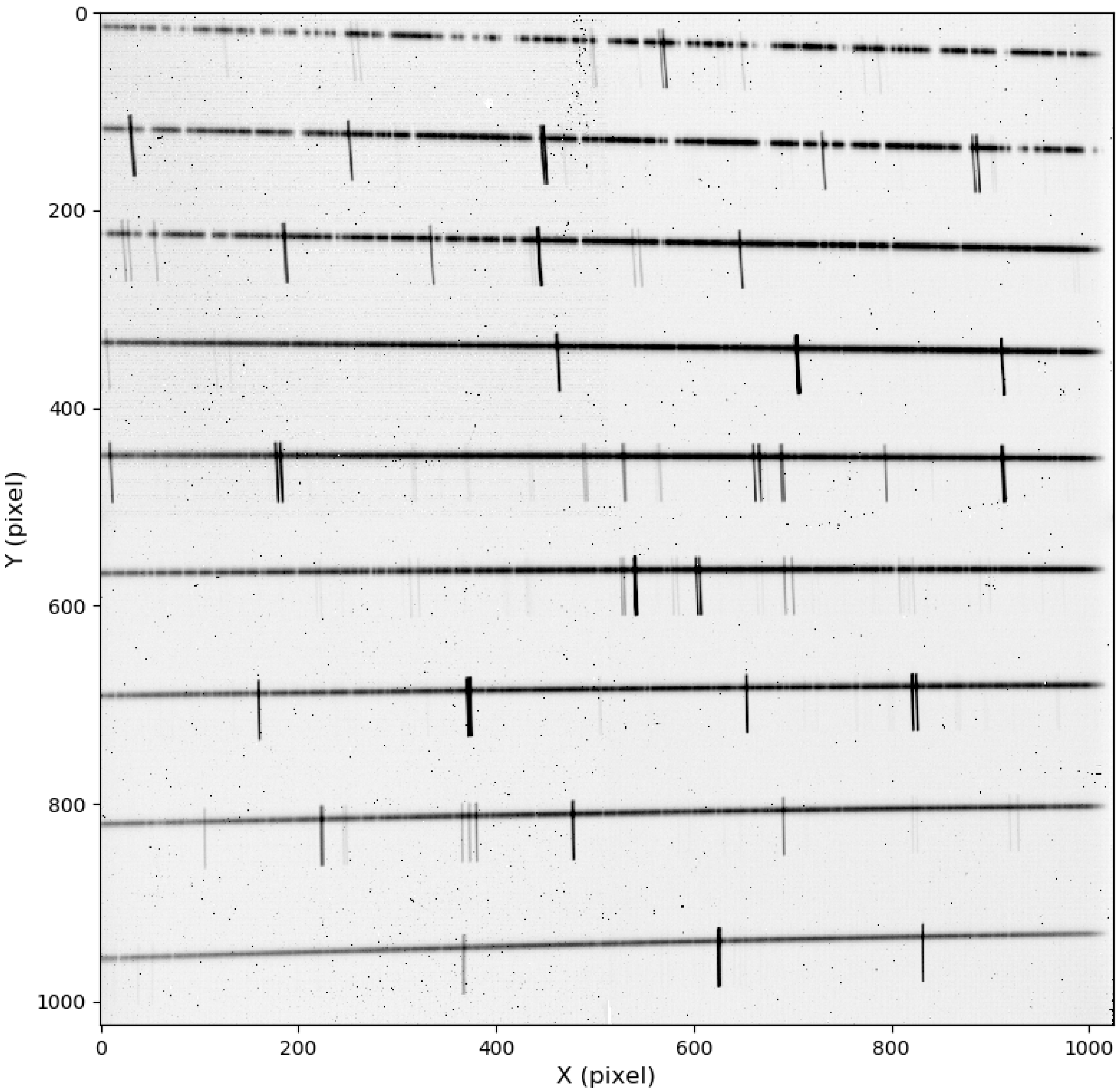

Figure 8 – Negative raw image of the H-band from star outer 17 ($H = 9.066$ mag), exposition number 153 from the night of 16.12.2013. Exposure time is 150 seconds per coadd. The echelle orders, from bottom to top, are the orders 45 to 53. The grayscale is saturated at 1024 counts to highlight the OH sky lines.

most affected by the lack of OH calibration features is order 33. This corresponds to the spectral region where is located the HF 1-0 R9 line, needed for the measurement of F abundances. Even the faintest observed object – i.e. the target with the longest exposure times (300 s per coadd), star HE 0002+0053, had no detectable OH lines in order 33, preventing rectification by the pipeline. Indeed, the inspection of the OH night-sky atlas from Rousselot et al. (2000) confirms the lack of strong sky lines in this spectral region, thus longer exposures are needed for proper identification of OH telluric features in the

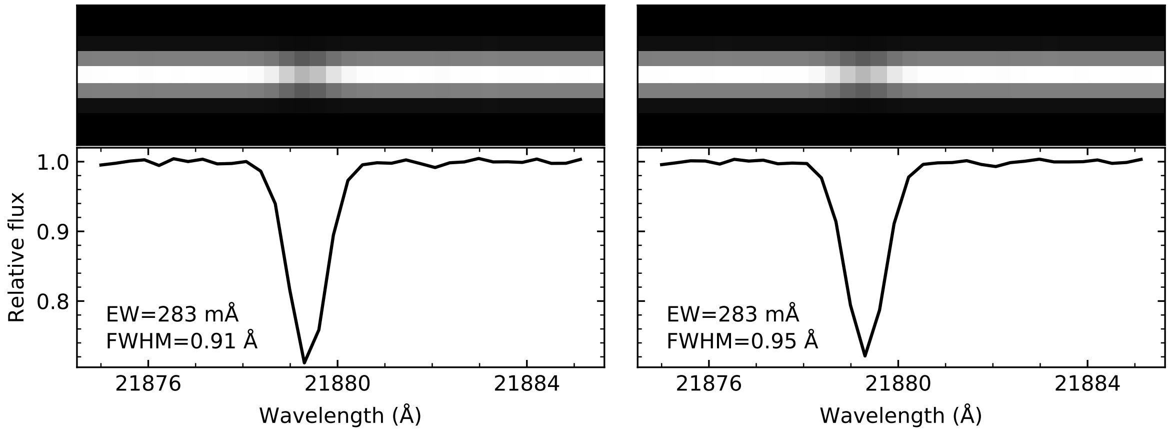

Figure 9 – Simulation of shear in the spectral axis. The images show simulated 2D spectra with R $\sim$ 25000 rectified in the spatial axis and, below, their respective reduced 1D spectra are plotted. Both images show the same spectrum, but the right one has shear with an inclination angle of 3 degrees. In spectra where the NSDRP was able to trace the sky lines, typical inclination angles range from 1 to 3 degrees. Despite the mild ($\sim$ 4 %) broadening observed due to shear, the equivalent width is preserved.

interval comprising the HF line. Since the equivalent widths are preserved in case of uncorrected shear (for shear slopes $\ll 1$), the adopted strategy was to control for line broadening. Features in regions where FWHM was much larger than λ/R were discarded, under the assumption that only severe broadening would affect the equivalent widths, and mild broadening was taken into account in the spectral synthesis.

After rectification, the reduction proceeds to subtract the signal from the sky – the background – leaving, ideally, only the target signal. Two 'sky windows' are defined on the wings of the spatial profile of the spectrum, which is fitted by a gaussian function. This fit helps to define an extraction window, from where the signal is going to be collapsed in an 1D spectrum. The counts of the sky windows are averaged in a 'pedestal', which is then subtracted, leaving only the extraction window and its immediate neighbour pixels with nonzero counts[12]. After the background subtraction, the row pixels in the extraction window of each pixel column are summed up to form the 1D spectrum. For NIRSPEC, due to the detector array size of 1024x1024 pixels, each order has a resulting 1D spectrum consisting of 1024 points. Each point carries the background-subtracted signal of the extraction window of its corresponding pixel column collapsed in one value.

The next step in data reduction consists in the transformation of the detector array

---

[12] Of course, the description has been simplified for an image with infinite signal-to-noise ratio. The image usually has small nonzero – and negative – counts in the sky regions after background subtraction.

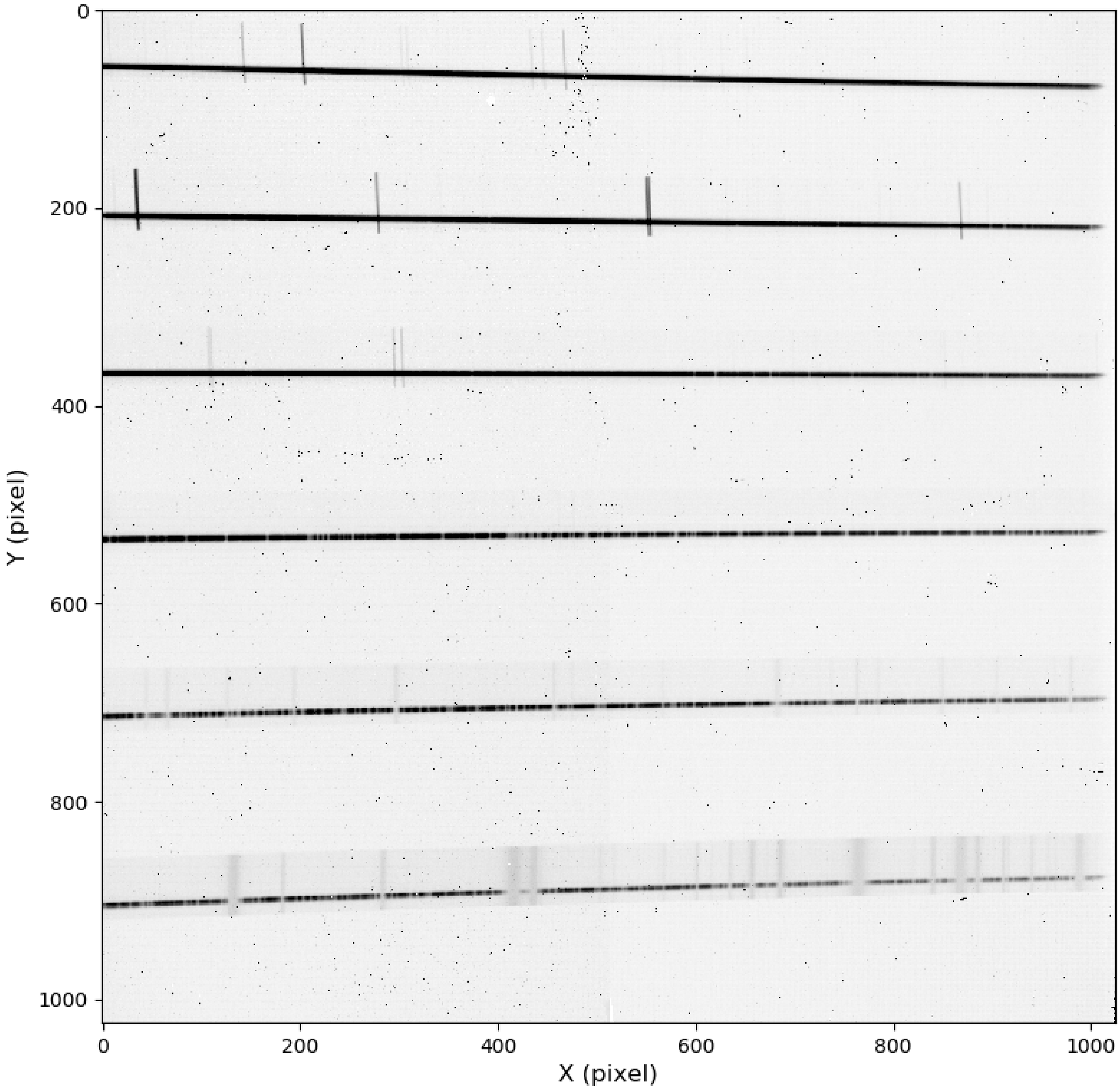

Figure 10 – Negative raw image of the K-band from star outer 1 (K_s = 8.760 mag), exposition number 203 from the night of 15.12.2013. Exposure time is 90 seconds per coadd. The echelle orders 31 to 36 are ordered from bottom to top, as for H-band orders in Fig. 8, and the grayscale is saturated at 1024 counts as well. Notice the lack of detectable OH sky lines in orders 33, 32 and 31: automated rectification in spectral axis and wavelength calibration have failed for these orders. The CO 3-1 band is clearly visible on order 33 (Y ≈ 520) from X ≈ 400 onwards.

pixel scale into a wavelength scale with physical significance. NSDRP uses the position of OH telluric emission lines for wavelength calibration because they are in the observer rest frame, i.e., they are not affected by doppler shift. However, most exposures were too short for proper identification of these calibration features in all echelle orders, as previously discussed. Inspecting the spectra of the telluric standards, we have found that the position of the telluric absorption features drifted in a non-linear manner in the pixel scale during each night of observation. This drift prevents the use of arc lamp images, because these images were taken only at the beggining and the end of each night. An effective lamp calibration would need one arc lamp for each science and telluric standard image to avoid significant differences between the pixel-to-true-wavelength scales of the arc lamp and of the calibrated images.

To circumvent the lack of proper wavelength calibration data, an ad hoc routine was written in Python language (Rossum, 1995) for the specific purpose of calibrating the pixel scale delivered by the NSDRP into a wavelength scale. The code makes use of the SciPy, NumPy, Matplotlib and AstroPy packages (Jones et al., 2001; Oliphant, 2015; Hunter, 2007; Astropy Collaboration et al., 2013; Price-Whelan et al., 2018). The routine starts loading the spectrum from the echelle order to be calibrated, a line list of telluric calibration features and the atmospheric transmission template available at the Gemini Observatory website[13]. Since the template is normalized, the to-be-calibrated spectrum is roughly normalized by a low-order polynomial fit in order to facilitate the visual comparison of both spectra. This rough normalization does not survive the process and is not saved after the code finishes the calibration. Then, the object spectrum is oversampled by interpolation using a cubic spline. The oversampled spectrum is then used to find the minima of the calibration lines, which had been previously located by visual inspection, in (fractional) pixel coordinates. The lines from the calibration line list are expected to be symmetric, thus the process is analogous to finding the line centroid. Then, the relationship between the pixel coordinate of the telluric line in the object spectrum and its theoretical wavelength from the line list is interpolated using another cubic spline. The interpolation is generated with the *UnivariateSpline* class from the SciPy package. This process creates a Python object which represents a function $f = \lambda(\text{pixel})$. A smoothing is applied to the cubic spline in order to prevent two or more pixels from giving the same wavelength value, which can happen in the extrapolated regions depending on the behaviour of the interpolated function on the borders of the interpolated regions. The routine starts with a smoothing factor of 0.1 and chooses the smallest value that generates a monotonic function all over the interpolated/extrapolated range. Then, the function is sampled to find the corresponding wavelength for each integer pixel value from the original pixel scale. A smoothed interpolation was chosen over a linear or polynomial fit because it gives better results on the extremes of the order (pixels 0, 1023 and their neighbours), minimize the residuals and optimize the process of telluric subtraction, discussed ahead. The last actions of the Python routine are saving a plot with a comparison between object and template spectra and saving the wavelength scale in pixel coordinates to an ASCII

---

[13] <http://www.gemini.edu/sciops/telescopes-and-sites/observing-condition-constraints/ir-transmission-spectra> (accessed on 10.11.2018).

file. This whole process was repeated for each of the 2530 spectral orders calibrated.

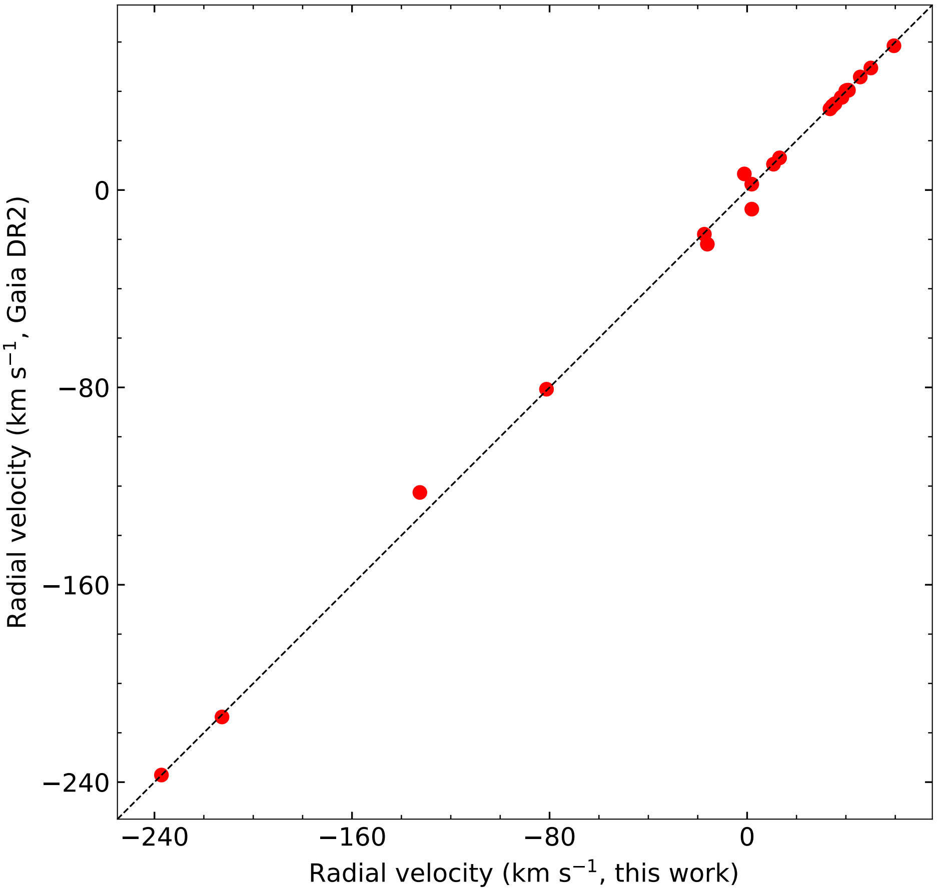

Figure 11 – Comparison between velocities measured with our spectra (horizontal axis) and those published by Gaia DR2 (vertical axis). The error bars are smaller than the circles, thus they are not shown. The black dashed line is the identity function. All 23 measurement pairs differ by less than 10 km s^{-1}, and 19 measurement pairs have differences ≤ 1 km s^{-1}.

Later, for each reduced echelle order, the wavelength scale and the (uncalibrated) flux values were exported to a .fits file through the IRAF task *rspectext*. The template telluric spectrum uses wavelength values in vacuum ($\lambda_{\rm vac}$), while most works dealing with high-resolution stellar spectroscopy use air wavelength ($\lambda_{\rm air}$)[14]. The transformation between vacuum and air wavelengths is:

$$\lambda_{\rm air} = \frac{\lambda_{\rm vac}}{n}, \tag{2.53}$$

---

[14] For instance, the HF 1-0 R9 line has $\lambda_{\rm vac} = 23364.70$ Å and $\lambda_{\rm air} = 23358.33$ Å.

where n is the air refraction index, calculated using the eq. (8) from Morton (2000):

$$n = 1 + 8.34254 \times 10^{-5} + \frac{2.406147 \times 10^{-2}}{130 - s^2} + \frac{1.5998 \times 10^{-4}}{38.9 - s^2}, \tag{2.54}$$

and s is $10^4/\lambda_{\rm vac}$ for wavelength in angstroms.

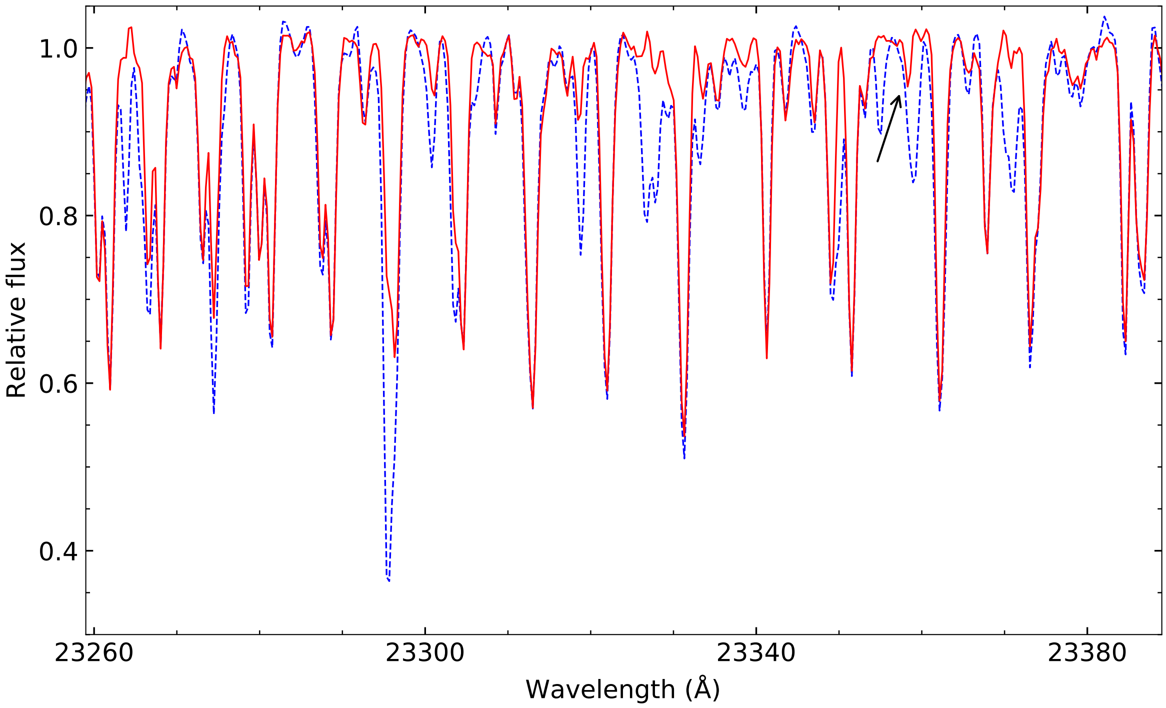

Figure 12 – A portion of the spectra of the star HD 5223. *Blue dashed line*: (doppler corrected) spectrum with telluric features. *Red solid line*: telluric subtracted spectrum. For this object – with observed radial velocity of -211.7 km s^{-1} – the 1-0 R9 HF line, marked with an arrow, fell inside a telluric feature. Its presence was revealed only after the subtraction.

With the wavelengths in $\lambda_{\rm air}$, the validation of the wavelength calibration was later carried out by measuring the heliocentric radial velocities of the targets and comparing with velocities available in the literature. Radial velocities were measured in orders 33, 49 and 50 of each target (when available) using the IRAF task *rvidlines*. Fig. 11 shows a comparison between the values from this work and those from the literature.

After creating the .fits files with the 1D spectra appropriately scaled in wavelength, we proceeded with the normalization of the spectra, in an (echelle) order-by-order basis. The normalization was performed with the IRAF task *continuum*. Each spectrum was normalized using the Legendre polynomial which minimized the residuals. The spectrum received visual inspection before saving the result, to confirm the inexistence of spurious

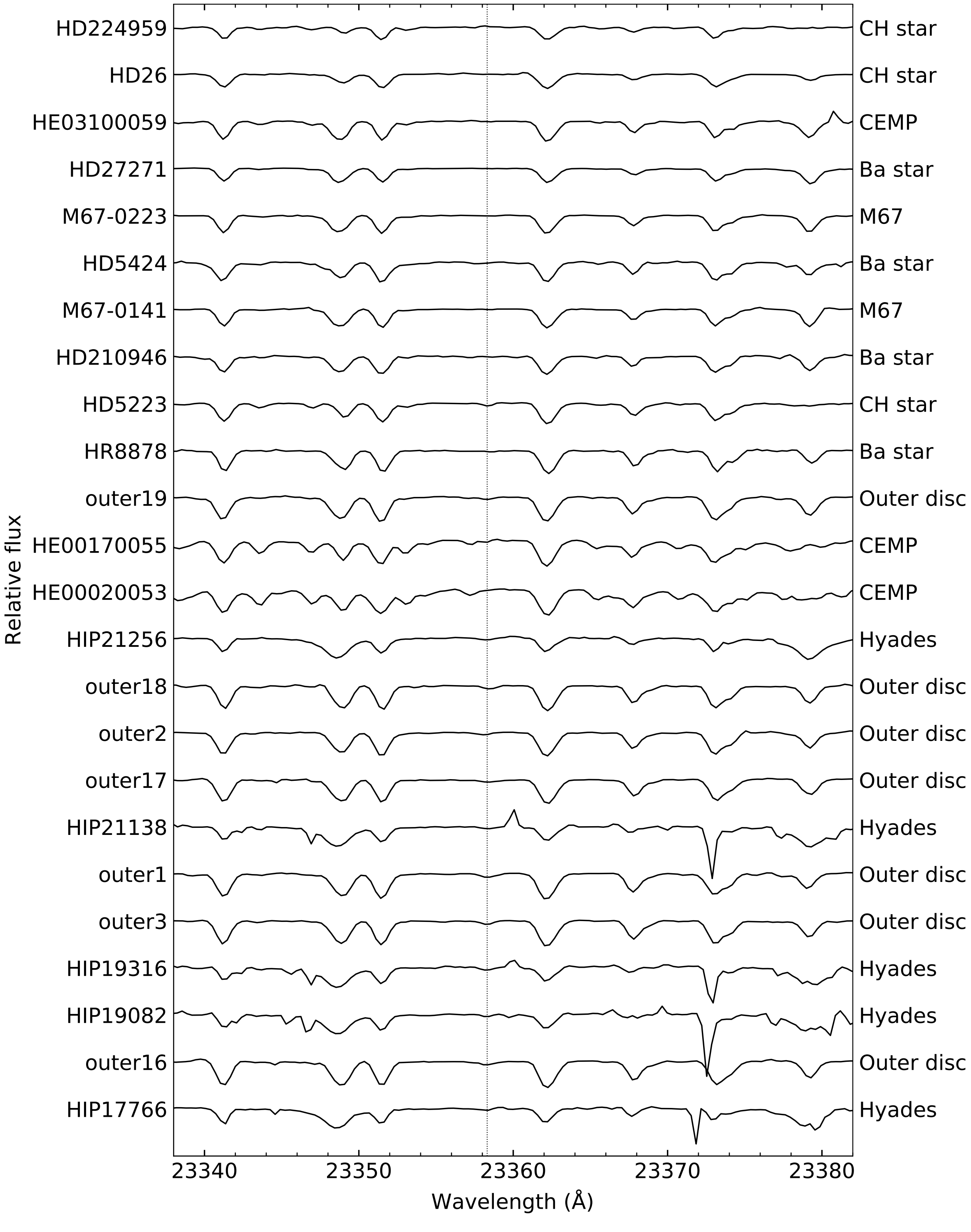

Figure 13 – A portion of the spectra in the K band, ordered by $T_{\rm eff}$, showing 2-0 CO, 3-1 CO features and the 23379 Å Na doublet. The dashed line marks the position of the 1-0 R9 HF feature.

trends in the fit, a critical factor in polynomial fits which used higher (> 6) orders. After normalization, spectra reduced from multiple exposures of the same object were coadded with the IRAF task *scombine* in one single 1D spectrum for each echelle order to improve final signal-to-noise ratio.

The telluric subtraction was performed by another Python routine written for this purpose. In short, the telluric subtraction works dividing the target spectrum by the spectrum of a telluric standard observed in the same night with the same intrumental configuration. The routine algorithm follows the procedure described in the documentation of the IRAF task *telluric*[15]. Both target spectrum and the spectrum of the telluric standard – hereafter the 'calibration spectrum' – are loaded. The minimum flux of the calibration spectrum is set to a threshold slightly greater than zero, to avoid division by non-positive values. Then, the calibration spectrum is shifted in the wavelength axis to eliminate any eventual relative shift of the telluric lines between target spectrum and calibration spectrum. The shift value is chosen minimizing the RMS of the division of the target spectrum by the calibration spectrum. This first division is performed only to determine the wavelength shift and is discarded.

Different airmasses impact the line profile of the observed telluric features, so any difference between airmass values of target and calibration spectra must be taken into account. The Python routine, after the wavelength shift, transforms the calibration spectrum through:

$$F'(\lambda) = (F(\lambda))^{s\frac{A_t}{A_c}} \tag{2.55}$$

where F(λ) is the flux at wavelength λ, A$_t$ and A$_c$ are, respectively, the airmass values for target and calibration spectra and s is a scale factor which minimizes the RMS of the division of both spectra. The code gives an option to choose manually the values of shift and scale factor, if the operation based on RMS minimization is unsatisfactory. The division is made after the interpolation of both target and scale-shifted calibration spectra into Python UnivariateSpline objects. Finally, the routine samples the resulting Python object in the wavelength array of the target spectrum and saves the telluric subtracted flux into a .fits file. An example of telluric subtraction is shown in Fig. 12.

The last step in data reduction process is doppler correction to the rest frame, executed through the IRAF task *dopcor*. The radial velocities with respect to the observer[16] measured through different echelle orders were averaged for each night for each star. The correction from the observed wavelength λ_{obs} to the rest wavelength λ_{rest} is made using the relativistic doppler equation:

$$\lambda_{\text{rest}} = \lambda_{\text{obs}}\sqrt{\frac{1+\frac{v}{c}}{1-\frac{v}{c}}} \tag{2.56}$$

---

[15] <http://stsdas.stsci.edu/cgi-bin/gethelp.cgi?telluric> (accessed on 10.11.2018).

[16] That is, the observed radial velocities, not the heliocentric ones.

where v is the observed radial velocity and c is the speed of light. The observed radial velocities were used as input for the task and the final results were saved in .fits files. Fig. 13 shows a portion of the fully reduced spectra around 23360 Å.

2.4 Analysis

While this work focuses on F, we took advantage of the total observed spectral interval, and abundance ratios of light (CNO, Na, Al, K), alpha (Mg, Si, Ca, Ti), Fe-peak (V, Cr, Mn, Co, Ni) and s-process (Ce) elements have been calculated as well. The targets are divided between 16 *normal* (dwarfs from the Hyades, RGB stars, M 67 subgiants) and 11 *peculiar* objects, including Carbon-Enhanced Metal-Poor (CEMP), CH- and Ba-stars. The normal stars are located in the Galactic disc – solar neighbourhood and outer disc, and the peculiar objects were chosen due to their characteristics. As previously mentioned, the targets in the outer disc were studied with optical spectra by Bensby et al. (2011) (see also Bensby et al. (2010)) – the numbering in their IDs corresponds to their ordering in table 1 from Bensby et al. (2011).

2.4.1 Kinematics

The kinematics presented in this work were derived from Gaia DR2 astrometry (Gaia Collaboration et al., 2018). The 6-parameter astrometric solution – right ascension, declination, parallax, proper motions and radial velocity – was converted to cartesian coordinates in the Galactocentric rest frame – positions X, Y, Z and velocities U, V, W. Two stars lack radial velocity measurements in Gaia DR2, outer 17 and μ Leo. For the former we used radial velocities from our spectra and for the later we adopted the value from Famaey et al. (2005) – due to its smaller uncertainties, respectively. We did not take into account the -0.029 mas zero-point offset in parallax reported by Lindegren et al. (2018) in the results presented in Tables 7, 9 and 14. The value of this zero-point correction is smaller than the published uncertainties in parallax for all objects in our sample, and the effect in the cartesian coordinates is not greater than the uncertainties derived here as well. Qualitatively, our results are not affected by the choice of ignoring the zero-point offset.

The conversion has been performed using the same procedure described in Marchetti, Rossi & Brown (2018). In short, Markov Chain Monte Carlo (MCMC) has been used for sampling the likelihood function in stars with low relative parallax error ($\sigma_\varpi/\varpi < 0.2$). For stars with large relative error in parallax, MCMC has been used to perform a Bayesian analysis, adopting the exponentially decreasing prior explored by Astraatmadja & Bailer-Jones (2016). In the cases of objects with low relative error, a Bayesian analysis would have its posterior dominated by the likelihood function, thus we choose the simpler approach of maximum likelihood in these cases. We employed the Python package *emcee*

(Foreman-Mackey et al., 2013) to run the MCMC algorithm.

For the group of stars with low relative parallax error, as stated above, emcee sampled the likelihood function:

$$\mathcal{L}(\mathbf{x}) \propto \exp[-0.5(\mathbf{x}-\boldsymbol{\mu})^T\Sigma^{-1}(\mathbf{x}-\boldsymbol{\mu})], \tag{2.57}$$

which is a multivariate normal distribution giving the probability of the state $\mathbf{x}$. The vector $\boldsymbol{\mu}$ corresponds to the set of four Gaia DR2 observables $(\mu_\alpha^*, \mu_\delta, \varpi, v_r)^T$, respectively: proper motion in right ascension and declination, radial velocity and parallax. Σ is the covariance matrix:

$$\Sigma = \begin{pmatrix} \sigma^2_{\mu_\alpha^*} & \sigma_{\mu_\alpha^*}\sigma_{\mu_\delta}\rho(\mu_\alpha^*, \mu_\delta) & \sigma_{\mu_\alpha^*}\sigma_\varpi\rho(\mu_\alpha^*, \varpi) & 0 \\ \sigma_{\mu_\alpha^*}\sigma_{\mu_\delta}\rho(\mu_\alpha^*, \mu_\delta) & \sigma^2_{\mu_\delta} & \sigma_{\mu_\delta}\sigma_\varpi\rho(\mu_\delta, \varpi) & 0 \\ \sigma_{\mu_\alpha^*}\sigma_\varpi\rho(\mu_\alpha^*, \varpi) & \sigma_{\mu_\delta}\sigma_\varpi\rho(\mu_\delta, \varpi) & \sigma^2_\varpi & 0 \\ 0 & 0 & 0 & \sigma^2_{v_r} \end{pmatrix}. \tag{2.58}$$

The non-zero off-diagonal elements appear because Gaia measurements in parallax and proper motion are correlated (Lindegren et al., 2018). All values needed for the matrix elements – square roots of the variances and correlation coefficients – are given in the data release. Fig. 14 shows an example of diganostic plot for one of the objects whose likelihood function was sampled. MCMC sampling began with a set of 100 walkers initialized randomly in a narrow region of the phase space around $\boldsymbol{\mu}$. The walkers made 10^4 steps, with the burn-in parameter set to the 200th step after some tests. Then, all $\mathbf{x}$ states after the burn-in were saved in an ASCII file to be converted – one-by-one – to cartesian coordinates in the Galactocentric rest frame.

One should note that Gaia DR2 astrometric solution – and cartesian state vectors as well – have six dimensions, and both right ascension α and declination δ were not included in $\boldsymbol{\mu}$. These two observables are treated as parameters, and the justification is that their uncertainties, of the order of 10^{-2} mas, are negligible in comparison with the full circle $(\sigma_\alpha, \sigma_\delta \ll 2\pi)$, and the errors in cartesian coordinates are dominated by the errors in proper motion and, mainly, parallax. To better understand the justification, let's imagine a star at the origin of a spherical coordinate system, but located at 1 kpc from the observer. An error of 0.1 mas ($\approx 5 \times 10^{-7}$ radians) in one angular coordinate θ would yield a $\Delta s = r\Delta\theta \approx 5 \times 10^{-4}$pc $\approx$ 100AU. A similar error of 0.1 mas in the parallax would result in a radial uncertainty of $\sim$ 100 pc[17], several orders of magnitude greater than the angular uncertainty. That is, for stars whose positional cartesian components are non-zero, the uncertainty due to the parallax will always be much greater than the uncertainty due to the error in celestial coordinates.

---

[17] Let's ignore, in this example, the fact that the uncertainties in parallax are not symmetric for the sake of simplicity.

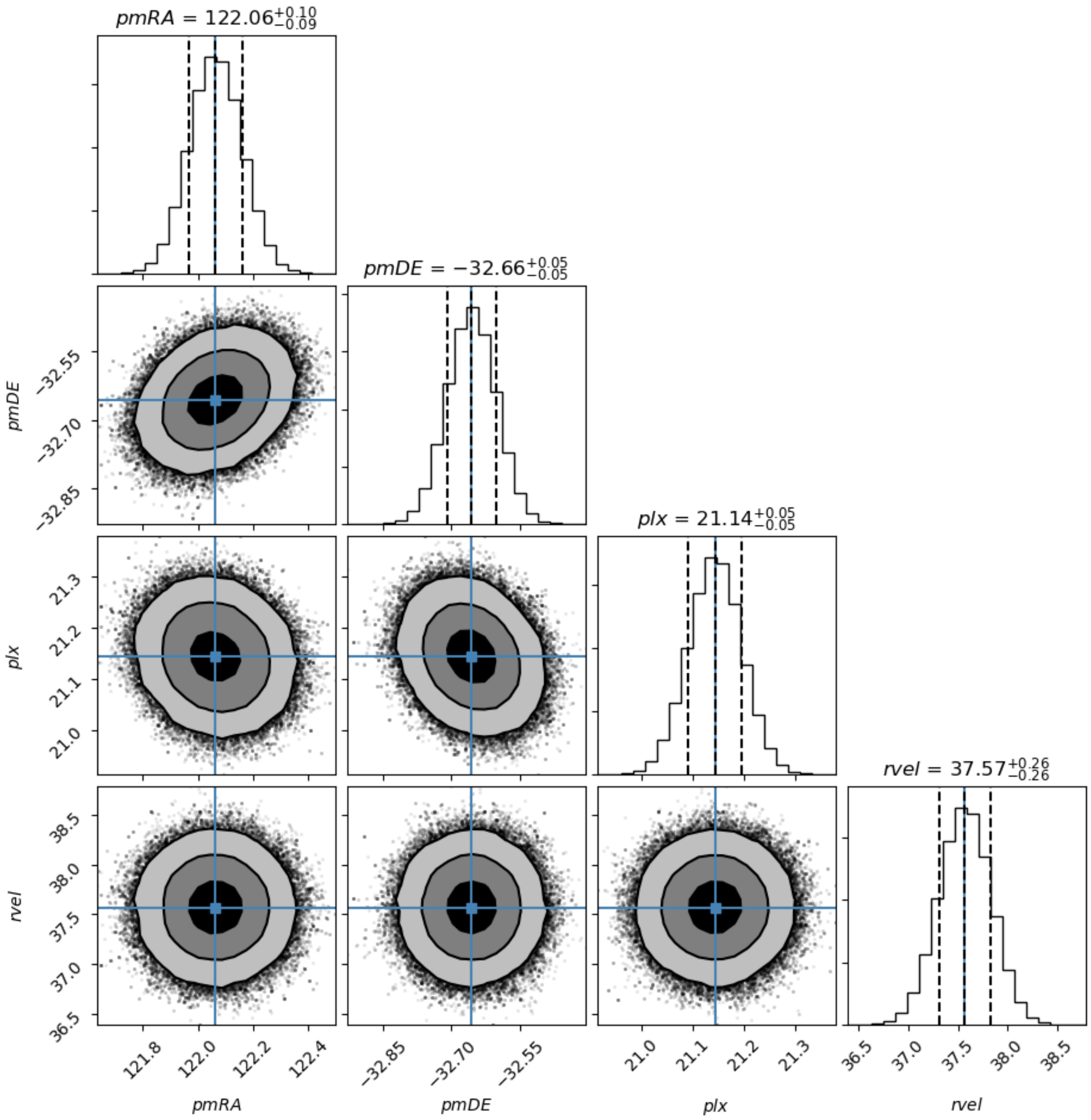

Figure 14 – MCMC sampling of the likelihood function of one of the Hyades dwarfs – HIP 19082. Dashed vertical lines in the histograms represent 16-, 50- and 84-percentiles. The blue lines indicate the value given by Gaia DR2 for each observable. Proper motion units are given in mas yr^{-1}; parallax units in mas; radial velocities in km s^{-1}. The contours are for 1-, 2- and 3-σ. Each point is a random walker state. The correlation between the proper motion components is noticeable. The *corner.py* library (Foreman-Mackey, 2016) was employed to generate the figure.

Treating right ascension and declination as parameters is useful as it simplifies coordinate transform. The transformation from sampled coordinates to cartesian Galactocentric has been performed under the prescriptions from ESA (1997). The six-dimensional vector $\mathbf{a} = (0, 0, \boldsymbol{\mu})^T$ with the input quantities is transformed into the vector

$\mathbf{c} = (X, Y, Z, U, V, W)^T$ containing the cartesian Galactic coordinates by:

$$\mathbf{c} = G\mathbf{a} + \mathbf{s}, \tag{2.59}$$

where $\mathbf{s}$ is the state vector of the Sun w.r.t. the Galactocentric rest frame: $\mathbf{s}$ = (X = -8200 pc, Y = 0 pc, Z = 25 pc, U = 14 km s^{-1}, V = 250.24 km s^{-1}, W = 7.25 km s^{-1})^T, the same values adopted by Marchetti, Rossi & Brown (2018). G is a 6x6 matrix that may be represented by:

$$G = \begin{pmatrix} B & 0 \\ 0 & B \end{pmatrix}, \tag{2.60}$$

and B is a 3x3 matrix resulting from the product of other two matrices, $B = A_G R$, where:

$$A_G = \begin{pmatrix} -0.054875560416215 & -0.873437090234885 & -0.483835015548713 \\ 0.494109427875584 & -0.444829629960011 & 0.746982244497219 \\ -0.867666149019005 & -0.198076373431202 & 0.455983776175067 \end{pmatrix}, \tag{2.61}$$

and:

$$R = \begin{pmatrix} -\sin\alpha & -\cos\alpha\sin\delta & \cos\alpha\cos\delta \\ \cos\alpha & -\sin\alpha\sin\delta & \sin\alpha\cos\delta \\ 0 & \cos\delta & \sin\delta \end{pmatrix}. \tag{2.62}$$

A_G rotates the equatorial coordinates into the Galactic frame and its elements result from the definition of Galactic coordinates (van Altena, 2013). R is the coordinate matrix, defined, e.g., in Johnson & Soderblom (1987).

As previously stated, the states from the markov chain were converted one-by-one into Galactocentric cartesian coordinates, generating an array for each cartesian coordinate. The adopted values for positions (X, Y, Z) and velocities (U, V, W) are the respective medians of the arrays, while the uncertainties are their 16- and 84-percentiles. Fig. 15 shows an example of the likelihood sampling converted to Galactocentric cartesian coordinates using this method.

For stars with high relative parallax error – actually, only outer 16 and HE 0002+0053 – a full Bayesian analysis was performed using a prior for distance:

$$P_r(r) = \frac{r^2}{2L^3} e^{-\frac{r}{L}}, \tag{2.63}$$

which is valid for $r > 0$, being zero otherwise, and L is a scale factor fixed as 2.6 kpc, because Marchetti, Rossi & Brown (2018) argue that this value minimizes the bias of the

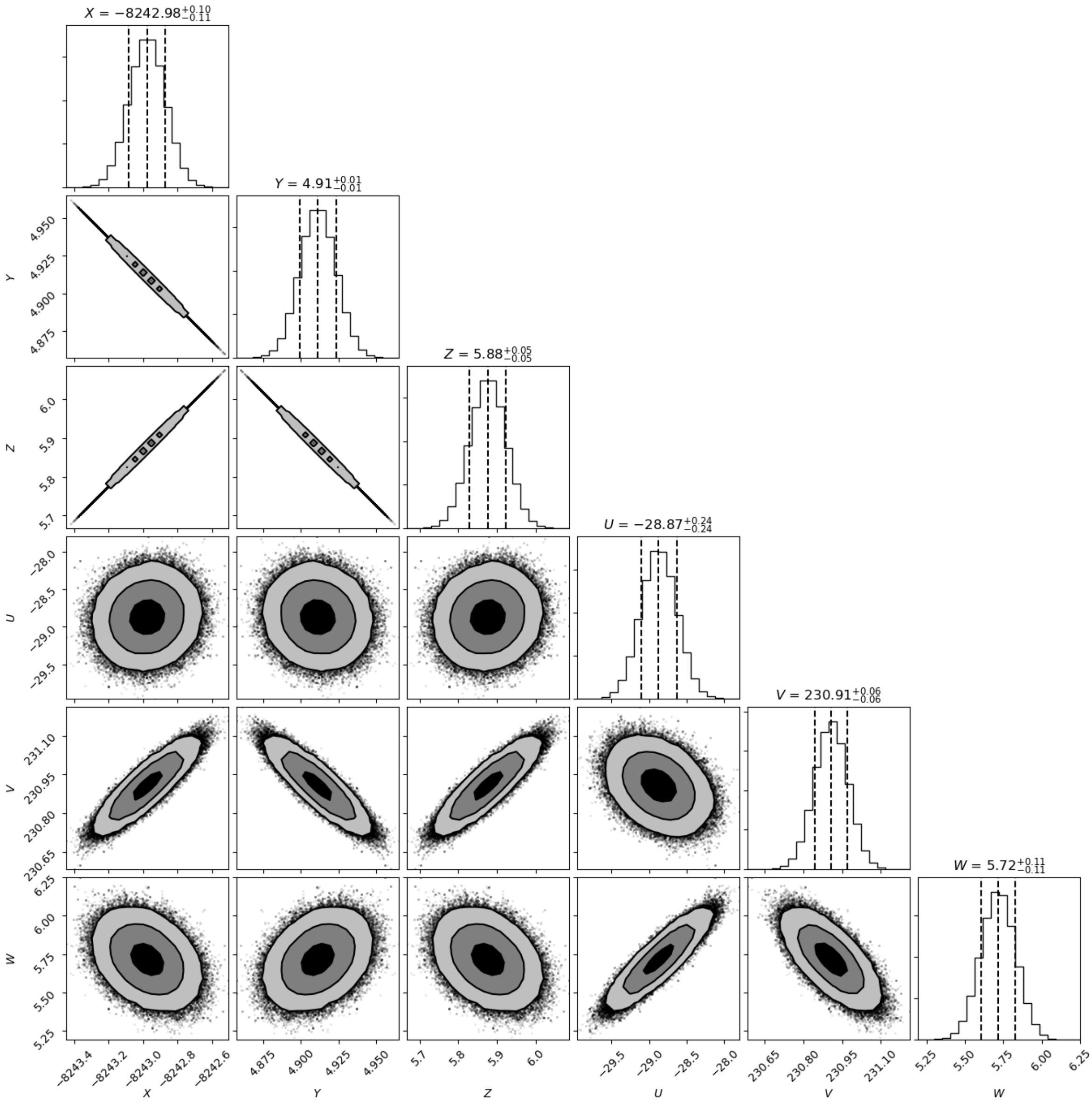

Figure 15 – MCMC sampling of the likelihood function after conversion to Galactocentric cartesian coordinates. Symbols are described in Fig. 14. Positions are given in parsecs, velocities in km s^{-1}.

estimator. The likelihood function is defined in a similar manner as in Eq. 2.57. The main practical difference is that the markov chain now samples distance r directly. Coordinate conversion is made as described above, taking into account that distance has been sampled instead of parallax. The values we have found for positions and velocities agree with those found by Marchetti, Rossi & Brown (2018), what is expected, because the only differences between both analysis were in the parameters of the markov chains – our configuration has more walkers mapping the phase space through a greater number of steps.

2.4.2 Spectral synthesis

The abundance analysis uses the traditional spectroscopic method. Assuming local thermodynamic equilibrium, we adopted 1D plane-parallel Kurucz model atmospheres (Castelli; Gratton; Kurucz, 1997), along with a line list with atomic and molecular parameters and a guess for [X/Fe], where X is the element whose abundance is being measured, as input for the 2017 version of MOOG[18] (Sneden, 1973) in order to produce a synthetic spectrum of the absorption lines of interest. The value of [X/Fe] that produces the best fit between synthetic and observed spectra represents the derived abundance for element X. The spectral synthesis is the adopted method because it is appropriate to spectral regions with strong blends such as the IR spectral regions under consideration in this work. Direct measurement of equivalent widths works best with unblended lines, and is a poor choice for lines with hyperfine splitting and blends, e.g., one cannot separate the equivalent widths of two lines from two different species with the same wavelength.

In the case of F, the measured line is the 23358 Å 1-0 R9 line, as discussed in Ch. 1, and, in stars where this line is not sufficiently strong upper limits of abundance were derived for this chemical element. The upper limit is defined as the F abundance whose synthetic spectrum matches a line depth inversely proportional to the signal-to-noise ratio, i.e., the minimum abundance at which the line begins to emerge from the continuum noise.

The input parameters for the model atmospheres, whose importance was discussed in Sect. 2.1 – effective temperature, surface gravity, metallicity, microturbulence – could not be determined by excitation and ionization equilibrium using our observed spectra in the IR. The method of excitation and ionization equilibrium is standard in spectroscopic analysis to determine the atmospheric parameters. In short, it constitutes in performing equivalent width measurements of a great number of Fe I and Fe II lines to derive abundances in a line-by-line basis – usually through the curve of growth method, used by MOOG. Lines with different excitation potentials have different sensitivities to temperature, and, in FGK stars, Fe II lines are more pressure sensitive than Fe I lines. Therefore, one can derive the effective temperature by eliminating any dependence of line abundance with excitation potential, and surface gravity may be estimated equalizing Fe I and Fe II abundances. Metallicity and microturbulence are calculated analogously. This method is employed in, e.g., Puls et al. (2018), and in several references whose atmospheric parameters we adopted for the stars in this work.

The reason for rely on published atmospheric parameters instead of deriving them directly in our spectra is the lack of reliable Fe II lines at the observed wavelength intervals. All but one Fe II lines from the infrared Fe line list built by Andreasen et al. (2016) are located in the gaps between the echelle orders of the observed spectra. Unfortunately, the

---

[18] MOOG is a code written in FORTRAN, employed in chemical abundance analysis based on LTE atmospheric models: <http://www.as.utexas.edu/~chris/moog.html> (acessed on 12.12.2018).

Table 2 – The adopted atmospheric parameters. Stars are ordered by effective temperature. References: A Bensby et al. (2011); B Kennedy et al. (2011); C Jorissen et al. (2016); D Aleo, Sobotka & Ramírez (2017); E Luck & Heiter (2007); F Goswami et al. (2006); G Liu, Liang & Deng (2009); H Pancino et al. (2010); I Allen & Barbuy (2006); J Goswami, Aoki & Karinkuzhi (2016); K Ito et al. (2009); L see text.

ID	$T_{\rm eff}$	log g	[Fe/H]	v_t	Ref.
outer 16	4050	1.00	-0.45	1.68	A
HIP 19082	4060	4.57	0.00	0.00	L
outer 1	4100	1.20	-0.48	1.64	A
outer 3	4100	1.15	-0.40	1.48	A
outer 2	4200	1.50	-0.56	1.46	A
outer 17	4200	1.45	-0.49	1.73	A
outer 18	4200	1.40	-0.32	1.55	A
outer 20	4200	1.50	-0.58	1.33	A
HE 0002+0053	4225	0.27	-2.18	2.00	B
HE 0017+0055	4250	1.00	-2.40	2.00	C
outer 19	4250	1.50	-0.21	1.64	A
HIP 17766	4268	4.71	-0.10	0.00	D
HIP 19316	4301	4.71	-0.09	0.00	D
HIP 21138	4330	4.69	-0.01	0.00	D
HIP 21256	4334	4.60	0.00	0.00	L
HR 8878	4435	1.98	-0.60	1.68	E
HD 5223	4500	1.00	-2.11	2.00	F
HD 210946	4577	2.42	-0.22	1.60	G
M67-0141	4650	2.80	0.06	1.30	H
μ Leo	4660	2.56	0.26	2.09	E
HD 5424	4700	1.80	-0.51	1.10	I
M67-0223	4800	2.80	0.04	1.30	H
HD 27271	4830	2.30	0.17	1.30	I
HE 0310+0059	4861	1.69	-1.32	2.00	B
HD 26	5000	1.60	-1.13	2.07	J
HD 224959	5050	2.10	-2.44	2.00	J
BD 44	5510	3.70	-3.73	1.30	K

spectra had been collected before any IR Fe line list useful for the method of ionization and excitation equilibrum has been published, thus preventing the possibility of optimizing the spectral coverage for Fe lines during the pre-observing procedures. For most sample stars, as mentioned above, the atmospheric parameters were compiled from high-resolution spectroscopic studies in optical wavelengths available in the literature (see Table 2 for references). For two Hyades stars – HIP 19082 and HIP 21256 – we adopted the temperatures from Gaia DR2 (Andrae et al., 2018). The respective surface gravities were derived from their Gaia DR2 parallaxes. First, to infer the absolute magnitude, with $A_V = 0.155$ and the parallax in miliarcseconds:

$$M_V = V - A_V + 5\log\varpi - 10. \tag{2.64}$$

Then, for the estimation of luminosity, we adopted the eq. (9) from Torres (2010), the T$_{\rm eff}$-BC$_V$ relation from the same paper, V$_\odot$ = -26.732, M$_{bol,\odot}$ = 4.76 and BC$_{V,\odot}$ = -0.08.

Finally, using the well known relation:

$$\log\frac{g_*}{g_\odot} = \log\frac{M_*}{M_\odot} + 4\log\frac{T_{\rm eff,*}}{T_{\rm eff,\odot}} - \log\frac{L_*}{L_\odot}, \tag{2.65}$$

their surface gravities were found, assuming a mass of 0.6 M$_\odot$ for both objects from their spectral types. The metallicity of these stars was inferred by comparison with the spectra from other Hyades stars from our sample, since all of them share the same spectral type. Finally, we assumed for these two objects the same microturbulence published for the remaining stars of the same cluster.

Our master line list uses atomic and molecular parameters (excitation potential, log gf, dissociation energy) from the APOGEE line list (Shetrone et al., 2015) for selected H-band lines, in most cases. The atomic parameters of Ce II lines are from Cunha et al. (2017). For the K-band we have compiled a master list from various sources in the literature: Brooke et al. (2014) for CN lines, Alves-Brito et al. (2011) for the CO and Na features at the 23300:23400 Å region and Ryde et al. (2016) for Si, Ca and the 22632 Å Ti line. For the remaining K-band molecular lines (CO and HF) the values from the HITRAN database (Gordon et al., 2017) have been adopted. The NIST database (Kramida et al., 2018) has been used for excitation potential and oscilator strengths of the 23328 Å Mg and 22444 Å Ti lines and for the excitation potentials of the Sc lines. For the later, log gf values were determined using an IR atlas of Arcturus (Hinkle; Wallace; Livingston, 1995): we have built a synthetic spectrum of these Sc features, freezing the abundance of Sc to the value published in Ramírez & Allende Prieto (2011) while tweaking the log gf of these lines until a good match between synthetic and observed spectra was found – i.e., we calculated an astrophysical log gf.

Whenever possible, lines in both bands were measured for each element. A total of 90 spectral regions were evaluated separately, all of them previously tested in our spectrum of μ Leo and in the Arcturus atlas, using reference atmospheric parameters and abundance ratios of Smith et al. (2013) and Ramírez & Allende Prieto (2011), respectively. The CNO elements, dependent on molecular features (OH, CO, CN), were measured in the order O, C, N. The C I atomic line at 16890 Å was employed to confirm C abundances measured from CO when possible. The full master line list with atomic parameters is shown in

Table 4. Notice that it has more than 90 lines: this happens because in some regions two or more lines of the same element are strongly blended, and were considered as only one line for practical effects in the analysis (as can be seen in the line-by-line measurements shown in Appendix A.1). One may notice the presence of a ^{13}CO line: this feature is included in the list to probe the ^{12}C/^{13}C ratio by tweaking its value in MOOG parameters after determination of C abundance.

Table 3 – Sensitivities in the abundances due to the uncertainties in the atmospheric models for representative stars. The *Quad.* columns give the total internal uncertainties.

	outer18					HIP 17766				
	$\Delta T_{\rm eff}$	$\Delta\log g$	Δ[Fe/H]	Δv_t	Quad.	$\Delta T_{\rm eff}$	$\Delta\log g$	Δ[Fe/H]	Δv_t	Quad.
ΔA(C)	0.04	0.13	-0.11	-0.09	0.20	0.02	0.00	-0.12	-0.00	0.12
ΔA(N)	0.00	0.01	-0.05	0.02	0.05	0.09	0.11	-0.07	0.10	0.19
ΔA(O)	0.14	-0.04	-0.04	-0.01	0.15	0.03	0.00	-0.02	0.00	0.04
ΔA(F)	**0.17**	**-0.01**	**-0.05**	**-0.02**	**0.18**	**0.06**	**0.03**	**-0.05**	**0.05**	**0.10**
ΔA(Na)	0.08	-0.06	-0.14	-0.09	0.19	...	...	...	...	...
ΔA(Mg)	0.05	-0.04	-0.10	-0.03	0.12	...	...	...	...	...
ΔA(Al)	0.08	-0.02	-0.11	-0.03	0.14	...	...	...	...	...
ΔA(Si)	-0.03	0.05	-0.11	-0.06	0.14	-0.05	0.00	-0.16	0.00	0.17
ΔA(K)	0.01	-0.01	-0.13	-0.02	0.13	0.04	0.02	-0.16	0.02	0.17
ΔA(Ca)	0.04	-0.03	-0.16	-0.04	0.17	0.02	0.00	-0.23	0.00	0.23
ΔA(Sc)	0.14	0.01	-0.15	-0.07	0.22	0.07	-0.01	-0.16	-0.01	0.17
ΔA(Ti)	0.12	0.02	-0.14	-0.08	0.20	0.05	0.01	-0.15	0.01	0.16
ΔA(V)	0.13	0.00	-0.15	0.00	0.20	...	...	...	...	...
ΔA(Cr)	0.02	0.02	-0.14	-0.01	0.14	0.00	0.02	-0.17	0.01	0.17
ΔA(Mn)	0.00	0.02	-0.15	-0.04	0.15	0.00	0.04	-0.13	0.03	0.14
ΔA(Co)	0.03	0.06	-0.11	-0.01	0.13	-0.02	-0.02	-0.17	-0.02	0.17
ΔA(Ni)	-0.01	0.07	-0.12	-0.00	0.14	-0.03	0.00	-0.21	0.01	0.21
ΔA(Ce)	0.06	0.08	-0.16	0.00	0.19	...	...	...	...	...

For the spectral synthesis itself, a Python script has been written to optimize the usage of MOOG. The user starts calling the script on command line using arguments with information such as spectral interval, element of interest, instrumental profile (the Gaussian FWHM from MOOG parameter file) and eventual geometric offsets $\Delta\lambda$ and Δy in case of mismatch of wavelength scale and/or continuum level between observed and synthetic spectra. An advantage of using command line arguments is the possibility of further optimization if the user knows their input values beforehand, allowing the use of a higher-level script to acelerate the workflow. The script makes use of the object-oriented programming paradigm to allow the interaction of the user with the process – parameters may be changed in runtime and the user is allowed to constrain the interval to be considered in spectral fitting. MOOG is called once before the interaction to build a first guess of the synthetic spectrum, then the user interacts with a plot showing both synthetic and observed spectra. After that, the script runs MOOG several times until the best fit is reached. The fitting is evaluated through chi-squared minimization:

$$\chi^2 = \sum_i^N \frac{(o_i - s_i)^2}{s_i}. \tag{2.66}$$

In the above equation, o_i represents the flux of the i-th point of the observed spectrum. The spectral interval under consideration, previously constrained by the user, has N observed points. In its turn, s_i is sampled from an interpolation that the script performs in the synthetic spectrum contained in MOOG output files. This is needed to avoid a mismatch in the corresponding wavelengths of o_i and s_i. The best fit is the one with the lower χ^2 value, and the chemical abundance used as input for its synthesis is taken as the estimated abundance for the considered spectral line. The script allows the user to check if the result is acceptable. Also, it has a function that allows the automatic adjustment of the instrumental profile if needed, to account for the additional broadening introduced by uncorrected shear, as discussed in Sect. 2.3. In uncrowded spectral regions, the automated fitting process takes, typically, less than one second.

The abundance uncertainties were estimated as in Alves-Brito et al. (2010): four new atmospheric models were built varying the atmospheric parameters by their uncertainties, one at a time. A new spectral synthesis was performed for each new model to estimate the sensitivity of the chemical abundances to the increase of the value of the respective atmospheric parameter. The sensitivities were added by quadrature to quantify the total uncertainty due to the atmospheric model. Table 3 shows two representative stars, – a giant and a dwarf. The adopted uncertainties of the atmospheric parameters are those published in their references (Bensby et al. (2011); Aleo, Sobotka & Ramírez (2017)): (ΔT$_{\rm eff}$, Δlog g, Δ[Fe/H], Δv$_t$) = (75 K, 0.3 dex, 0.14 dex, 0.2 km/s) for outer 18 and (ΔT$_{\rm eff}$, Δlog g, Δ[Fe/H], Δv$_t$) = (60 K, 0.015 dex, 0.19 dex, 0.2 km/s) for HIP 17766.

Table 4 – The master line list with atomic parameters. See text for references.

Wavelength (Å)	Species	χ (eV)	log gf (dex)
15130.9	OH	0.170	-5.499
15278.5	OH	0.205	-5.382
15281.1	OH	0.205	-5.382
15505.7	OH	0.515	-5.305
15568.8	OH	0.299	-5.269
15572.1	OH	0.300	-5.269
15719.7	OH	0.358	-5.254

Continued on next page

Table 4 – continued

Wavelength	Species	χ	log gf
15755.5	OH	0.571	-5.107
15756.5	OH	0.572	-5.107
16190.1	OH	0.688	-4.893
16448.1	OH	0.612	-5.075
16450.4	OH	0.608	-5.048
16909.3	OH	0.898	-4.654
15784.0	CO	hfs	···
16159.0	CO	hfs	···
16831.0	CO	hfs	···
16890.4	C I	9.002	0.503
23106.1	CO	0.110	-5.664
23109.4	CO	1.513	-4.906
23118.2	CO	0.100	-5.687
23122.1	CO	1.550	-4.898
23130.8	CO	0.090	-5.711
23310.9	CO	2.025	-4.802
23329.7	CO	2.067	-4.795
23351.4	CO	0.419	-5.084
23351.6	CO	1.586	-4.473
23362.0	CO	0.407	-5.104
23362.6	CO	1.621	-4.464
23367.7	CO	0.005	-6.338
24014.7	^{13}CO	0.307	-5.098
15260.0	CN	hfs	···
15410.0	CN	hfs	···
15447.0	CN	hfs	···
15466.0	CN	hfs	···
15472.0	CN	hfs	···
15482.0	CN	hfs	···
15522.0	CN	hfs	···
15563.0	CN	hfs	···
21805.6	CN	1.005	-2.162
21810.4	CN	0.990	-2.168
21825.6	CN	1.230	-1.876
21847.3	CN	0.997	-2.291
21870.2	CN	1.020	-2.148

Continued on next page

Table 4 – continued

Wavelength	Species	χ	log gf
21947.8	CN	1.281	-1.871
22032.0	CN	1.308	-1.864
22074.8	CN	1.069	-2.112
23358.3	HF	0.227	-3.955
22056.4	Na I	3.191	0.287
23379.0	Na I	3.754	-0.420
23379.1	Na I	3.754	0.530
15740.7	Mg I	5.931	-0.312
15748.9	Mg I	5.932	-0.438
15749.0	Mg I	5.932	0.080
15765.6	Mg I	5.933	-1.794
15765.7	Mg I	5.933	-0.437
15765.8	Mg I	5.933	0.471
15879.5	Mg I	5.946	-2.438
15879.6	Mg I	5.946	-1.366
15879.6	Mg I	5.946	-3.615
15886.2	Mg I	5.946	-1.702
15886.3	Mg I	5.946	-2.301
23328.1	Mg I	6.719	-1.493
16763.4	Al I	4.087	-0.505
15557.8	Si I	5.964	-0.820
16060.0	Si I	5.954	-0.607
16094.8	Si I	5.964	-0.258
16828.2	Si I	5.984	-1.172
21819.7	Si I	6.720	0.087
21879.3	Si I	6.720	0.384
22537.6	Si I	6.620	-0.216
15163.1	K I	2.670	0.697
15163.1	K I	2.670	-1.280
15168.4	K I	2.670	0.521
15772.4	K I	3.397	-2.510
15772.7	K I	3.397	-2.510
16136.8	Ca I	4.531	-0.551
16150.8	Ca I	4.532	-0.198
16155.2	Ca I	4.532	-0.543
16157.4	Ca I	4.554	-0.152

Continued on next page

Table 4 – continued

Wavelength	Species	χ	log gf
22626.8	Ca I	4.680	-0.281
22052.1	Sc I	1.448	-0.340
22065.4	Sc I	1.439	-0.970
15543.8	Ti I	1.879	-1.160
15602.8	Ti I	2.267	-1.639
22444.9	Ti I	1.739	-2.370
22632.7	Ti I	1.880	-2.760
15567.7	V I	4.623	-3.967
15567.7	V I	4.586	-3.806
15924.0	V I	hfs	$\cdots$
15860.2	Cr I	4.697	-0.017
15159.0	Mn I	hfs	$\cdots$
15217.0	Mn I	hfs	$\cdots$
15262.0	Mn I	hfs	$\cdots$
16757.0	Co I	hfs	$\cdots$
15555.1	Ni I	5.279	-0.903
15555.2	Ni I	5.279	-0.608
15555.4	Ni I	5.488	0.036
15605.7	Ni I	5.299	-0.527
15605.8	Ni I	5.299	-0.839
16584.0	Ni I	hfs	$\cdots$
16589.3	Ni I	5.469	-0.591
16815.5	Ni I	5.305	-0.496
16818.8	Ni I	6.039	0.442
16945.3	Ni I	5.363	-0.741
16996.3	Ni I	5.299	0.302
15277.7	Ce II	0.609	-1.940
15784.8	Ce II	0.318	-1.540
15829.8	Ce II	0.320	-1.800
16595.2	Ce II	0.122	-2.190

3 Results and discussion

Here we present the results divided in three sections: the *outer disc* section, concerning red giants already studied with optical spectra by Bensby et al. (2011); the *open clusters* section, where our findings are discussed for K-dwarfs from the Hyades and the red giants from M 67. Finally, the results for the *peculiar* objects (CEMP, CH- and Ba- stars) are discussed. But, first, let's take a look at the results for the reference stars, Arcturus and μ Leo, shown in Table 5.

Table 5 – Abundance ratios, in dex, derived for Arcturus and μ Leo. The values for [Fe/H] are those adopted in the atmospheric models. For comparison, we show the results from Ramírez & Allende Prieto (2011) (R11) and Smith et al. (2013) (S13).

[X/Y]	Arcturus (this work)	Arcturus (R11)	μ Leo (this work)	μ Leo (S13)
[Fe/H]	-0.52	-0.52	0.26	0.26
[C/Fe]	0.10	0.43	-0.11	-0.20
[N/Fe]	0.06	···	0.57	0.62
[O/Fe]	0.33	0.50	0.10	0.10
[F/Fe]	-0.16	···	···	···
[Na/Fe]	0.17	0.11	···	···
[Mg/Fe]	0.34	0.37	···	-0.01
[Al/Fe]	0.28	0.34	0.11	0.19
[Si/Fe]	0.36	0.33	0.09	-0.01
[K/Fe]	0.20	0.20	0.05	0.34
[Ca/Fe]	0.14	0.11	-0.09	0.02
[Sc/Fe]	0.15	0.15	···	···
[Ti/Fe]	0.27	0.27	0.11	0.19
[V/Fe]	0.12	0.20	···	-0.01
[Cr/Fe]	0.03	-0.05	···	0.24
[Mn/Fe]	-0.07	-0.21	0.40	0.10
[Co/Fe]	0.09	0.09	-0.02	-0.02
[Ni/Fe]	0.04	0.06	0.20	0.12
[Ce/Fe]	-0.25	···	-0.35	···

The abundance ratios derived here for Arcturus – using the R $\sim$ 100000 spectrum from the Hinkle, Wallace & Livingston (1995) atlas – agree reasonably well with those calculated with optical spectrum by Ramírez & Allende Prieto (2011), from whom we adopted the atmospheric parameters. Only for three elements the results differ by more than 0.1 dex – C, O and Mn, while they did not present abundances for N, F and Ce. However, the abundance of C derived here is in fair agreement with those found by Smith et al. (2013), in whose work the APOGEE line list was tested in some well studied giants.

Our values for O disagree by $\sim$ 0.15 dex with both works, while the Mn abundance derived here agrees with the value found by Smith et al.. The difference found for O does not represent necessarily a flaw, because results closer to ours are also found in the (extensive) literature for this object (e.g., Alves-Brito et al. (2010)). The 24014.7 Å ^{13}CO line is the only clean feature of this CO isotopologue that we have found in the available spectral interval for most stars of our sample. However, it gave a ^{12}C/^{13}C ratio (and uncertainties) too high for what is commonly reported for Arcturus – we measured a ratio of 15 ± 8 while the ratio of $\sim$ 7 is usual in the literature (e.g., Smith et al. (2013) reported 6.3 ± 0.6). Since our values come from only one line and we are not sure about blends of this feature with ^{12}C-bearing species, we will not consider the ^{12}C/^{13}C ratio in the discussion.

The main purpose of the analysis of Arcturus is the validation of the line list. As stated above, in general our results show agreement with those found in the literature. For species with most spectral regions evaluated – OH, C+CO, CN, Si and Ni – we applied the Shapiro-Wilk normality test (Shapiro; Wilk, 1965) in the results for Arcturus to estimate if the dispersion of line-by-line abundances follows a normal distribution for each of these species. The null-hypothesis was positive for all species evaluated, i.e., their scatter may be considered normal, except for Si. A 21874 Å Si line – the cause of the deviation – was removed from the line list. The Ce abundance from this work is 0.13 dex below the optical value adopted by Cunha et al. (2017) to define the oscillator strenghts employed here. It is possible that blending played a role in this difference, because the spectral regions of IR Ce II lines are filled with features from CNO-bearing molecules, but we did not isolate the causes. The F abundance derived here for Arcturus (A(F) = 3.72) differs by only 0.06 dex from the quantity found by Abia et al. (2015) using three HF lines with the updated excitation potentials.

For μ Leo, a comparison with Smith et al. (2013) shows agreement in the 0.1 level for most species, even taking into account the lower resolution of the spectrum in comparison with the Arcturus atlas and that the uncertainties for giants such as μ Leo are in the 0.1-0.2 dex interval (see Table 3). Only K and Mn show disgreement, by $\sim$ 0.3 dex. In comparison with the (spectroscopic) analysis of Luck & Heiter (2007), made in the optical, our abundance ratios are mostly lower, in some cases (Al and Si) by 0.4 dex. Unfortunately, we have no K-band spectra for μ Leo.

3.1 Outer disc

The F abundances in outer disc stars and their relationship with O follow the trend of the solar neighbourhood found in the work of Jönsson et al. (2017) (see Figs. 16 and 17; and Table 6), at least for the two 'O-rich' stars (outer 18 and outer 19). Meanwhile, the two outer disc stars with [O/H] $\sim$ -0.4 (outer 16 and outer 17) seem to deviate from the

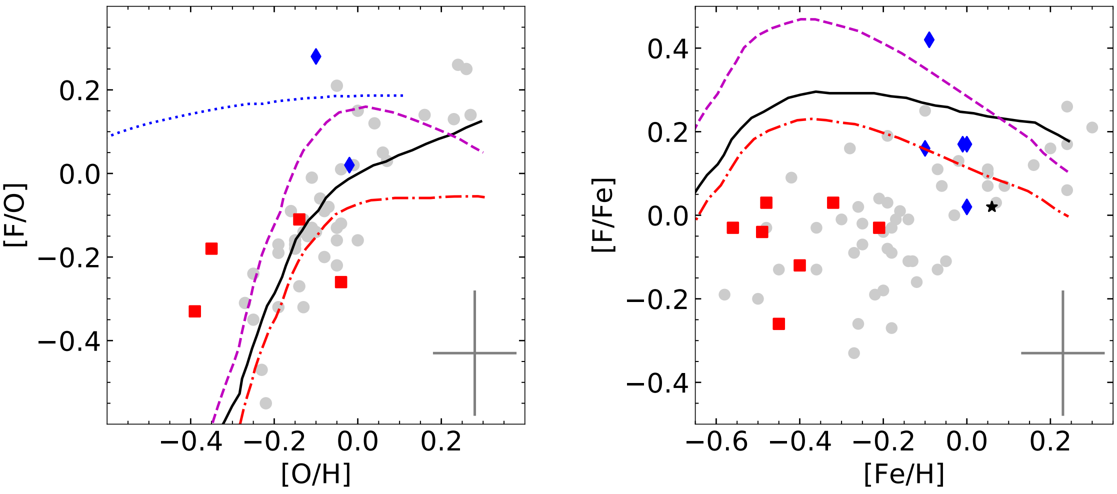

Figure 16 – F abundances for the 'normal' disc stars and models of Galactic chemical evolution. *Red squares*: outer disc giants. *Blue diamonds*: Hyades dwarfs. *Black star*: M67. *Grey circles*: Solar neighbourhood giants from Jönsson et al. (2017). *Red dash-dotted line*, *black solid line* and *magenta dashed line*: one-infall models F7 (standard yields), F8 (WR yields x2) and F9 (AGB yields x2) from Spitoni et al. (2018), respectively. *Blue dotted line*: model from Kobayashi et al. (2011) with ν-process and neutrino luminosity $E_\nu = 3$.

solar neighbourhood trend, being 0.2 dex more F-rich (or more O-poor) than expected from a linear fit. Here we have three possible scenarios:

- The behaviour of the [F/O] ratio in the Galactic disc would change at [O/H] $\sim$ -0.3. At first, this could be reconciled with the inclusion of the ν-process adopting yields lower than those from Kobayashi et al. (2011). This would create a problem with the [F/O] $<$ -0.4 stars from Jönsson et al. (2017) – but one may point out that only two stars of their sample are so F-poor, thus these two objects may be outliers;
- The [F/O] ratio *in the outer disc* would have a less pronounced slope than in the solar neighbourhood for some reason, implying a greater role in F production from Type II Supernovae in this region. That is, the secondary behaviour of F would be less pronounced (but still greater than 1) in the outer disc – a possibility shown in Fig. 17, or;
- These two O-poor stars would be outliers, and the speculation on the first two scenarios would be the effect of having a small data set.

In order to test these scenarios, more data for F are required (1) across the disc in the metal-poor ([O/H] $<$ -0.3) regime, and (2) for the outer disc, particularly in the

Table 6 – Abundance ratios, in dex, derived for the outer disc stars. The values for [Fe/H] are those adopted in the atmospheric models.

[X/Y]	outer 1	outer 2	outer 3	outer16	outer17	outer18	outer 19	outer 20
[Fe/H]	-0.48	-0.56	-0.40	-0.45	-0.49	-0.32	-0.21	-0.58
[C/Fe]	···	···	···	-0.30	-0.11	0.01	-0.18	-0.03
[N/Fe]	···	···	···	0.40	0.12	0.21	0.18	0.08
[O/Fe]	···	···	···	0.07	0.14	0.29	0.08	0.34
[F/Fe]	**0.03**	**-0.03**	**-0.12**	**-0.26**	**-0.04**	**0.03**	**-0.03**	···
[Na/Fe]	0.42	0.48	0.42	0.34	0.58	0.53	0.76	···
[Mg/Fe]	0.03	0.22	0.09	0.13	-0.03	0.21	0.14	0.42
[Al/Fe]	···	···	···	0.20	-0.06	0.25	0.33	···
[Si/Fe]	0.15	0.14	0.39	0.39	0.32	0.26	0.35	0.47
[K/Fe]	···	···	···	0.07	0.16	0.12	0.29	0.27
[Ca/Fe]	0.09	0.37	0.33	-0.14	0.07	0.24	0.05	0.14
[Sc/Fe]	0.01	0.26	0.31	0.09	-0.08	0.25	0.13	···
[Ti/Fe]	0.04	0.40	0.21	0.22	0.12	0.31	0.23	0.50
[V/Fe]	···	···	···	0.01	···	-0.13	···	···
[Cr/Fe]	···	···	···	0.11	0.18	0.10	···	0.25
[Mn/Fe]	···	···	···	0.17	0.08	0.18	0.18	-0.10
[Co/Fe]	···	···	···	-0.13	-0.10	-0.06	-0.16	0.05
[Ni/Fe]	···	···	···	0.06	0.05	0.01	0.00	0.08
[Ce/Fe]	···	···	···	0.13	0.23	0.00	0.23	···

super-solar metallicity regime. More data in the metal-poor interval – maybe using the 12.2 μm line mentioned in Ch. 1 – would finally shed light on the role (or abscence of role) of the ν-process in the cosmic enrichment of F. As stressed by Spitoni et al. (2018) in their conclusions, more data for F at low metallicities ([O/H] $<$ -0.4) are needed to confirm their prediction about the role of Wolf-Rayet stars in the production of F, because they attribute to the WR stars the pronounced slope in the [F/O] plot, unexplained if only AGB stars are considered. Observations of more metal-rich stars from the outer disc would solve at least the third scenario stated above – if they follow the trend of the solar neighbourhood, the behaviour of the O-poor stars shown here would be just an observational effect, and the hypothesis of a combined enrichment by WR+AGB could be strengthened also for the outer disc, if the yields used by Spitoni et al., which consider SNe+AGB+WR stars, are not totally unrealistic. Unfortunately, our [F/O] measurements in the outer disc are limited to only four objects, because the rest of the sample lacks simultaneous H- and K-band observations, and all OH lines are in the H-band, while the HF feature inhabits the K-band.

Regarding the [F/Fe] ratio, no radial gradient is evident. The star with the largest Galactocentric radius – outer 16, 14.5 kpc – is also the most F-poor. Thus, it would be interesting to explore in depth the region around $R_{GC} = 14$ kpc in further observations. Another interesting result shown in the [F/Fe] plot is that the outer disc sample follows the solar neighbourhood trend found by Jönsson et al. (2017). That is, if the outer disc

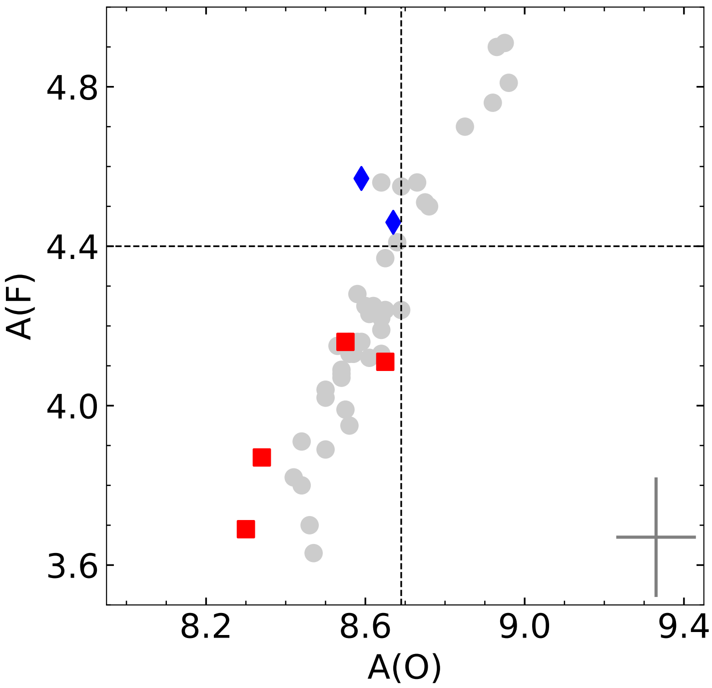

Figure 17 – A(F) vs A(O). The colours of the points are as in Fig. 16. The dashed lines represent solar values.

Table 7 – Positions and velocities of the outer disc stars in the Galactocentric rest frame. The position of the Sun is assumed at (X, Y, Z) = (-8200, 0, 25) pc.

Star	X (pc)	Y (pc)	Z (pc)	U (km/s)	V (km/s)	W (km/s)
outer 1	-11530^{+425}_{-571}	-750^{+96}_{-129}	-1819^{+236}_{-316}	$-30.0^{+1.2}_{-1.6}$	$232.4^{+1.7}_{-2.2}$	$9.4^{+3.6}_{-2.7}$
outer 2	-10545^{+240}_{-301}	-690^{+71}_{-89}	-1360^{+142}_{-178}	$39.0^{+4.8}_{-3.8}$	$145.3^{+10.2}_{-12.8}$	$-9.3^{+1.5}_{-1.8}$
outer 3	-10685^{+305}_{-404}	-972^{+119}_{-158}	-1417^{+177}_{-235}	$50.9^{+3.8}_{-2.9}$	$193.7^{+7.5}_{-9.9}$	$19.5^{+1.0}_{-0.9}$
outer 16	-14243^{+1077}_{-1600}	-2880^{+514}_{-763}	698^{+178}_{-120}	$-27.5^{+1.3}_{-1.0}$	$213.4^{+3.2}_{-4.6}$	$-28.4^{+7.7}_{-11.4}$
outer 17	-12717^{+703}_{-1023}	-2292^{+357}_{-520}	585^{+127}_{-87}	$-22.5^{+2.1}_{-1.5}$	$210.5^{+3.2}_{-4.4}$	$3.4^{+2.2}_{-3.0}$
outer 18	-11668^{+466}_{-630}	-1757^{+236}_{-319}	490^{+84}_{-63}	$13.0^{+1.6}_{-1.2}$	$221.6^{+3.3}_{-4.4}$	$-20.3^{+4.0}_{-5.4}$
outer 19	-11630^{+475}_{-666}	-1964^{+272}_{-381}	731^{+137}_{-98}	$-21.8^{+0.9}_{-0.8}$	$220.3^{+1.4}_{-1.8}$	$10.9^{+1.5}_{-1.9}$
outer 20	-10664^{+251}_{-318}	-1410^{+144}_{-182}	538^{+66}_{-52}	$84.5^{+15.6}_{-12.3}$	$-4.6^{+23.2}_{-29.3}$	$-25.2^{+4.7}_{-5.9}$

stars share their chemical history with the solar neighbourhood, the results shown here add another piece of evidence to the positive slope found by Jönsson et al. in the [F/Fe] vs. [Fe/H] space, indicating that the abundance of F grows with the abundance of Fe, at least for [Fe/H] > -0.6. As previously discussed in Ch. 1, no chemical evolution models published to date reproduce this behaviour.

The outer disc stars have abundances of Mg, Si and Ti measured in optical

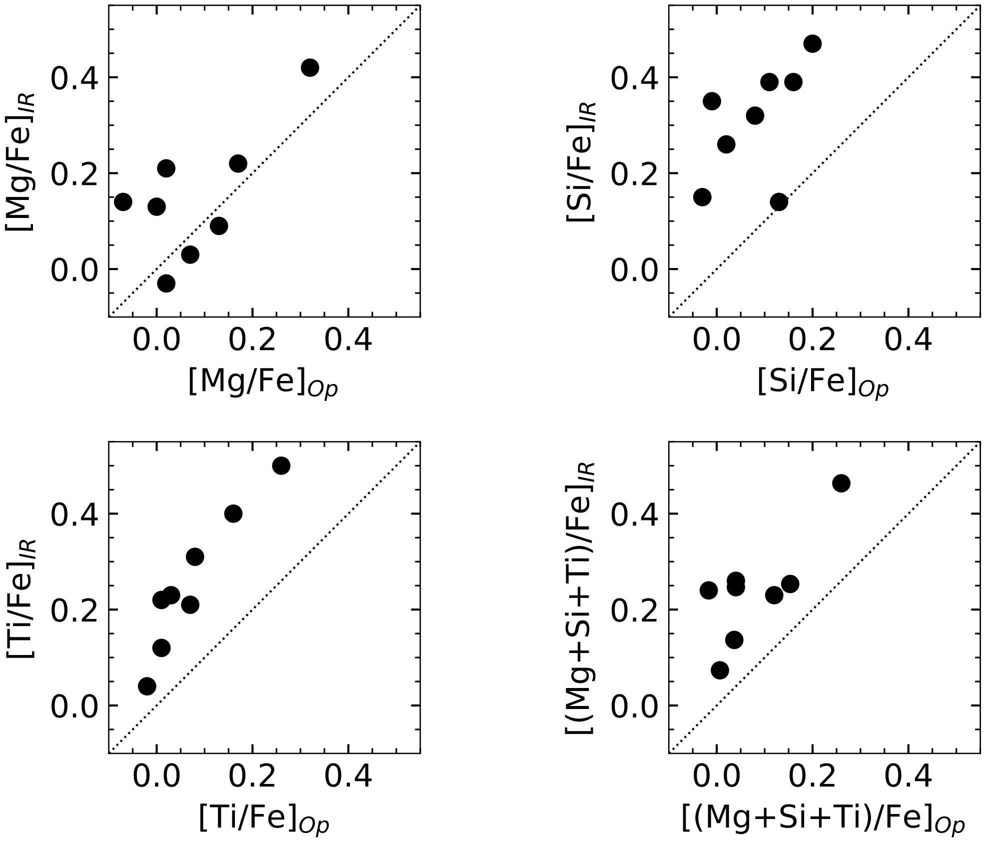

Figure 18 – Comparison between Mg, Si and Ti abundances in the outer giants derived with optical spectra by Bensby et al. (2011) (horizontal axis) and those calculated in this work using infrared spectra (vertical axis).

spectra (Bensby et al., 2011). The abundances from this work differ by 0.2 dex from those measured in the optical for Si and Ti, while the median difference in [Mg/Fe] is lower than 0.1 dex. A comparison is shown in Fig. 18. We note here that the two possible [F/O] outliers – i.e. outer 16 and outer 17 – do not seem to show any anomalous chemical content w.r.t. the remainder of the outer disc sample. These discrepancies in Mg, Si and Ti are unexpected, because they do not happen in the calibration with Arcturus neither with μ Leo (if we consider the comparison with Smith et al. (2013)). Indeed, the effect is inverse to what happened to our μ Leo results if we consider the comparison with the abundances from Luck & Heiter (2007), where the optical abundance ratios are *greater* for the same atmospheric parameters, while for the outer disc sample the abundances in the optical are lower.

In Table 6 all measured abundance ratios of the outer disc stars are shown, and high [Na/Fe] values can be noticed. The combination of Na and O abundances would put these (field) stars in the intermediate population of the Na-O anticorrelation of a

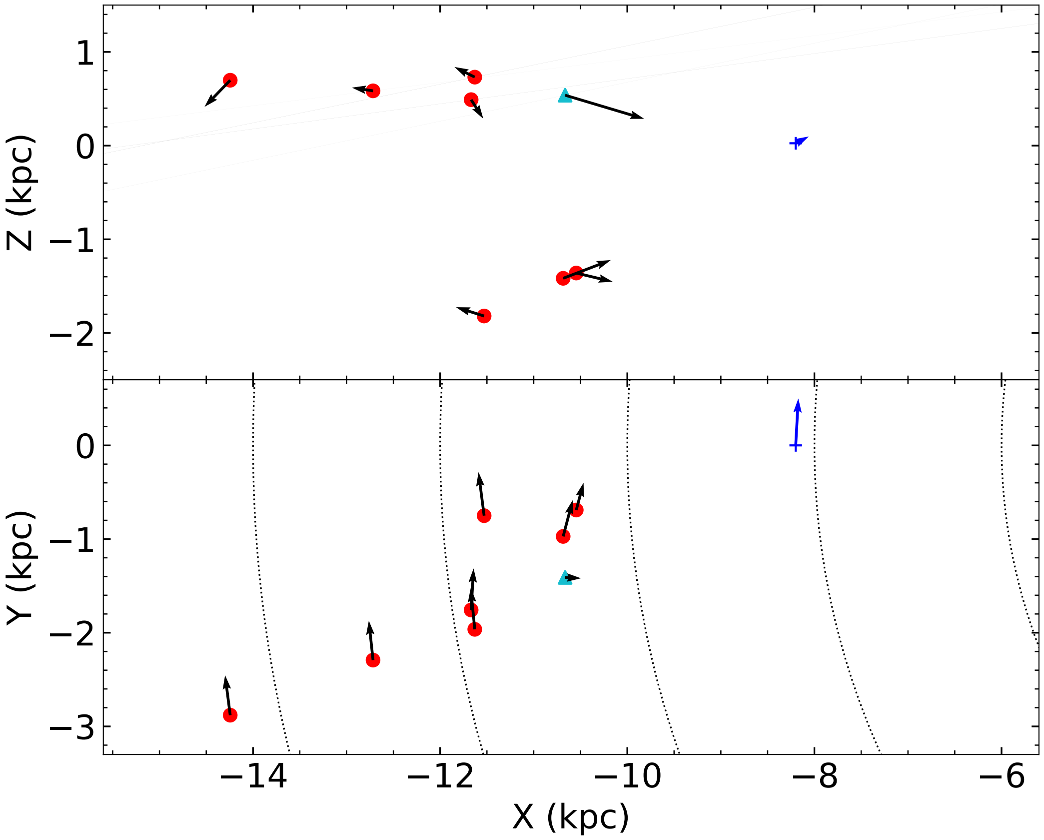

Figure 19 – Locations and velocity vector components of the outer disc sample (red points, black arrows) in Galactocentric coordinates. The blue crosses and arrows represent the Sun and its velocity. Star outer 20 is marked as the cyan triangle. The vectors are downscaled in the XY plot due to the greater value of most of the V components when compared with their respective U and W components.

globular cluster (Carretta et al., 2009). However, the N abundances are not compatible with the self-enrichment pattern found in GC, because the expected [N/Fe] in GC for the Na enhancement derived here is ~ 1 dex (see, e.g., Yong et al. (2008)), far higher than the [N/Fe] ratios shown in Table 6. Also, the kinematics of these Na-enhanced objects are typical from the disc – see Table 7 – thus inconsistent with a GC origin. Measurements in optical spectra would be helpful to confirm (or reject) those high Na abundances. Another element with odd results is Mn, whose abundance ratios are at least 0.2 dex above what has been measured in thin disc stars (Reddy et al., 2003; Feltzing; Fohlman; Bensby, 2007). Mn is one of the few elements where our results for Arcturus differ from those found in the optical by Ramírez & Allende Prieto (2011), while we recall that the IR measurements from Smith et al. (2013) agree with ours. But, since the Mn abundance found for μ Leo is strangely high in comparison with values for the disc found in the literature, the results derived for this element should be taken with a grain of salt.

The star outer 20 has higher abundances of α elements, as can also be seen in Table 6 and in the optical measurements from Bensby et al. (2011). This object was assumed as being from the disc by Bensby et al. using the astrometry available at the time. However, with the improved astrometry delivered by Gaia DR2 the precision of the kinematics has increased, as shown in Fig. 19 and in Table 7. The star outer 20 diverts from the rest of the sample, with its orbit having a considerable inclination with respect to the plane of the disc – 53 degrees if we consider its adopted position and velocity vectors. Also, its specific angular momentum is the lowest among our entire sample in the Galactocentric rest frame, suggesting a highly eccentric orbit. Thus, it is possible that the star has been ejected from the inner region of the Galaxy, or is part of the Galactic halo. Unfortunately, we lack observations in the K-band for this object, therefore no F measurements could be made for outer 20.

3.2 Open clusters

The targets located in open clusters consist of five K-dwarfs from the Hyades and two red giants from M 67. In this section the results are discussed separately. Table 8 shows the derived abundances.

Table 8 – Abundance ratios derived for the open cluster stars – Hyades dwarfs and M67 giants. The values for [Fe/H] are those adopted in the atmospheric models.

[X/Y]	HIP 17766	HIP 21256	HIP 19082	HIP 19316	HIP 21138	M67-0141	M67-0223
[Fe/H]	-0.10	0.00	0.00	-0.09	-0.01	0.06	0.04
[C/Fe]	0.25	0.05	···	···	···	···	···
[N/Fe]	0.06	-0.15	···	···	···	···	···
[O/Fe]	0.14	-0.11	···	···	···	···	···
[F/Fe]	**0.16**	**0.17**	**0.02**	**0.42**	**0.17**	**<0.02**	**<0.02**
[Na/Fe]	···	···	···	···	···	0.35	0.43
[Mg/Fe]	···	···	···	···	···	-0.01	0.00
[Si/Fe]	0.28	0.18	0.33	0.35	0.17	0.28	0.34
[K/Fe]	0.10	-0.05	···	···	···	···	···
[Ca/Fe]	0.23	0.08	0.18	···	···	0.09	0.21
[Sc/Fe]	0.33	0.05	-0.06	···	···	-0.36	-0.05
[Ti/Fe]	0.30	0.04	0.05	0.20	0.39	···	···
[Cr/Fe]	0.32	0.20	···	···	···	···	···
[Mn/Fe]	0.35	0.25	···	···	···	···	···
[Co/Fe]	0.06	···	···	···	···	···	···
[Ni/Fe]	0.30	0.33	···	···	···	···	···

3.2.1 Hyades

Five stars of the Hyades open cluster had their [F/Fe] measured with the 23358 Å line, and the derived cluster median is 0.17 dex. Unexpectedly, the [F/Fe] ratio deviates by 0.25 dex from the median in star HIP 19316, with A(F) ranging by 0.3 dex. Fig. 20 shows the

Table 9 – Positions and velocities of the Hyades and M 67 stars in the Galactocentric rest frame. Uncertainties assigned as 0.00 pc represent values < 0.005 pc. The position of the Sun is assumed at (X, Y, Z) = (-8200, 0, 25) pc.

Star	X (pc)	Y (pc)	Z (pc)	U (km/s)	V (km/s)	W (km/s)
HIP17766	$-8229.85^{+0.05}_{-0.05}$	$-0.39^{+0.00}_{-0.00}$	$3.94^{+0.03}_{-0.03}$	$-28.06^{+0.20}_{-0.20}$	$230.75^{+0.03}_{-0.03}$	$6.55^{+0.14}_{-0.14}$
HIP19082	$-8242.98^{+0.10}_{-0.11}$	$4.91^{+0.01}_{-0.01}$	$5.88^{+0.05}_{-0.05}$	$-28.87^{+0.24}_{-0.24}$	$230.91^{+0.06}_{-0.06}$	$5.72^{+0.11}_{-0.11}$
HIP19316	$-8240.95^{+0.13}_{-0.13}$	$-0.03^{+0.00}_{-0.00}$	$3.10^{+0.07}_{-0.07}$	$-27.87^{+0.46}_{-0.46}$	$231.42^{+0.07}_{-0.07}$	$5.89^{+0.25}_{-0.25}$
HIP21138	$-8242.56^{+0.07}_{-0.07}$	$-0.88^{+0.00}_{-0.00}$	$8.11^{+0.03}_{-0.03}$	$-28.62^{+0.27}_{-0.27}$	$231.07^{+0.03}_{-0.03}$	$5.98^{+0.11}_{-0.11}$
HIP21256	$-8241.64^{+0.09}_{-0.09}$	$2.34^{+0.00}_{-0.00}$	$11.64^{+0.03}_{-0.03}$	$-29.11^{+0.23}_{-0.22}$	$230.89^{+0.05}_{-0.05}$	$5.56^{+0.08}_{-0.08}$
M 67-0141	$-8775.31^{+18.71}_{-20.41}$	$-413.48^{+13.44}_{-14.67}$	$466.24^{+15.66}_{-14.35}$	$-33.16^{+1.01}_{-1.05}$	$225.93^{+0.53}_{-0.54}$	$-12.56^{+1.36}_{-1.45}$
M 67-0223	$-8796.86^{+31.80}_{-35.80}$	$-427.19^{+22.76}_{-25.62}$	$484.58^{+27.57}_{-24.49}$	$-33.32^{+1.53}_{-1.72}$	$225.45^{+0.55}_{-0.59}$	$-15.22^{+2.36}_{-2.65}$

synthesis of the HF feature in the Hyades targets. From Table 9, we assume membership for all five objects, because they share the same kinematics.

Another odd result from the analysis of the Hyades dwarfs presented in Table 8 is the star-to-star variation of several elements above the 0.1 dex level. Previous studies of open clusters have found large differences in Fe I and Fe II abundances in K dwarfs, which increase with decreasing effective temperature (e.g. Yong et al. (2004); Aleo, Sobotka & Ramírez (2017)). Schuler et al. (2006) also report a trend of increasing O abundances with decreasing temperatures in K dwarfs of the Hyades through measurements of the 7774 Å O-triplet. They suggested photospheric spots as the source of this spurious trend from toy model simulations. Schuler et al. argue that NLTE effects are irrelevant in the temperature range of K-dwarfs presented here, but may be the possible explanation for the increasing [O/Fe] in hotter F-type stars. The differential analysis from Liu et al. (2016) found chemical inhomogeneities in a sample of solar-type Hyades stars, however, their measured intrinsic scatter is below 0.05 dex.

Stars HIP 17766 ($T_{\rm eff}$ = 4268 K) and HIP 21256 ($T_{\rm eff}$ = 4334 K), the ones with H-band observations available, present variations up to $\sim$ 0.3 dex in the element-to-Fe ratio. If we take into account [X/H] instead of [X/Fe], because their adopted [Fe/H] ratios differ by 0.1 dex, differences still persist, notably for O, Sc, Ti and Ni. In Fig. 21 portions of the spectra of these two stars are superposed, and the OH lines show a striking difference between the spectra. The adopted models predict a difference of only 66 K in effective temperatures. A uncertainty of this magnitude in temperature results in a deviation of $\sim$ 0.03 dex in O abundance according to Table 3. Nevertheless, the measured ΔA(O) is 0.15 dex, i.e., $\sim$ 300 K of $\Delta T_{\rm eff}$ would be necessary to account for the difference, assuming linear sensitivity.

The abundance differences for the two Hyades dwarfs with observations in both H- and K-bands are shown in Table 10. To test the possibility of the adopted effective

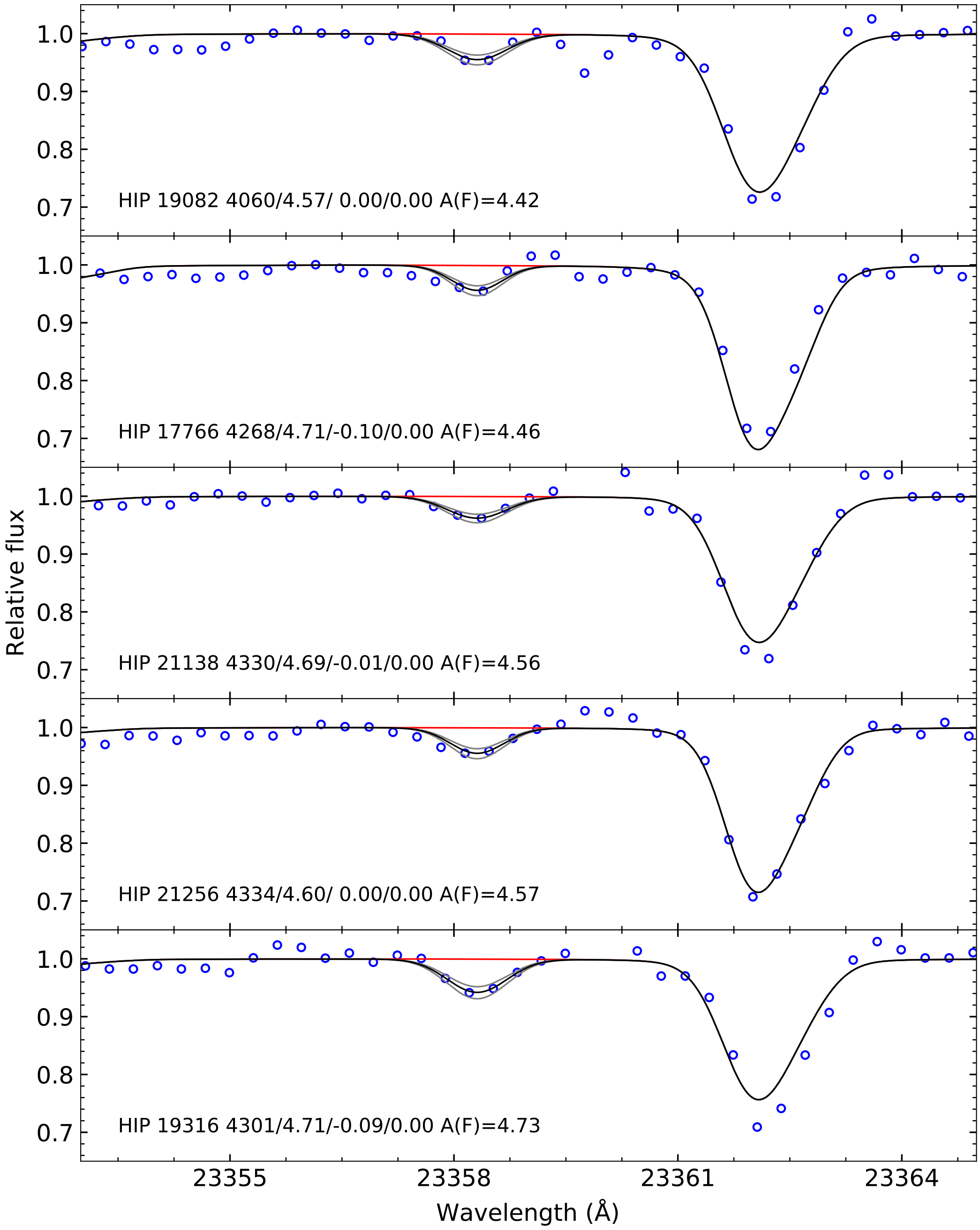

Figure 20 – Spectral synthesis of the HF 23358 Å line for the Hyades dwarfs. Hipparcos ID, adopted atmospheric parameters (in K/dex/dex/km s^{-1}) and F abundance for each star are labelled. *Black lines*: best fits. *Grey lines*: ±1-σ fits. *Red line*: no F. *Blue open circles*: observed spectra. With the exception of HIP 17766 and HIP 21256, the synthesis of the 23362 Å CO line uses solar values for C and O.

temperature being poorly determined in (at least) one of these objects, the abundances of HIP 17766 were estimated for the T$_{\text{eff}}$ taken from the Gaia DR2 catalogue, the same source used for HIP 21256. Also, the change in the abundances was tested for the T$_{\text{eff}}$ determined

Table 10 – Abundance differences between HIP 21256 and HIP 17766. In column 2, $\Delta A(X) = A(X)_{21256} - A(X)_{17766}$. ΔT is the T_{eff} change in model atmosphere of HIP 17766, estimated from the sensitivity in the effective temperature, needed to match the abundance of each element with the respective abundance of HIP 21256. Δ_{Gaia} and Δ_{2MASS} represent the $\Delta A(X)$ if we adopt effective temperatures for HIP 17766 from Gaia DR2 and 2MASS colours, respectively, also estimated from the sensitivity in effective temperature.

	ΔA(X) (dex)	ΔT (K)	Δ_{Gaia} (dex)	Δ_{2MASS} (dex)
C	-0.09	-285	-0.05	-0.06
N	-0.11	-73	0.10	0.05
O	-0.15	-300	-0.08	-0.10
F	0.11	110	0.25	0.22
Si	0.00	0	-0.12	-0.09
K	-0.05	-75	0.05	0.02
Ca	-0.05	-165	-0.01	-0.02
Sc	-0.19	-159	-0.02	-0.06
Ti	-0.16	-192	-0.04	-0.07
Cr	-0.02	-240	-0.01	-0.01
Mn	0.00	0	0.02	0.01
Ni	0.14	-270	0.06	0.08

from 2MASS (J-K) colours, using the calibration of Alonso, Arribas & Martinez-Roger (1996). The estimates are made through the sensitivities of Table 3, assuming linearity. In both cases most abundances agree below the 0.1 dex level, as can be seen in Table 10, *with the notable exception being F*, whose difference in abundances increased above 0.2 dex.

It should be noted that the O abundances of the Hyades stars found in this work are at least 0.3 dex below those found in past studies using the O-triplet and optical spectra of dwarfs (Schuler et al. (2006); Takeda et al. (2013)). Star HIP 21256, underabundant in O, deviates a bit from the F vs. O trend in Figs. 16 and 17. However, the [O/H] value calculated by previous studies would put the Hyades far off the solar neighbourhood F/O trend and underabundant in F with respect to the trend found by Jönsson et al. (2017), The exception is the 'F-overabundant' HIP 19316, which is, however, our dwarf with the closest value found for Gamma Tau (a giant from the same cluster, A(F) = 4.9) by Nault & Pilachowski (2013). The F abundance of Gamma Tau puts this giant right over the trend shown in Fig. 17 if we assume the O abundance from Schuler et al. (triplet) or Takeda et al. (optical). Nevertheless, caution should be taken when comparing dwarfs and giants measured with distinct line lists (e.g., Dutra-Ferreira et al. (2016)), and, while the F abundances are usually taken from one weak and unblended line, systematic effects can arise depending on the lines chosen for measurements of O abundances. We recall that the objects from Jönsson et al. used in the comparison are giants.

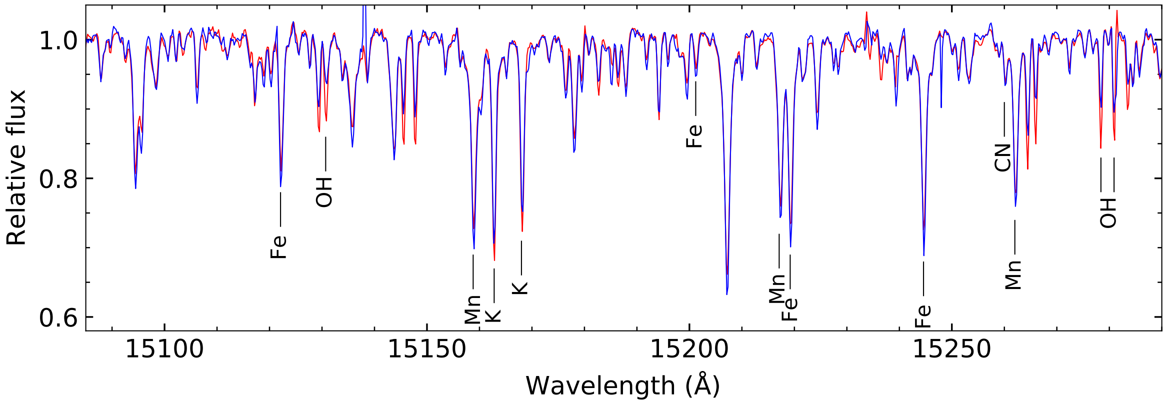

Figure 21 – Superposition of the spectra of HIP 17766 (red line, colder) and HIP 21256 (blue line, hotter), from the Hyades cluster, in a portion of the H-band. Spectral lines measured in this work and some Fe I lines are labelled. The adopted effective temperatures differ by 66 K (see Table 2).

H-band spectrum of HIP 19316 would be useful to investigate the behaviour of the OH lines in K dwarfs and relate it to the odd abundance of F derived for this object. However, we must note that the F overabundance of HIP 19316 can also be effect of badly determined temperature: taking into account the F sensitivity to T_{eff} listed in Table 3, the abundance of this element would fall by 0.18 dex if we adoped the effective temperature inferred for this object by Gaia DR2, 180 K lower. Nevertheless, its Si abundance, already the largest with respect to Fe in the Hyades sample, would increase by 0.15 dex. Furthermore, although the assumption of a colder effective temperature would solve the F spread *in our sample*, it would also further increase the difference between the F abundances of HIP 19316 and Gamma Tau.

Since the atmospheric parameters of the Hyades dwarfs came from different sources and were determined by different methods, a sanity check against this source of inhomogenety in F abundances was performed. Two sets of atmospheric parameters for our K-dwarfs sample were built homogeneously and the synthesis of the HF line was redone. The first parameter set used the T_{eff} values from Gaia DR2 from all stars. Surface gravities were interpolated from T_{eff} and stellar luminosities also taken from Gaia DR2 in a 625 Myr PARSEC isochrone[1] with metallicity $Z = 0.0191$ (Marigo et al., 2017). The second parameter set was built using the $(V\text{-}K)$ colour-temperature relation from Alonso, Arribas & Martinez-Roger (1996), assuming zero extinction due to the proximity of the targets. The 2MASS K_s magnitudes were transformed to the CIT system and then to the TCS system using the calibrations of Carpenter (2001) and Alonso, Arribas & Martinez-Roger

---

[1] <http://stev.oapd.inaf.it/cgi-bin/cmd> (accessed on 12.12.2018).

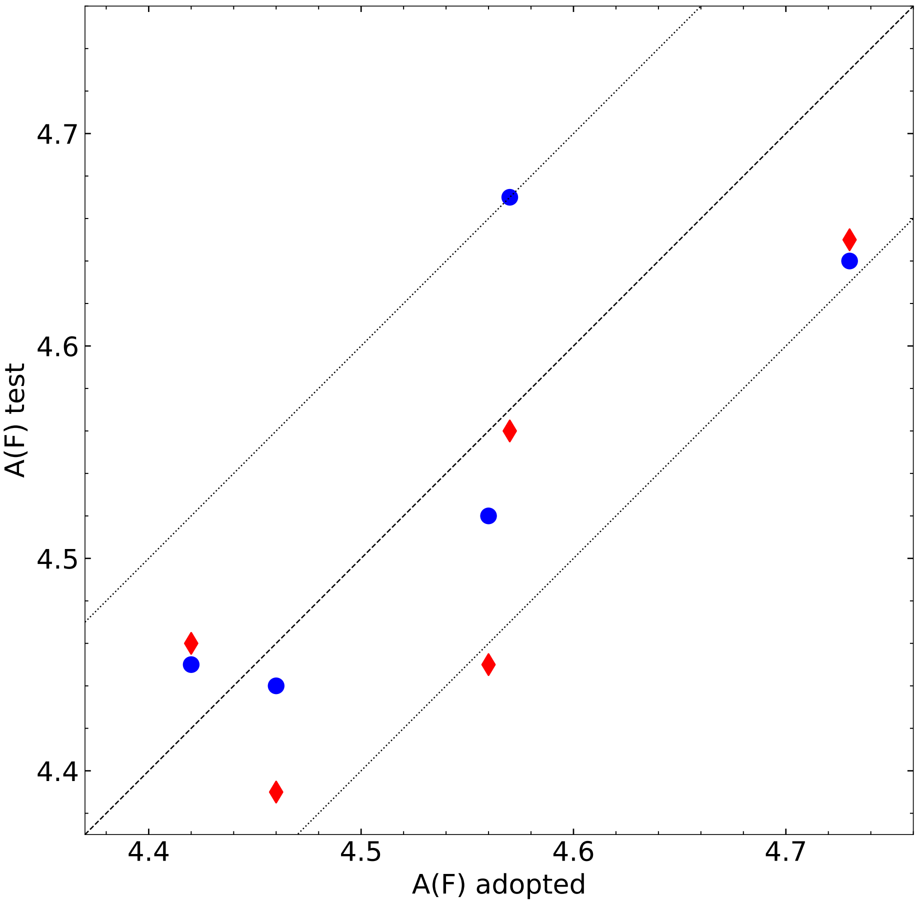

Figure 22 – Comparison between the F abundances in the Hyades dwarfs derived with the adopted atmospheric parameters from Table 2 (abscissa) and the homogeneous test sets of atmospheric parameters (ordinate). *Blue circles*: $T_{\rm eff}$ from Gaia DR2. *Red squares*: $T_{\rm eff}$ from photometric calibration. The dashed line is the identity function and the dotted lines represent 0.1 dex intervals. See text for details on the atmospheric parameters.

(1998), respectively. Derivation of surface gravities used the same isochrone method from the other set, this time interpolating the absolute K_s magnitudes instead of luminosity. In both sets, the log g values range between 4.56 and 4.61 dex, $\sim$ 0.1 dex below those inferred by Aleo, Sobotka & Ramírez (2017) for HIP 17766, HIP 19316 and HIP 21138. The effective temperature interval is 4060:4334 K for Gaia DR2 $T_{\rm eff}$ and 4025:4235 K for colour-temperature $T_{\rm eff}$. Assuming chemical homogeneity, both sets have [Fe/H] = 0.1 dex as metallicity input. The microturbulent velocity was set to zero for all models.

The result of the test is shown in Fig. 22. The scatter in F abundances becomes slightly smaller, with standard deviations of 0.11 and 0.10 dex for Gaia DR2 parameter set and colour-temperature set, respectively. The standard deviation of F abundance in the Hyades with the adopted atmospheric parameters is 0.12 dex. The difference between the higher and lower derived F abundances decreases, but is still relatively high: 0.23 dex in the Gaia DR2 set, and 0.26 dex with the colour-temperature parameters. For the initially adopted parameters, this difference is 0.31 dex. The uncertainty in F abundances due to the atmospheric parameters is estimated at 0.10 dex (Table 3). The microturbulence values could be the main source of scatter in the test sets, because they are guesses taken from those published by Aleo, Sobotka & Ramírez. The estimated sensitivity of the HF line to microturbulence in Hyades spectra is 0.05 dex in abundance for 0.2 km s^{-1} in microturbulent velocity.

Summing up our results for the Hyades and the aforementioned observational issues, it is possible that the current knowledge of K dwarfs atmospheres is incomplete, and further modeling would be needed in case of starspots and/or stellar activity being responsible for the spread in derived abundances, as suggested by Schuler et al. (2006) in the case of the O-triplet. However, this scenario should be considered only after we eliminate the possibility of inappropriate atmospheric parameters being the cause of the star-to-star abundance variations. In any case, an extensive study of FGK dwarfs from several open clusters, observed both in optical and infrared, would be required to verify the supposedly spurious abundance patterns observed here and in past works and trace their origins.

3.2.2 M 67

In the spectra of the two M 67 giants the HF line is barely visible (star 0141) or does not appear (star 0223). For star 0141 an upper limit in [F/Fe] was estabilished. Further studies of F in M 67 must target colder stars – the $T_{\rm eff}$ of star 0141 seems to be the upper limit for detection of the HF feature in this cluster. The value derived here agrees very well with abundances previously calculated for M 67 (Nault & Pilachowski (2013); Maiorca et al. (2014)). No H-band observations are available for these objects.

3.3 CH-, CEMP and Ba-stars

The *peculiar* subsample consists of objects classified as Ba-, CH- and Carbon Extreme Metal Poor stars. CH-stars may be defined as high-velocity stars that exhibit very strong bands created in the optical by the CH molecule and having weak metallic lines (Keenan, 1942; Jorissen et al., 2016). An alternative description would be 'C-rich metal-poor stars from the Galactic halo'. On their turn, the C-rich CEMP stars have different subclassifications, according to the abundances of neutron-capture elements: CEMP-s are s-process rich, CEMP-r are r-process rich, CEMP-rs are rich in both r- and s-process species and CEMP-no present no enrichment in neutron capture elements (e.g., Beers & Christlieb (2005), Masseron et al. (2010), Jorissen et al. (2016)). As argued by

Lucatello et al. (2005) and Jorissen et al. (2016), CEMP-s and CH-stars obey the same mass transfer mechanism, being thus overlapping nomenclatures, while Ba-stars, which, on their turn, are G- and K-type giants with enhanced Ba II, Sr II, CH and CN lines (Bidelman; Keenan, 1951; Allen; Barbuy, 2006), would be their metal-rich counterparts. Their binary nature – a white dwarf companion is detected or assumed for them, except for CEMP-no (Lucatello et al., 2005; Starkenburg et al., 2014) – makes them an ideal astrophysical laboratory to constrain models of AGB nucleosynthesis. It is believed that their former AGB companions left the imprints of the AGB nucleosynthesis yields in the atmospheres of the surviving stars through mass transfer – i.e., they are *extrinsic* F and s-process rich objects (Karakas; Lattanzio, 2014). Since the AGB is the only site of F production observationally confirmed, the study of these binary objects is of crucial importance to constrain the role of the AGBs in the Galactic chemical evolution of this element.

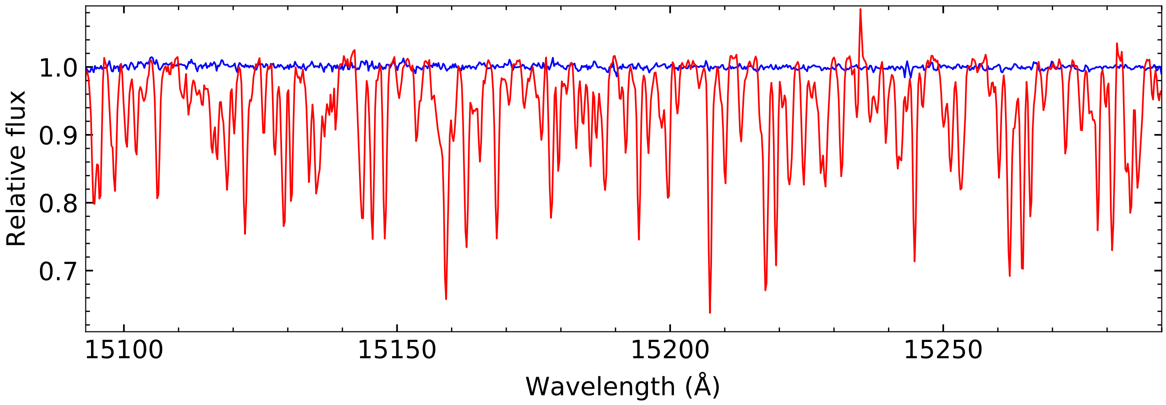

Figure 23 – Comparison of spectra from BD 44 (blue) and the normal giant outer 16 (red).

However, the HF line was detected only in 2 of the 11 observed *peculiar* stars – HD 5223 and HE 0017+0055. For the other targets we calculated upper limits of its F abundances. In the supposed Ba-star HR 8878 ($T_{\rm eff}$ = 4435 K, see discussion on its status as Ba-star in Section 3.3.3.1) the line is barely differentiable from noise. All CEMP, Ba- and CH- stars lacking F measurements are relatively hot ($T_{\rm eff} > 4500$ K). At these temperature regimes the HF feature is not observable unless F is exceptionally overabundant. HE 0002+0053, which is colder ($T_{\rm eff}$ = 4225 K), in the same temperature range of the outer disc stars analysed in Section 3.1, has a spectrum apparently affected by the process of telluric subtraction in the 23358 Å region – the region of the HF line is noisy and unexpectedly flat – impairing the spectral fitting process of the HF line.

Star BD 44, identified as a CEMP-no, presents a featureless spectrum in both H- and K-bands – see Fig. 23, where a typical portion of the spectrum of this object is shown.

Despite having molecular features present in its optical spectra (Ito et al., 2009), this object, a CEMP-no, is the hottest in the sample (T_{eff} = 5510 K) and very metal-poor ([Fe/H] = -3.73). Even the strongest OH and CO lines are absent in the IR regions studied in this work – the CO 3-1 bandhead at 23220 Å seems to be barely visible. Therefore, star BD 44 has been excluded from the analysis.

3.3.1 CH-stars

Table 11 – Abundance ratios derived for CH-stars. Values with the '<' sign are upper limits.

[X/Y]	HD 224959	HD 26	HD 5223
[Fe/H]	-2.44	-1.13	-2.11
[C/Fe]	2.23	0.87	0.91
[N/Fe]	2.00	0.57	1.06
[O/Fe]	0.54	0.34	0.92
[F/Fe]	**<2.54**	**<1.62**	**1.42**
[Na/Fe]	···	0.31	0.41
[Mg/Fe]	0.68	0.59	0.47
[Al/Fe]	···	0.32	0.07
[Si/Fe]	0.72	0.46	0.60
[K/Fe]	···	0.54	-0.09
[Ca/Fe]	···	0.41	0.77
[Ti/Fe]	···	0.06	···
[Mn/Fe]	···	0.23	-0.35
[Ce/Fe]	2.21	1.47	1.66

HD 5223 is the only CH- target with F abundance measured (see Table 11 for abundance ratios in CH-stars), and its [F/Fe] ratio is 1.42 dex. It is a very metal-poor giant ([Fe/H] = -2.11, log g = 1.00), thus we expect an old age and, therefore, a subsolar initial mass. The estimated binary mass function from radial velocity observations is f(m) = 0.082 (Pourbaix et al., 2004). If we estimate a mass of 0.8 $M_\odot$, the minimum mass for the companion white dwarf is $\sim$ 0.5 $M_\odot$, or an initial mass of $\sim$ 0.8 $M_\odot$ as well if we apply the theoretical initial-final mass relation from Romero, Campos & Kepler (2015) (their Fig. 4) to get a rough estimate[2]. The minimum mass of the WD M_{WD} is estimated through:

$$f(m) = \frac{M_{WD}^3}{(M_{\text{obs}} + M_{WD})^2}, \tag{3.1}$$

which is the definition of the binary mass function for an inclination angle of 90 degrees (Karttunen et al., 1996). A more general formula – for an orbital inclination i – has the

---

[2] A caveat should be made here: to estimate the initial masses of the WD progenitors we are assuming that the mass accreted *by the former AGB companion* during the mass transfer is negligible and its mass loss occurred as predicted for a non-interacting system.

right-hand side multiplied by $\sin^3 i$. In the case of HD 5223, it may be concluded that the minimum mass of the companion should be underestimated. The chemistry of HD 5223 indicates pollution from a former AGB companion which experienced a third dredge-up, therefore its minimum initial mass estimative should be set at $\sim 1.2\ M_\odot$, suggesting that the plane of the orbit is not edge-on. Its [Ce/Fe] value is 1.66 dex, further indicating pollution from mass transfer, since Ce is a s-process dominated element (Sneden; Cowan; Gallino, 2008).

HD 5223 has measurements made with both optical and IR spectra available in the literature. The atmospheric parameters adopted for this star came from Goswami et al. (2006), and most abundance ratios derived here agree with their work inside the 0.1 dex interval. Exceptions are C, Ca and Ce, albeit both Ce measurements are enhanced and indicative of pollution from a former AGB companion. Our value for Ca – [Ca/Fe] = 0.77 – is based in only one line. The other Ca lines were considered unreliable and this may be the case for the line considered in our measurements. The abundance of C from this work strongly diverges from that calculated through the synthesis of the C_2 Swan 0-1 band around 5635 Å by Goswami et al., being $\sim$ 0.7 dex below their value. Meanwhile, Lucatello et al. (2011) presented abundances of N, O, F and Na measured in the IR. The results from Lucatello et al. diverge from ours for all four elements by ± 0.3-0.4 dex, the difference being probably due to the different atmospheric models adopted. Their A(F) is 0.30 dex higher – the HF line from their spectrum, shown in their Fig. 1, is slightly depper than in ours, but this is probably due to the different instrumental profiles. The difference in the F results must be consequence of adopting different atmospheric models – the ratio between the equivalent widths would account for only $\sim$ 0.05 dex, below typical uncertainties. For O, the discrepancy between our value and that found by Lucatello et al. can be attributed, as stated, partially to atmospheric models. Since the O abundance calculated here is 0.3 dex above their value and their synthesis relied in K-band CO lines for O, the difference can be partially attributed to the discrepant C abundances adopted as well. We also recall that the O abundance presented here for HD 5223 is based on only one OH line at 15572 Å. While Goswami et al. used a 1D LTE Kurucz model similar to ours, Lucatello et al. adopted a CN-enhanced OSMARCS model, also employing the same atmospheric parameters from Goswami et al..

Making a first approximation comparison with the Z=0.0001 yields from Lugaro et al. (2012) as upper limits of mass transfer[3], the C, F, Na and Ce ratios are compatible with some degree of pollution from a former AGB companion in HD 5223, though it is difficult to reconcile the observed C/N ratio, much higher than any of those presented in their yields. That is, if both the observations and the yields are correct, the transfer of N

---

[3] The correct approach to estimate the chemistry involved in mass transfer is to evaluate the evolution of surface abundances in the TP-AGB, because the mass transfer process may happen at any time during this phase, as the AGB companion is losing mass continuously.

would have been much more efficient – therefore, a careful analysis of the time-evolution of the surface abudnaces in the TP-AGB is needed.

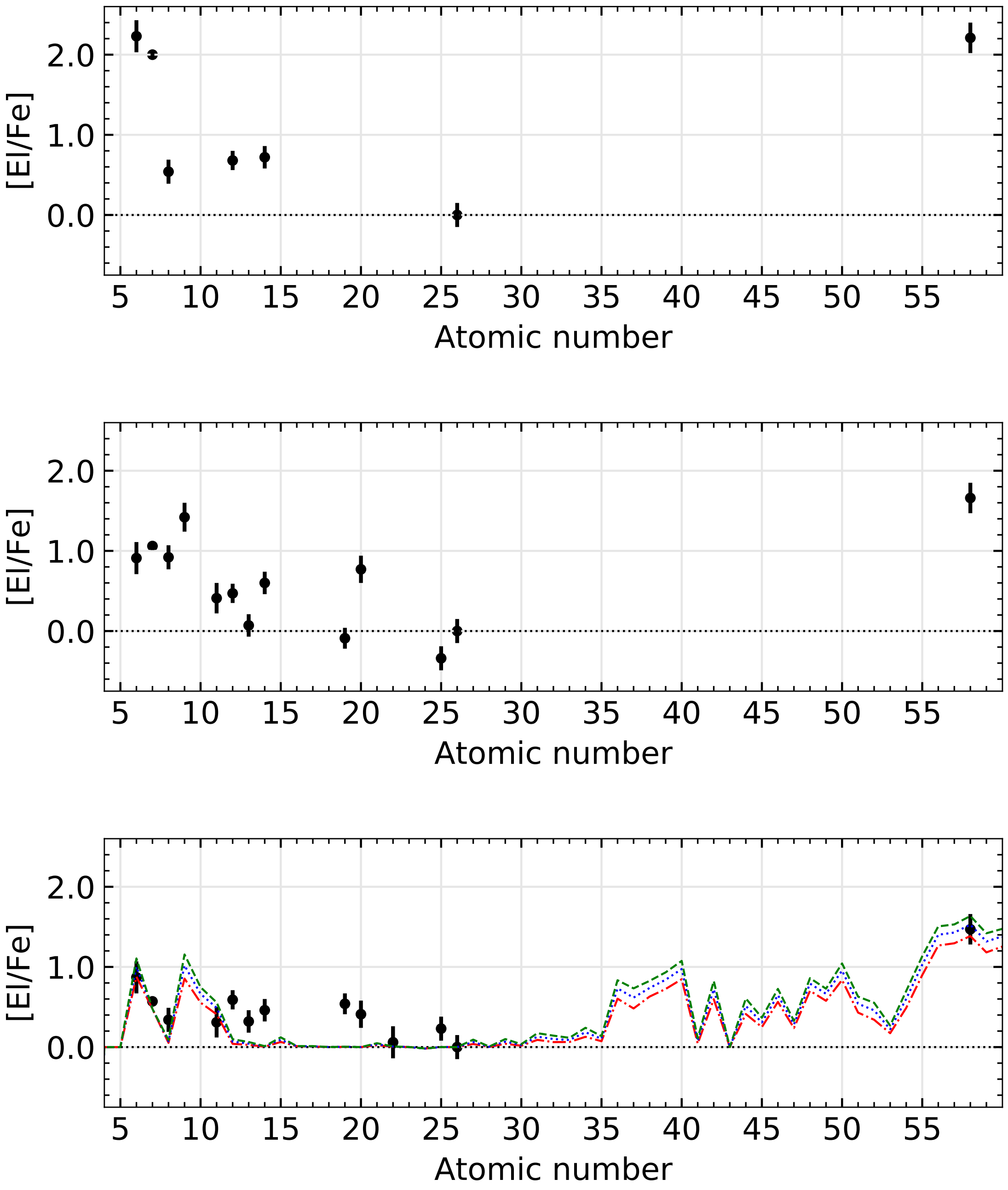

Figure 24 – Abundance ratios for the CH-stars. *Top*: HD 224959. *Center*: HD 5223. *Bottom*: HD 26, with lines showing surface abundances of a Z=0.001, 3 $M_\odot$ star in TP-AGB (Fishlock et al., 2014), thermal pulses #8 (red dashed-dotted), #9 (blue dotted) and #10 (green dashed).

Star HD 26 has been relatively well studied with optical spectra – it first came into attention thanks to its 'unusually high' radial velocity (Keenan; Keller, 1951). Later, Wallerstein & Greenstein (1964) noted enhancement in C and s-process elements through a curve of growth analysis of its spectrum. Then, Vanture (1992a), Vanture (1992b), Vanture

(1992c), made a series of high-resolution analysis of CH-stars, featuring measurements of CNO and some heavy elements for HD 26. Concerning the binarity of the object, Jorissen et al. (2016) derived eccentricity e = 0.08 and a minimum orbital period of 54 years – the longest known among chemically peculiar stars – through radial velocity time series. They estimated the binary mass function f(m) as 0.075. Assuming the primary has 0.8-1.0 $M_\odot$ (it should be an old star due to its low metallicity), we estimate the minimum mass for the companion white dwarf in the 0.5-0.6 $M_\odot$ range, or an initial mass of 0.9-1.4 $M_\odot$. Yet, taking into account that the companion must have had third dredge-up, 1.2-1.4 $M_\odot$ for minimum initial mass. More recent detailed chemical abundance studies, always with optical spectra, include Van Eck et al. (2003), Masseron et al. (2010) and Goswami, Aoki & Karinkuzhi (2016), the later having adopted the same atmospheric parameters and model used in this work. The abundances from Goswami, Aoki & Karinkuzhi usually agree with ours in the 0.2 dex range, except for Mn and for individual abundances of C and N – however, the average [CN/H] shows agreement below 0.1 dex. Goswami, Aoki & Karinkuzhi point out that this star has 'no clear good Mn lines' in its optical spectrum. Unfortuantely, the HF line is undetectable in HD 26 spectrum, and the upper limit derived for [F/Fe] is 1.62 dex. As in past studies, we found strong enhancement in the s-process element Ce, an indicative of enrichment from a former AGB companion. Fishlock et al. (2014) published surface abundances for thermal pulses in AGB stars with metallicity compatible with HD 26 (Z=0.001). As shown in Fig. 24, the abundance pattern of this object is compatible with a former companion of 3 $M_\odot$, consistent with its estimated minimum mass. Despite the abscence of F measurements, the estimated upper limit is compatible with the model – which predicts [F/Fe] = 1.0, as well as the reported CNO, Na and Ce. Goswami, Aoki & Karinkuzhi (2016) published abundance ratios for several s-process elements. While Sr and Ba are overabundant by 1 dex w.r.t. the models we plotted in Fig. 24, their published values for Y, Zr, La, Ce, Pr and Nd fall on the curves plotted here. It is important to note that deviation presented by some species, such as Mg, Ca and Si, may be due to the fact that the models are scaled to the solar composition, and metal-poor stars commonly have enhancement in α-elements, whose production in AGB stars is usually negligible.

HD 224959 has also been studied along HD 26 in some of the aforementioned chemical analysis papers (Vanture, 1992a; Vanture, 1992b; Vanture, 1992c; Van Eck et al., 2003; Masseron et al., 2010; Goswami; Aoki; Karinkuzhi, 2016). With very few elements measured in common, we may note that our C and O abundances are $\sim$ 0.2 dex higher than those of Goswami, Aoki & Karinkuzhi (2016), where the same atmospheres were employed. Also, both studies present the same level of enhancement in Ce, with our [Ce/Fe] value being 2.21 dex. The F abundance may be very high as well, because the estimated upper limit is [F/Fe] $<$ 2.54. HD 224959 is present in the orbital analysis of Jorissen et al. (2016) and its period is estimated as P = 1273 days (e = 0.18). The binary mass function f(m) = 0.093 suggests a WD companion with at least 0.55 $M_\odot$, which corresponds to an initial mass of ∼ 0.9 $M_\odot$, again suggesting that the plane of the orbit is not edge-on, since we expect a higher progenitor initial mass due to the observed peculiar chemistry. We must point out that this object also has only one OH line measured for O abundance. The lack of clear, measurable OH lines is a problem shared by all stars with effective temperatures above 4500 K in our sample. The chemical pattern of this object is compatible with pollution from a 2 $M_\odot$ companion if we take the yields of C, O, F and Ce from Lugaro et al. (2012) as upper limits of mass transfer. However, the excessive observed abundance of N does not agree with their models.

3.3.2 CEMP stars

Table 12 – Abundance ratios derived for CEMP stars. Values with the '<' sign are upper limits.

[X/Y]	HE 0002+0053	HE 0017+0055	HE 0310+0059
[Fe/H]	-2.18	-2.40	-1.32
[C/Fe]	1.26	1.97	0.92
[N/Fe]	1.94	···	1.46
[O/Fe]	···	0.87	···
[F/Fe]	···	**0.57**	<**1.35**
[Na/Fe]	···	···	2.27
[Si/Fe]	···	···	1.24
[Ti/Fe]	···	···	1.42

HE 0017+0055 is the only CEMP star from our sample with a derived abundance of F, having a mild enhancement of [F/Fe] = 0.57 (A(F) = 2.57). Regarding the CNO elements, it is the only target with an Oxygen measurement as well – the synthesis of the 16909 Å OH line determined [O/Fe] = 0.87. This abundance ratio is expected for a CEMP of [Fe/H] ∼ -2.4 (Masseron et al., 2010). The A(C) agrees with that calculated by Kennedy et al. (2011), the difference in the [C/Fe] ratio between both works being due to the different [Fe/H] values adopted. In comparison with the results of Jorissen et al. (2016), who used the same atmospheric parameters but with a C-enhanced MARCS model, the A(C) value found in this work differs by 0.2 dex. Jorissen et al. found elevated r-process abundances in HE 0017+0055, classifying it as a CEMP-rs star. Unfortunately, no abundances for N, Ce and other elements were measured, since in many regions the continuum normalization was impaired by the CN blanket. Jorissen et al. also published a radial velocity analysis of HE 0017+0055 – the binary mass function is so negligible (f(m) ≈ 10^{-6}) that it is impossible to constrain the mass of the supposed white dwarf companion. In comparison with the yields from Lugaro et al. (2012), which, we recall, give an upper estimative, we suppose from C and F abundances derived here that the mass transfer should be highly inneficient in this system, but a more detailed chemical analysis must be carried out before any conclusions.

Star HE 0002+0053 has measurementes of only two elements, C and N. It lacks observations in the H-band, and we adopted the O abundance from Kennedy et al. (2011) – the same source of the atmospheric parameters – to perform the synthesis of CO lines. Only two CO lines and one CN line were considered for the synthesis. As previously mentioned, the region of the HF line seems to be affected by telluric contamination, leaving HE 0002+0053 without a measurement of F. The [C/Fe] found is $\sim$ 1 dex below the value derived by Kennedy et al. – they did not publish results for N.

As pointed out for HE 0017+0055 by Jorissen et al. (2016), the surface gravity derived by Kennedy et al. and adopted here for HE 0002+0053 (log g = 0.27) may be underestimated. Using the Eq. 2.65 to find the luminosity, the minimum value estimated for HE 0002+0053 with the effective temperature and log g from Kennedy et al. is 3380 $L_\odot$ – assuming the object is a giant star, we impose a minimum mass of $\sim$ 0.8 $M_\odot$. If the adopted surface gravity is correct, this object is among the most luminous CEMP stars (Masseron et al. (2010), fig. 12).

Nonetheless, its absolute magnitude – and, then, its surface gravity – can be estimated through the parallax using Eq. 2.64. Adopting the Gaia DR2 parallax of 0.0675 mas, the absolute magnitude M_V is estimated as -2.63. Using the eq.(9) from Torres (2010) with the constants defined as in Section 2.4, the corresponding luminosity is 1920 $L_\odot$. Therefore, the surface gravity of HE 0002+0053 derived using simply the parallax is 0.53 dex. However, HE 0002+0053 has the smallest parallax of our sample with high relative parallax error ($\sigma_\varpi/\varpi = 0.6$). The distance inferred through the Bayesian analysis described in Section 2.4, which takes into account the high relative error in parallax, is 3 kpc lower than the naive inversion of the parallax. The distance modulus then derived implies an absolute magnitude M_V = -2.06 and the corresponding surface gravity is 0.75 dex. While the value adopted by Kennedy et al. (2011) seems underestimated, it is on the border of the uncertainty in log g if we consider the surface gravity derived with parallax. No value for luminosity is available for this object in Gaia DR2, preventing a comparison.

The HF line is undetectable in star HE 0310+0059, and the upper limit of [F/Fe] in this target is 1.35 dex. The only known spectroscopic abundance analysis of HE 0310+0059 is the CO measurement of Kennedy et al. (2011) – Goswami (2005) made a qualitative analysis of its optical spectrum. We adopted the [O/Fe] from Kennedy et al. due to the lack of H-band spectrum (see Table 1), which also prevent the probing of its s-process content through Ce. The [C/Fe] we measured from CO lines is 0.35 dex below the value found by Kennedy et al.. Na seems to be very enhanced, with [Na/Fe] = 2.27, and high abundance ratios were measured for Si and Ti as well (see Table 12). In the specific cases of Si and Ti, the overabundances could be due to blends with not listed C/CN features.

3.3.3 Ba-stars

Table 13 – Abundance ratios derived for Ba-stars and HR 8878. Values with the '<' sign are upper limits.

[X/Y]	HD 5424	HD 27271	HD 210946	HR 8878
[Fe/H]	-0.51	0.04	-0.22	-0.60
[C/Fe]	⋯	-0.37	-0.16	0.17
[N/Fe]	⋯	0.29	0.32	0.32
[O/Fe]	⋯	-0.25	-0.17	0.57
[F/Fe]	**<0.68**	**<0.56**	**<0.26**	**<0.10**
[Na/Fe]	0.65	0.40	0.13	0.23
[Mg/Fe]	⋯	-0.10	-0.10	0.25
[Al/Fe]	⋯	-0.09	0.03	⋯
[Si/Fe]	0.28	0.20	0.22	0.32
[K/Fe]	⋯	-0.10	0.12	0.14
[Ca/Fe]	0.49	-0.17	-0.15	0.46
[Ti/Fe]	⋯	-0.38	-0.43	0.62
[Cr/Fe]	⋯	-0.11	0.04	-0.01
[Mn/Fe]	⋯	-0.16	0.00	0.01
[Co/Fe]	⋯	-0.45	-0.19	⋯
[Ni/Fe]	⋯	-0.27	-0.05	⋯
[Ce/Fe]	⋯	0.14	0.54	-0.03

HD 210946, a confirmed spectroscopic binary with P = 1529 d, e = 0.126 and f(m) = 0.041 (Udry et al., 1998), has abundance ratios for all elements considered, except Sc, V and, unfortunately, F. For the later, [F/Fe] < 0.26 was derived as upper limit. Our analysis suggests the characterization of HD 210946 as a mild Ba-star, with moderate s-process enhancement – [Ce/Fe] = 0.54. This work presents the first measurements of CNO for this object, with its [C/Fe] corresponding to the lower limit of the sample from Barbuy et al. (1992) and below the most C-poor star from Allen & Barbuy (2006).

Assuming a mass of 2.3 $M_\odot$ for HD 210946 from its spectral type – K1IIIBa1, (Gray, 2005; Pourbaix et al., 2004) – its companion should have a minimum initial mass of 3 $M_\odot$. An upper limit for the inital companion mass may be set at 4.5 $M_\odot$, due to the [Ce/Fe] found in our measurements, since the Ce production is negligible above this initial mass in Z=0.007 stars (Karakas; Lugaro, 2016). Taking into account these mass constraints and the available abundance ratios, it may be suggested that mass transfer occured at the beggining of the TP-AGB phase of a 4 $M_\odot$ companion. A model of its surface abundances at thermal pulse #6 is plotted in Fig. 25, providing good fits for C, N, Na and Ce abundances.

The values found in the IR (see Table 13) agree with those measured with optical spectrum by Liu, Liang & Deng (2009), whose atmospheric parameters were adopted in this work. On the other hand, de Castro et al. (2016) found $T_{\rm eff}$ = 4800 K and log g = 2.1

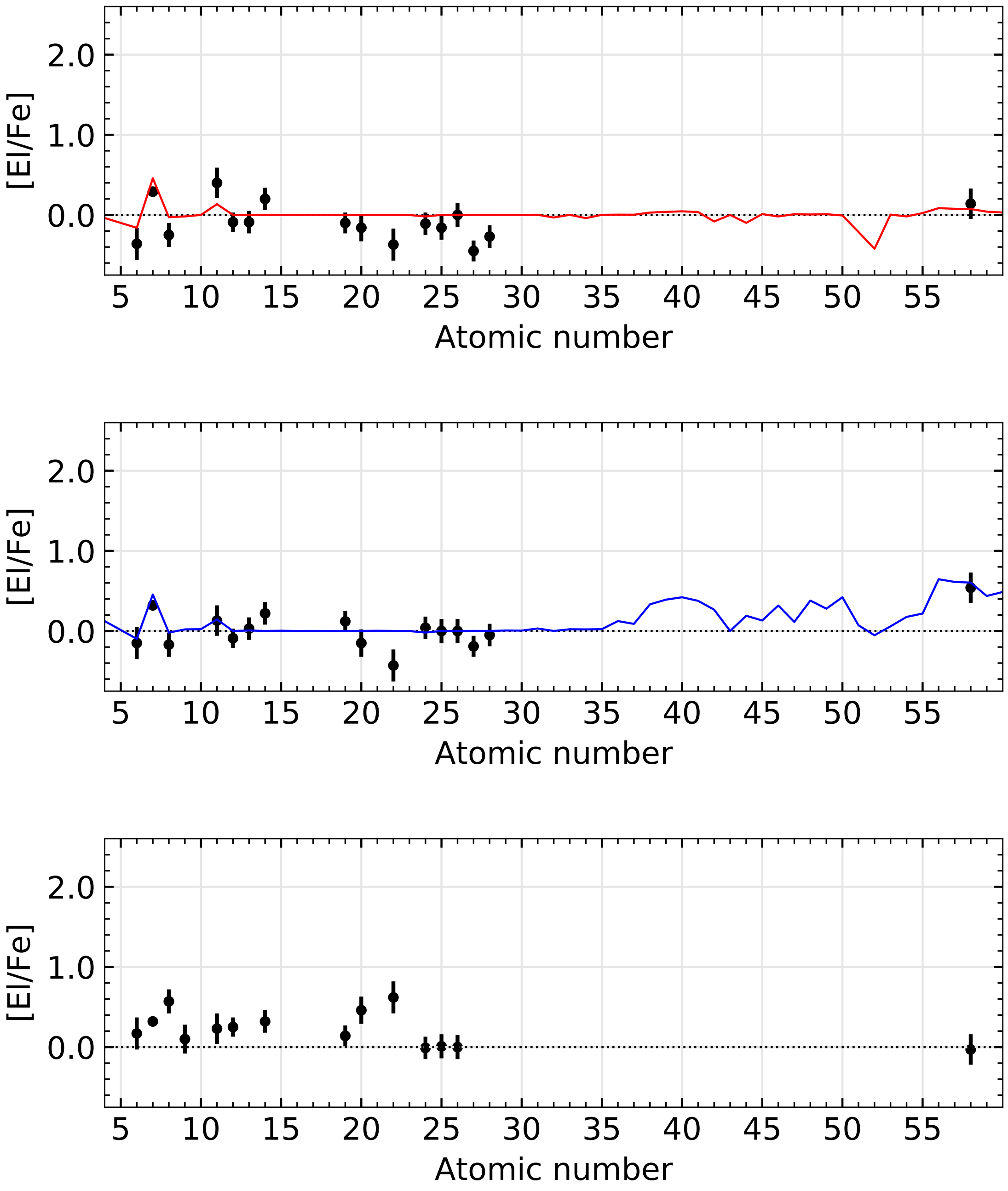

Figure 25 – Abundance ratios for two of the Ba-stars and HR 8878. *Top*: HD 27271, with red solid line showing surface abundances of a solar metallicity, 3 $M_\odot$ star in TP-AGB, thermal pulse #13 (Karakas; Lugaro, 2016). *Center*: HD 210946, with blue solid line showing surface abundances of a solar metallicity, 4 $M_\odot$ star in TP-AGB, thermal pulse #6, also from Karakas & Lugaro. *Bottom*: HR 8878.

dex for this target. A higher temperature would imply a higher upper limit for [F/Fe] in HD 210946. Notwithstanding, de Castro et al. employed their atmospheric parameters to estimate the spectroscopic distance of the star, which is overestimated by more than a factor of two with respect to the distance we inferred with Gaia DR2 data – 320 ± 6 pc. Substituting their atmospheric parameters by those adopted in this work in their eq. (1), a spectroscopic distance of 474 pc is estimated, closer to the distance derived with geometric parallax. Therefore, we assume that the atmospheric parameters from Liu, Liang & Deng are more adequate, unless the mass of the star has been strongly overestimated by de Castro et al. – which is a possibility, since they estimated 4 $M_\odot$, almost two times the value we suggested in this work – and/or relevant systematic errors affect the adopted photometric values.

HD 27271, also confirmed as a spectroscopic binary by Udry et al. (1998) with P = 1694 d, e = 0.217 and f(m) = 0.024, does not have the HF line present in its spectrum. The binary mass function yields a companion with initial mass lower than the 2.3 $M_\odot$ assumed from the spectral type, i.e., the minimum initial mass of the companion is at least 2.3 $M_\odot$, because it obviously evolved faster. The upper limit of 0.56 dex was determined for [F/Fe]. Also, its H-band OH lines are weak ($T_{\rm eff}$ = 4830 K), prompting us to adopt the A(O) from Barbuy et al. (1992). The CNO abundances from Barbuy et al. are somewhat lower than those from Allen & Barbuy (2006), with the average A(C+N+O) diverging by ∼ 0.2 dex. We calculated the C and N abundances using the adopted A(O), and our CNO results are consistent with those from Barbuy et al. (1992). Liang et al. (2003) derived A(O) = 9.16, 0.7 dex greater than the value from Barbuy et al.. The differences in the CNO elements have not resulted in any systematic shift, apparently. The only elements whose abundances are consistently higher/lower in our results than those of both Allen & Barbuy (2006) and Liang et al. (2003) are Na and Ni, respectively. While all works with measurements of s-process elements have shown enhancement of these species, it is noteworthy that the A(Ce) found in this work is 0.5 below the value found by Allen & Barbuy (2006). In Fig. 25 a TP-AGB model with solar metallicity and 3 $M_\odot$ (Karakas; Lugaro, 2016) is plotted with the observed abudances. The surface abundances of its thermal pulse #13 were chosen because they represent the best fit to the C, N and Ce abundance ratios measured in this work. Unfortunately, a better mass constraint is impaired due to the lack of F measurements. Models with higher masses were avoided in the plot becuse they yield much higher N abundances and less Na, whose measurement already has some overabundance w.r.t. to the curve.

The spectroscopic binary HD 5424, with P = 1881 d, e = 0.226 and f(m) = 0.005 (Udry et al., 1998), was observed only in the K-band. With $T_{\rm eff}$ = 4700 K, the HF line was not detected, and a upper limit [F/Fe] < 0.68 was established. Measurements were performed only for Na, Si and Ca. In comparison with Allen & Barbuy (2006), we derived abundances greater than theirs by ∼ 0.5 dex for Na and Ca, while both Si abundances agree. The same differences arise when our values are compared with those from de Castro et al. (2016). Despite our Si abundances agreeing with those of both Allen & Barbuy and de Castro et al., it is necessary to point out that our result for this element comes from only two lines whose derived abundances differ by 0.4 dex.

3.3.3.1 HR 8878

Table 14 – Positions and velocities of the binaries and HR 8878 in the Galactocentric rest frame. Uncertainties assigned as 0.00 pc represent values < 0.005 pc. The position of the Sun is assumed at (X, Y, Z) = (-8200, 0, 25) pc.

Star	X (pc)	Y (pc)	Z (pc)	U (km/s)	V (km/s)	W (km/s)
HD 224959	-8235^{+2}_{-3}	400^{+30}_{-26}	-761^{+51}_{-58}	342^{+24}_{-21}	-29.03^{+14}_{-17}	-11^{+8}_{-10}
HD 26	$-8246.2^{+0.8}_{-0.9}$	184^{+3}_{-3}	-221^{+4}_{-5}	-253^{+5}_{-6}	-106.48^{+4}_{-4}	60^{+2}_{-2}
HD 5223	-8409^{+6}_{-7}	313^{+11}_{-10}	-278^{+10}_{-10}	-155^{+9}_{-9}	-103.45^{+7}_{-7}	137^{+2}_{-2}
HE 0002+0053	-9171^{+244}_{-364}	5676^{+2132}_{-1427}	-9795^{+2468}_{-3688}	-28^{+12}_{-18}	304.19^{+19}_{-13}	35^{+13}_{-9}
HE 0017+0055	-8758^{+85}_{-123}	1839^{+405}_{-280}	-3401^{+522}_{-756}	19^{+2}_{-2}	47.06^{+25}_{-36}	-10^{+13}_{-19}
HE 0310+0059	-9024^{+32}_{-35}	$15.1^{+0.7}_{-0.6}$	-821^{+33}_{-36}	$3.4^{+0.5}_{-0.5}$	211.58^{+2}_{-2}	$2.9^{+0.5}_{-0.5}$
BD 44	-8356^{+2}_{-2}	130^{+2}_{-2}	$-28.3^{+0.7}_{-0.8}$	43^{+1}_{-2}	67.65^{+1}_{-1}	$58.4^{+0.3}_{-0.3}$
HD 210946	-8095^{+2}_{-2}	212^{+4}_{-4}	-191^{+4}_{-4}	$19.4^{+0.3}_{-0.3}$	$241.41^{+0.6}_{-0.6}$	$12.7^{+0.6}_{-0.6}$
HD 27271	-8432^{+5}_{-6}	-44^{+1}_{-1}	-122^{+3}_{-4}	69^{+1}_{-1}	200.74^{+1}_{-1}	-24^{+1}_{-1}
HD 5424	$-8203.6^{+0.1}_{-0.1}$	$-10.9^{+0.3}_{-0.3}$	-514^{+15}_{-15}	82^{+2}_{-2}	194.63^{+2}_{-2}	$5.6^{+0.4}_{-0.4}$
HR 8878	$-8194.7^{+0.1}_{-0.1}$	66^{+1}_{-1}	-56^{+2}_{-2}	$-3.7^{+0.4}_{-0.5}$	$241.48^{+0.7}_{-0.7}$	$-53.3^{+0.6}_{-0.6}$

Star HR 8878, as seen in Table 13, has [F/Fe] < 0.10; A(F) < 3.90, the same upper limit found by Pilachowski & Pace (2015) in their analysis of normal solar neighbourhood stars. This object has been treated as a Ba-star in some works, but others, notably Smiljanic, Porto de Mello & da Silva (2007) and Allen & Porto de Mello (2011), conclude that it is a chemically normal star. The discussion on the status of this star apparently exists due to the Ba overabundance measured by Zacs (1994) – who found [Ba/Fe] = 0.42. A recent NLTE analysis by Korotin et al. (2015) measured [Ba/Fe] values in four spectral lines, obtaining results similar to Allen & Porto de Mello. Our analysis of the infrared spectrum of HR 8878 suggests that it is indeed a normal star, without enhancement in Ce and C, as shown in Fig. 25. Also, no evidence of binarity is known to us – Beavers & Eitter (1986) made time series measurements of radial velocity for this object, among others, but their amount of data for HR 8878 is too scarce to draw any conclusions. Without radial velocity data to support (or not) any evidence for binarity, a check for long period binaries (2000-4000 days) by comparison of Hipparcos (ESA, 1997) and Tycho-2 (Høg et al., 2000) proper motions was first proposed by Kaplan & Makarov (2003), and used in later studies of Ba-stars (see, e.g., Jorissen et al. (2005) for a brief justification of the method). This check, a chi-squared test, was fully described by, e.g., Frankowski, Jancart & Jorissen (2007). In short, the χ^2 is evaluated by:

$$\chi^2 = \boldsymbol{\mu^T} S^{-1} \boldsymbol{\mu}, \tag{3.2}$$

where $\boldsymbol{\mu}$ is the two dimensional vector containing the difference between the proper motion components from Hipparcos and Tycho-2, and S is a covariance matrix, shown in the eq. (9) from Frankowski, Jancart & Jorissen. The quantity calculated with Eq. 3.2 is assumed to follow a χ^2 distribution with two degrees of freedom, implying that binarity can be rejected with 90% of confidence for $\chi^2 < 4.605$. In the case of HR 8878, we found $\chi^2 = 0.916$, suggesting that it does not belong to a long period binary system.

If HR 8878 is treated as a normal solar neighbourhood star, it seems slightly underabundant in the F/O ratio with respect to the trend found by Jönsson et al. (2017). Its α-elements abundances, when compared with the results from Alves-Brito et al. (2010) seem typical of the thick disc, despite its thin disc kinematics – confirmed by Pilachowski & Pace – see also Table 14. However, as discussed in Sect. 3.1, comparisons between α-elements abundances derived in IR with those measured in optical must be taken with caution.

4 Conclusions and perspectives

Emerging from the quest on the cosmic origin and evolution of the chemical element F, with all its intricacies, we will first summarize our findings. Regarding the outer disk stars where we were able to measure both F and O chemical abundances, we found the possibility of a chemical history in the outer disc field which may be different from that in the solar neighbourhood. Our results seem to show a minor secondary behaviour of F in the Galactic region studied, and the [F/O] slope seem less strong. This may give the hypothesis of F nucleosynthesis by the ν-process a survival chance, at least in the outskirts of the Galactic disc. Nevertheless, we must point out that we have only four stars with O measurements available. Further exploration must be done before taking any conclusions – anyway, here we present interesting results in this regard.

One of the hypothesis we tested is the possibility of abundance gradients in [F/Fe] along the Galactic disc. We have not found any suggestions of a F gradient between the solar neighbourhood and the outer disc region located between 2 and 4 kpc from the Sun, neither any hints of vertical F gradients. However, the lower abundance ratio found in the most distant star, outer 16, may stimulate some astronomers to look for gradients at that region and beyond, a task which will be facilitated by dedicated near-IR spectrographs operating at 30-m class observatories. Also, our results for [F/Fe] corroborate the findings from Jönsson et al. (2017) that, at least for solar metallicity, F grows with Fe. This will have implications in chemical evolution and stellar nucleosynthesis models, because they fail to reproduce the observed behaviour of [F/Fe] against [Fe/H].

Other interesting findings in the outer disc sample are the differences in the measured abundances of Si and Ti and, to a less extent, Mn. These differences were not found in our measurements of Arcturus and μ Leo, thus, what is happening? The atmospheric parameters and models are the same, therefore one possible culprit must be one of the line lists. Another possible culprit may be the solar-scaled model atmosphere plus blending with C-bearing molecules, which is stronger in the IR – but, if that is the case, we would have found the same problem in the CH-stars and in other abundances from the outer disc stars themselves. In the CH-stars we found results compatible with other works in the literature which rely in the very same atmospheres adopted here. Also, high Na abundance ratios, pointing to a possible GC origin of the outer disc sample, which is, on the other hand, dismissed by N abundances and kinematics. Our findings point to the need of more investigation of these stars in the optical, where O, Na, Ca and CN measurements would be very welcome.

In the K-dwarfs from the Hyades open cluster we found a scatter in abundances which point to the importance of well defined atmospheric parameters. We took our adopted atmospheric parameters from different sources in the literature, and, at least for most elements, it seems to be the main reason behind their scattered abundances, a problem that seems to have affected the F analysis from Pilachowski & Pace (2015), for instance. That is, the atmospheric parameters must be determined in the most homogeneous manner. However, we built sets of parameters homogeneously determined and applied them for the synthesis of the HF line, but the scatter observed with the non-homogeneous parameters remained. In an ideal situation, the obvious choice to test F abundances in this open cluster would be to observe solar-type stars, which have better calibrated models, but the 23358 Å HF line is undetectable in these objects. Therefore, more observations of cool stars in several open clusters would help to put our results in some context, since we do not expect to find star-to-star variation of F in open clusters.

The analysis of the binary sample was hampered by the lack of the HF feature in most targets, but offered room to learning. F abundances in binary systems subject to mass transfer are essential to constrain the models of stellar nucleosyhtesis. Despite the lack of well determined F abundances in most of our sample, the measurements of CNO, Na and the s-process element Ce were helpful in comparison with models. In HD 210946, we were able to constrain the upper limit of the initial mass of the former AGB-companion. Combining several elements and F, we may use chemistry to better constrain this parameter in, e.g., F-rich peculiar stars, since the peak of F production is relatively narrow in mass. Also, the comparison of several elements may help to refine other parameters in the models, such as reaction rates. With proper identification of lines from several s-process elements in the IR, we will be able, in the future, to perform a full analysis of chemically peculiar objects in this spectral region alone, with the already known and well documented CNO, F and Na features.

Regarding the methods, we had several problems in the data reduction phase, mostly due to undetectable sky lines. These problems were overcome. Luckly, the DR2 from Gaia was released this year, and this work benefited from Gaia DR2, e.g., in the determination of the non-disc nature of outer 20. The Python code created to optimize the usage of MOOG will be further improved, and, in the near-future, released to the community. Obviously, the work conducted here will be submitted in one or more articles to refereed journals.

It has been four years since I began to work in the area of high-resolution spectroscopy and chemical abundances. After working with optical and IR spectra, with GC and field stars, I assume I am ready to improve my skills in my PhD, mastering different techiniques (e.g., photometry) that will be helpful in the journey to unveil some of the mysteries of the Galaxy.

Bibliography

Abia, C. et al. Fluorine Abundances in Galactic Asymptotic Giant Branch Stars. ApJ, v. 715, p. L94–L98, jun. 2010. Cited in page 30.

Abia, C. et al. The First Fluorine Abundance Determinations in Extragalactic Asymptotic Giant Branch Carbon Stars. ApJ, v. 737, p. L8, ago. 2011. Cited in page 30.

Abia, C. et al. The origin of fluorine: abundances in AGB carbon stars revisited. A&A, v. 581, p. A88, set. 2015. Cited 3 times in pages 30, 31, and 78.

Abia, C. et al. Fluorine in Asymptotic Giant Branch Carbon Stars Revisited. ApJ, v. 694, p. 971–977, abr. 2009. Cited in page 30.

Adams, F. C.; Laughlin, G. A dying universe: the long-term fate and evolutionof astrophysical objects. *Reviews of Modern Physics*, v. 69, p. 337–372, abr. 1997. Cited in page 23.

Aleo, P. D.; Sobotka, A. C.; Ramírez, I. On the Iron Abundance Anomaly in K-dwarf and Hyades Stars. ApJ, v. 846, p. 24, set. 2017. Cited 5 times in pages 69, 72, 85, 88, and 89.

Allen, D. M.; Barbuy, B. Analysis of 26 barium stars. I. Abundances. A&A, v. 454, p. 895–915, ago. 2006. Cited 5 times in pages 69, 90, 98, 99, and 100.

Allen, D. M.; Porto de Mello, G. F. Mn, Cu, and Zn abundances in barium stars and their correlations with neutron capture elements. A&A, v. 525, p. A63, jan. 2011. Cited in page 100.

Alonso, A.; Arribas, S.; Martinez-Roger, C. The empirical scale of temperatures of the low main sequence (F0V-K5V). A&A, v. 313, p. 873–890, set. 1996. Cited 2 times in pages 85 and 88.

Alonso, A.; Arribas, S.; Martinez-Roger, C. Broad-band JHK(L') photometry of a sample of giants with 0.5 $\geq$ [Fe/H] *geq* -3. A&AS, v. 131, p. 209–219, ago. 1998. Cited in page 88.

Alves-Brito, A. et al. CNO and F abundances in the barium star HD 123396. A&A, v. 536, p. A40, dez. 2011. Cited 3 times in pages 30, 34, and 70.

Alves-Brito, A. et al. Chemical similarities between Galactic bulge and local thick disk red giants: O, Na, Mg, Al, Si, Ca, and Ti. A&A, v. 513, p. A35, abr. 2010. Cited 5 times in pages 21, 36, 72, 78, and 101.

Alves-Brito, A. et al. CNO and F abundances in the globular cluster M 22 (NGC 6656). A&A, v. 540, p. A3, abr. 2012. Cited in page 30.

Andrae, R. et al. Gaia Data Release 2. First stellar parameters from Apsis. A&A, v. 616, p. A8, ago. 2018. Cited in page 69.

Andreasen, D. T. et al. Near-infrared spectroscopy of the Sun and HD 20010. Compiling a new line list in the near-infrared. A&A, v. 585, p. A143, jan. 2016. Cited in page 68.

Asplund, M. et al. The Chemical Composition of the Sun. ARA&A, v. 47, p. 481–522, set. 2009. Cited 2 times in pages 25 and 26.

Astraatmadja, T. L.; Bailer-Jones, C. A. L. Estimating Distances from Parallaxes. II. Performance of Bayesian Distance Estimators on a Gaia-like Catalogue. ApJ, v. 832, p. 137, dez. 2016. Cited in page 63.

Astropy Collaboration et al. Astropy: A community Python package for astronomy. *aap*, v. 558, p. A33, out. 2013. Cited in page 58.

Audi, G. et al. The NUBASE evaluation of nuclear and decay properties. *Nuclear Physics A*, v. 729, p. 3–128, dez. 2003. Cited in page 25.

Barbuy, B.; Chiappini, C.; Gerhard, O. Chemodynamical history of the galactic bulge. *Annual Review of Astronomy and Astrophysics*, v. 56, n. 1, p. 223–276, 2018. Disponível em: <https://doi.org/10.1146/annurev-astro-081817-051826>. Cited in page 21.

Barbuy, B. et al. Light element abundances in barium stars. A&A, v. 262, p. 216–228, ago. 1992. Cited 2 times in pages 98 and 99.

Beavers, W. I.; Eitter, J. J. E. W. Fick Observatory stellar radial velocity measurements. I - 1976-1984. ApJS, v. 62, p. 147–228, set. 1986. Cited in page 100.

Beers, T. C.; Christlieb, N. The Discovery and Analysis of Very Metal-Poor Stars in the Galaxy. ARA&A, v. 43, p. 531–580, set. 2005. Cited in page 90.

Bensby, T. et al. The first chemical abundance analysis of K giants in the inner Galactic disc. A&A, v. 516, p. L13, jun. 2010. Cited in page 63.

Bensby, T. et al. A First Constraint on the Thick Disk Scale Length: Differential Radial Abundances in K Giants at Galactocentric Radii 4, 8, and 12 kpc. ApJ, v. 735, p. L46, jul. 2011. Cited 8 times in pages 33, 63, 69, 72, 77, 81, 82, and 83.

Bensby, T.; Feltzing, S.; Oey, M. S. Exploring the Milky Way stellar disk. A detailed elemental abundance study of 714 F and G dwarf stars in the solar neighbourhood. A&A, v. 562, p. A71, fev. 2014. Cited in page 21.

Bidelman, W. P.; Keenan, P. C. The Ba II Stars. ApJ, v. 114, p. 473, nov. 1951. Cited in page 90.

Bionta, R. M. et al. Observation of a neutrino burst in coincidence with supernova 1987A in the Large Magellanic Cloud. *Physical Review Letters*, v. 58, p. 1494–1496, abr. 1987. Cited in page 25.

Bland-Hawthorn, J.; Gerhard, O. The Galaxy in Context: Structural, Kinematic, and Integrated Properties. ARA&A, v. 54, p. 529–596, set. 2016. Cited in page 21.

Bovy, J.; Rix, H.-W.; Hogg, D. W. The Milky Way Has No Distinct Thick Disk. ApJ, v. 751, p. 131, jun. 2012. Cited in page 21.

Brooke, J. S. A. et al. Einstein A Coefficients and Oscillator Strengths for the A $^2\Pi$-X $^2\Sigma^+$ (Red) and B$^2\Sigma^+$-X$^2\Sigma^+$ (Violet) Systems and Rovibrational Transitions in the X $^2\Sigma^+$ State of CN. ApJS, v. 210, p. 23, fev. 2014. Cited in page 70.

Burbidge, E. M. et al. Synthesis of the Elements in Stars. *Reviews of Modern Physics*, v. 29, p. 547–650, 1957. Cited in page 21.

Carpenter, J. M. Color Transformations for the 2MASS Second Incremental Data Release. AJ, v. 121, p. 2851–2871, maio 2001. Cited in page 88.

Carretta, E. et al. Na-O anticorrelation and HB. VII. The chemical composition of first and second-generation stars in 15 globular clusters from GIRAFFE spectra. A&A, v. 505, p. 117–138, out. 2009. Cited in page 82.

Carroll, B. W.; Ostlie, D. A. *An Introduction to Modern Astrophysics*. [S.l.: s.n.], 1996. Cited in page 35.

Castelli, F.; Gratton, R. G.; Kurucz, R. L. Notes on the convection in the ATLAS9 model atmospheres. A&A, v. 318, p. 841–869, fev. 1997. Cited in page 68.

Chabrier, G. Galactic Stellar and Substellar Initial Mass Function. PASP, v. 115, p. 763–795, jul. 2003. Cited in page 23.

Chiappini, C.; Matteucci, F.; Gratton, R. The Chemical Evolution of the Galaxy: The Two-Infall Model. ApJ, v. 477, p. 765–780, mar. 1997. Cited in page 23.

Clayton, D. D. *Principles of stellar evolution and nucleosynthesis*. [S.l.: s.n.], 1983. Cited 2 times in pages 23 and 25.

Coc, A.; Vangioni, E. Primordial nucleosynthesis. *International Journal of Modern Physics E*, v. 26, p. 1741002, 2017. Cited in page 21.

Cohen-Tannoudji, C.; Diu, B.; Laloe, F. *Quantum Mechanics, Volume 2*. [S.l.: s.n.], 1986. 626 p. Cited 2 times in pages 43 and 45.

Cristallo, S. et al. On the Need for the Light Elements Primary Process (LEPP). ApJ, v. 801, p. 53, mar. 2015. Cited in page 31.

Cristallo, S. et al. Effects of nuclear cross sections on ^{19}F nucleosynthesis at low metallicities. A&A, v. 570, p. A46, out. 2014. Cited 3 times in pages 28, 29, and 30.

Cristallo, S. et al. Evolution, Nucleosynthesis, and Yields of Low-Mass Asymptotic Giant Branch Stars at Different Metallicities. ApJ, v. 696, p. 797–820, maio 2009. Cited in page 29.

Crowther, P. A. Physical Properties of Wolf-Rayet Stars. ARA&A, v. 45, p. 177–219, set. 2007. Cited in page 27.

Cunha, K.; Smith, V. V. Fluorine Abundances in the Orion Nebula Cluster. ApJ, v. 626, p. 425–430, jun. 2005. Cited in page 30.

Cunha, K.; Smith, V. V.; Gibson, B. K. Fluorine Abundances in the Milky Way Bulge. ApJ, v. 679, p. L17, maio 2008. Cited in page 30.

Cunha, K. et al. Adding the s-Process Element Cerium to the APOGEE Survey: Identification and Characterization of Ce II Lines in the H-band Spectral Window. ApJ, v. 844, p. 145, ago. 2017. Cited 2 times in pages 70 and 78.

Cunha, K. et al. Fluorine Abundances in the Large Magellanic Cloud and ω Centauri: Evidence for Neutrino Nucleosynthesis? AJ, v. 126, p. 1305–1311, set. 2003. Cited in page 30.

D'Agata, G. et al. Nuclear reactions in AGB nucleosynthesis: the ^{19}F(α, p)^{22}Ne at energies of astrophysical relevance. In: *European Physical Journal Web of Conferences*. [S.l.: s.n.], 2018. (European Physical Journal Web of Conferences, v. 165), p. 01019. Cited in page 30.

de Castro, D. B. et al. Chemical abundances and kinematics of barium stars. MNRAS, v. 459, p. 4299–4324, jul. 2016. Cited 2 times in pages 99 and 100.

Demtröder, W. *Atoms, Molecules and Photons*. Springer Berlin Heidelberg, 2010. Disponível em: <https://www.ebook.de/de/product/19111364/wolfgang_demtroeder_atoms_molecules_and_photons.html>. Cited in page 30.

Drout, M. R. et al. Light curves of the neutron star merger GW170817/SSS17a: Implications for r-process nucleosynthesis. *Science*, v. 358, p. 1570–1574, dez. 2017. Cited in page 21.

Dutra-Ferreira, L. et al. Consistent metallicity scale for cool dwarfs and giants. A benchmark test using the Hyades. A&A, v. 585, p. A75, jan. 2016. Cited in page 87.

Edmunds, M. G.; Greenhow, R. M. General constraints on the effect of gas flows in the chemical evolution of galaxies - II. Radial flows and abundance gradients. MNRAS, v. 272, p. 241–264, jan. 1995. Cited in page 23.

ESA (Ed.). *The HIPPARCOS and TYCHO catalogues. Astrometric and photometric star catalogues derived from the ESA HIPPARCOS Space Astrometry Mission*, v. 1200 de *ESA Special Publication*, (ESA Special Publication, v. 1200). [S.l.: s.n.], 1997. Cited 2 times in pages 65 and 100.

Eversberg, T.; Vollmann, K. *Spectroscopic Instrumentation: Fundamentals and Guidelines for Astronomers*. [S.l.: s.n.], 2015. Cited in page 49.

Famaey, B. et al. Local kinematics of K and M giants from CORAVEL/Hipparcos/Tycho-2 data. Revisiting the concept of superclusters. A&A, v. 430, p. 165–186, jan. 2005. Cited in page 63.

Feltzing, S.; Fohlman, M.; Bensby, T. Manganese trends in a sample of thin and thick disk stars. The origin of Mn. A&A, v. 467, p. 665–677, maio 2007. Cited in page 83.

Fishlock, C. K. et al. Evolution and Nucleosynthesis of Asymptotic Giant Branch Stellar Models of Low Metallicity. ApJ, v. 797, p. 44, dez. 2014. Cited in page 94.

Foreman-Mackey, D. corner.py: Scatterplot matrices in python. *The Journal of Open Source Software*, v. 24, 2016. Disponível em: <http://dx.doi.org/10.5281/zenodo.45906>. Cited in page 65.

Foreman-Mackey, D. et al. emcee: The MCMC Hammer. PASP, v. 125, p. 306, mar. 2013. Cited in page 63.

Frankowski, A.; Jancart, S.; Jorissen, A. Proper-motion binaries in the Hipparcos catalogue. Comparison with radial velocity data. A&A, v. 464, p. 377–392, mar. 2007. Cited in page 101.

Fuhrmann, K. Nearby stars of the Galactic disc and halo - V. MNRAS, v. 414, p. 2893–2922, jul. 2011. Cited in page 21.

Gaia Collaboration et al. Gaia Data Release 2. Summary of the contents and survey properties. A&A, v. 616, p. A1, ago. 2018. Cited 2 times in pages 33 and 63.

Gallino, R. et al. The role of primary ^{16}O as a neutron poison in AGB stars and fluorine primary production at halo metallicities. Mem. Soc. Astron. Italiana, v. 81, p. 998, 2010. Cited in page 29.

Gordon, I. et al. The hitran2016 molecular spectroscopic database. *Journal of Quantitative Spectroscopy and Radiative Transfer*, v. 203, p. 3 – 69, 2017. ISSN 0022-4073. HITRAN2016 Special Issue. Disponível em: <http://www.sciencedirect.com/science/article/pii/S0022407317301073>. Cited in page 70.

Goswami, A. CH stars at high Galactic latitudes. MNRAS, v. 359, p. 531–544, maio 2005. Cited in page 97.

Goswami, A. et al. A high-resolution spectral analysis of three carbon-enhanced metal-poor stars. MNRAS, v. 372, p. 343–356, out. 2006. Cited 3 times in pages 69, 92, and 93.

Goswami, A.; Aoki, W.; Karinkuzhi, D. Subaru/HDS study of CH stars: elemental abundances for stellar neutron-capture process studies. MNRAS, v. 455, p. 402–422, jan. 2016. Cited 3 times in pages 69, 93, and 95.

Gratton, R. G. et al. Abundances of light elements in metal-poor stars. IV. [Fe/O] and [Fe/Mg] ratios and the history of star formation in the solar neighborhood. A&A, v. 358, p. 671–681, jun. 2000. Cited in page 21.

Gray, D. F. *The Observation and Analysis of Stellar Photospheres.* [S.l.: s.n.], 2005. Cited 3 times in pages 35, 49, and 98.

Grevesse, N.; Sauval, A. J. Standard Solar Composition. Space Sci. Rev., v. 85, p. 161–174, maio 1998. Cited in page 25.

Heger, A.; Woosley, S. E.; Spruit, H. C. Presupernova Evolution of Differentially Rotating Massive Stars Including Magnetic Fields. ApJ, v. 626, p. 350–363, jun. 2005. Cited in page 30.

Hinkle, K.; Wallace, L.; Livingston, W. Infrared Atlas of the Arcturus Spectrum, 0.9-5.3 microns. PASP, v. 107, p. 1042, nov. 1995. Cited 2 times in pages 70 and 77.

Hirata, K. et al. Observation of a neutrino burst from the supernova SN1987A. *Physical Review Letters*, v. 58, p. 1490–1493, abr. 1987. Cited in page 25.

Høg, E. et al. The Tycho-2 catalogue of the 2.5 million brightest stars. A&A, v. 355, p. L27–L30, mar. 2000. Cited in page 100.

Hunter, J. D. Matplotlib: A 2d graphics environment. *Computing In Science & Engineering*, IEEE COMPUTER SOC, v. 9, n. 3, p. 90–95, 2007. Disponível em: <http://dx.doi.org/10.1109/MCSE.2007.55>. Cited in page 58.

Indelicato, I. et al. New Improved Indirect Measurement of the ^{19}F(p, α)^{16}O Reaction at Energies of Astrophysical Relevance. ApJ, v. 845, p. 19, ago. 2017. Cited in page 30.

Ito, H. et al. BD+44deg493: A Ninth Magnitude Messenger from the Early Universe; Carbon Enhanced and Beryllium Poor. ApJ, v. 698, p. L37–L41, jun. 2009. Cited 2 times in pages 69 and 91.

Iwamoto, K. et al. Nucleosynthesis in Chandrasekhar Mass Models for Type IA Supernovae and Constraints on Progenitor Systems and Burning-Front Propagation. ApJS, v. 125, p. 439–462, dez. 1999. Cited in page 32.

Johnson, D. R. H.; Soderblom, D. R. Calculating galactic space velocities and their uncertainties, with an application to the Ursa Major group. AJ, v. 93, p. 864–867, abr. 1987. Cited in page 66.

Jones, E. et al. *SciPy: Open source scientific tools for Python*. 2001. [Online; accessed <today>]. Disponível em: <http://www.scipy.org/>. Cited in page 58.

Jönsson, H. et al. Chemical evolution of fluorine in the bulge. High-resolution K-band spectra of giants in three fields. A&A, v. 564, p. A122, abr. 2014. Cited in page 31.

Jönsson, H. et al. Fluorine in the Solar Neighborhood: Is It All Produced in Asymptotic Giant Branch Stars? ApJ, v. 789, p. L41, jul. 2014. Cited 2 times in pages 30 and 31.

Jönsson, H. et al. Fluorine in the Solar Neighborhood: No Evidence for the Neutrino Process. ApJ, v. 835, p. 50, jan. 2017. Cited 10 times in pages 31, 32, 33, 78, 79, 80, 81, 87, 101, and 103.

Jorissen, A. et al. HE 0017+0055: A probable pulsating CEMP-rs star and long-period binary. A&A, v. 586, p. A159, fev. 2016. Cited 2 times in pages 69 and 96.

Jorissen, A.; Smith, V. V.; Lambert, D. L. Fluorine in red giant stars - Evidence for nucleosynthesis. A&A, v. 261, p. 164–187, jul. 1992. Cited 2 times in pages 25 and 30.

Jorissen, A. et al. Binary properties of CH and carbon-enhanced metal-poor stars. A&A, v. 586, p. A158, fev. 2016. Cited 3 times in pages 90, 93, and 95.

Jorissen, A. et al. On metal-deficient barium stars and their link with yellow symbiotic stars. A&A, v. 441, p. 1135–1148, out. 2005. Cited in page 101.

José, J.; Hernanz, M. Nucleosynthesis in Classical Novae: CO versus ONe White Dwarfs. ApJ, v. 494, p. 680–690, fev. 1998. Cited in page 32.

Kaplan, G. H.; Makarov, V. V. Astrometric detection of binary companions and planets: Acceleration of proper motion. *Astronomische Nachrichten*, v. 324, p. 419–424, jul. 2003. Cited in page 100.

Karakas, A. I. Updated stellar yields from asymptotic giant branch models. MNRAS, v. 403, p. 1413–1425, abr. 2010. Cited 3 times in pages 29, 31, and 32.

Karakas, A. I.; Lattanzio, J. C. The Dawes Review 2: Nucleosynthesis and Stellar Yields of Low- and Intermediate-Mass Single Stars. PASA, v. 31, p. e030, jul. 2014. Cited 3 times in pages 27, 29, and 90.

Karakas, A. I.; Lugaro, M. Stellar Yields from Metal-rich Asymptotic Giant Branch Models. ApJ, v. 825, p. 26, jul. 2016. Cited 3 times in pages 29, 98, and 99.

Karttunen, H. et al. *Fundamental Astronomy*. [S.l.: s.n.], 1996. 402 p. Cited in page 92.

Keenan, P. C. The Spectra of CH Stars. ApJ, v. 96, p. 101, jul. 1942. Cited in page 90.

Keenan, P. C.; Keller, G. HD 26-An Unusual High-Velocity Star. ApJ, v. 113, p. 700, maio 1951. Cited in page 93.

Kennedy, C. R. et al. [O/Fe] Estimates for Carbon-enhanced Metal-poor Stars from Near-infrared Spectroscopy. AJ, v. 141, p. 102, mar. 2011. Cited 3 times in pages 69, 96, and 97.

Kippenhahn, R.; Weigert, A. *Stellar Structure and Evolution*. [S.l.: s.n.], 1990. 192 p. Cited in page 27.

Kobayashi, C. et al. Evolution of Fluorine in the Galaxy with the ν-process. ApJ, v. 739, p. L57, out. 2011. Cited 5 times in pages 30, 31, 32, 79, and 80.

Kobayashi, C.; Karakas, A. I.; Umeda, H. The evolution of isotope ratios in the milky way galaxy. *Monthly Notices of the Royal Astronomical Society*, Oxford University Press (OUP), v. 414, n. 4, p. 3231–3250, may 2011. Cited in page 30.

Kobayashi, C. et al. Galactic Chemical Evolution: Carbon through Zinc. ApJ, v. 653, p. 1145–1171, dez. 2006. Cited 2 times in pages 24 and 32.

Korotin, S. A. et al. Grid of theoretical NLTE equivalent widths of four Ba ii lines and barium abundance in cool stars. A&A, v. 581, p. A70, set. 2015. Cited in page 100.

Kramida, A. et al. 2018. NIST Atomic Spectra Database (ver. 5.5.6), [Online]. Available: `https://physics.nist.gov/asd` [2018, August 14]. National Institute of Standards and Technology, Gaithersburg, MD. Cited in page 70.

Kroupa, P. The Local Stellar Initial Mass Function. In: Deiters, S. et al. (Ed.). *Dynamics of Star Clusters and the Milky Way*. [S.l.: s.n.], 2001. (Astronomical Society of the Pacific Conference Series, v. 228), p. 187. Cited 2 times in pages 22 and 23.

Laeter, J. R. de et al. Atomic weights of the elements. review 2000 (IUPAC technical report). *Pure and Applied Chemistry*, Walter de Gruyter GmbH, v. 75, n. 6, p. 683–800, jan 2003. Cited in page 25.

Léna, P. et al. *Observational Astrophysics*. [S.l.: s.n.], 2012. Cited 2 times in pages 49 and 54.

Liang, Y. C. et al. Chemical compositions of four barium stars. A&A, v. 397, p. 257–265, jan. 2003. Cited in page 99.

Lindegren, L. et al. Gaia Data Release 2. The astrometric solution. A&A, v. 616, p. A2, ago. 2018. Cited 2 times in pages 63 and 64.

Linden, S. T. et al. Timing the Evolution of the Galactic Disk with NGC 6791: An Open Cluster with Peculiar High-α Chemistry as Seen by APOGEE. ApJ, v. 842, p. 49, jun. 2017. Cited in page 21.

Liu, F. et al. The Hyades open cluster is chemically inhomogeneous. MNRAS, v. 457, p. 3934–3948, abr. 2016. Cited in page 85.

Liu, G.-Q.; Liang, Y.-C.; Deng, L.-C. Abundance analysis of Barium stars. *Research in Astronomy and Astrophysics*, v. 9, p. 431–448, abr. 2009. Cited 2 times in pages 69 and 99.

Lodders, K.; Palme, H.; Gail, H.-P. Abundances of the Elements in the Solar System. *Landolt Börnstein*, p. 712, 2009. Cited in page 25.

Lucatello, S. et al. Fluorine and Sodium in C-rich Low-metallicity Stars. ApJ, v. 729, p. 40, mar. 2011. Cited 4 times in pages 30, 34, 92, and 93.

Lucatello, S. et al. The Binary Frequency Among Carbon-enhanced, s-Process-rich, Metal-poor Stars. ApJ, v. 625, p. 825–832, jun. 2005. Cited in page 90.

Luck, R. E.; Heiter, U. Giants in the Local Region. AJ, v. 133, p. 2464–2486, jun. 2007. Cited 3 times in pages 69, 78, and 82.

Lugaro, M. et al. The s-process in Asymptotic Giant Branch Stars of Low Metallicity and the Composition of Carbon-enhanced Metal-poor Stars. ApJ, v. 747, p. 2, mar. 2012. Cited 3 times in pages 93, 95, and 96.

Lugaro, M. et al. Reaction Rate Uncertainties and the Production of ^{19}F in Asymptotic Giant Branch Stars. ApJ, v. 615, p. 934–946, nov. 2004. Cited 2 times in pages 29 and 30.

Maiorca, E. et al. A New Solar Fluorine Abundance and a Fluorine Determination in the Two Open Clusters M67 and NGC 6404. ApJ, v. 788, p. 149, jun. 2014. Cited 3 times in pages 25, 26, and 90.

Marchetti, T.; Rossi, E. M.; Brown, A. G. A. Gaia DR2 in 6D: Searching for the fastest stars in the Galaxy. *ArXiv e-prints*, abr. 2018. Cited 3 times in pages 63, 66, and 67.

Marigo, P. et al. A New Generation of PARSEC-COLIBRI Stellar Isochrones Including the TP-AGB Phase. ApJ, v. 835, p. 77, jan. 2017. Cited in page 88.

Masseron, T. et al. A holistic approach to carbon-enhanced metal-poor stars. A&A, v. 509, p. A93, jan. 2010. Cited 4 times in pages 90, 93, 95, and 96.

Matteucci, F. *Chemical Evolution of Galaxies.* [S.l.: s.n.], 2012. Cited 2 times in pages 21 and 22.

Matteucci, F.; Brocato, E. Metallicity distribution and abundance ratios in the stars of the Galactic bulge. ApJ, v. 365, p. 539–543, dez. 1990. Cited in page 24.

McLean, I. S. et al. Design and development of NIRSPEC: a near-infrared echelle spectrograph for the Keck II telescope. In: Fowler, A. M. (Ed.). *Infrared Astronomical Instrumentation.* [S.l.: s.n.], 1998. (Proc. SPIE, v. 3354), p. 566–578. Cited in page 51.

McWilliam, A. Abundance Ratios and Galactic Chemical Evolution. ARA&A, v. 35, p. 503–556, 1997. Cited in page 21.

McWilliam, A. The Chemical Composition of the Galactic Bulge and Implications for its Evolution. PASA, v. 33, p. e040, ago. 2016. Cited 2 times in pages 21 and 24.

Meynet, G.; Arnould, M. Synthesis of ^{19}F in Wolf-Rayet stars. A&A, v. 355, p. 176–180, mar. 2000. Cited 2 times in pages 27 and 32.

Mihalas, D. *Stellar atmospheres.* [S.l.: s.n.], 1970. Cited in page 35.

Morton, D. C. Atomic Data for Resonance Absorption Lines. II. Wavelengths Longward of the Lyman Limit for Heavy Elements. ApJS, v. 130, p. 403–436, out. 2000. Cited in page 60.

Mowlavi, N.; Jorissen, A.; Arnould, M. Fluorine production in intermediate-mass stars. A&A, v. 311, p. 803–816, jul. 1996. Cited in page 29.

Nault, K. A.; Pilachowski, C. A. The Abundance of Fluorine in the Hyades, NGC 752, and M67. AJ, v. 146, p. 153, dez. 2013. Cited 3 times in pages 30, 87, and 90.

Nomoto, K.; Kobayashi, C.; Tominaga, N. Nucleosynthesis in Stars and the Chemical Enrichment of Galaxies. ARA&A, v. 51, p. 457–509, ago. 2013. Cited in page 24.

Nyquist, H. Certain topics in telegraph transmission theory. *Transactions of the American Institute of Electrical Engineers*, Institute of Electrical and Electronics Engineers (IEEE), v. 47, n. 2, p. 617–644, apr 1928. Cited in page 36.

Oliphant, T. E. *Guide to NumPy.* 2nd. ed. USA: CreateSpace Independent Publishing Platform, 2015. ISBN 151730007X, 9781517300074. Cited in page 58.

Palacios, A.; Arnould, M.; Meynet, G. The thermonuclear production of ^{19}F by Wolf-Rayet stars revisited. A&A, v. 443, p. 243–250, nov. 2005. Cited in page 30.

Pancino, E. et al. Chemical abundance analysis of the open clusters Cr 110, NGC 2099 (M 37), NGC 2420, NGC 7789, and M 67 (NGC 2682). A&A, v. 511, p. A56, fev. 2010. Cited in page 69.

Pandey, G. The Discovery of Fluorine in Cool Extreme Helium Stars. ApJ, v. 648, p. L143–L146, set. 2006. Cited in page 30.

Pilachowski, C. A.; Pace, C. The Abundance of Fluorine in Normal G and K Stars of the Galactic Thin Disk. AJ, v. 150, p. 66, set. 2015. Cited 6 times in pages 30, 31, 32, 100, 101, and 104.

Pourbaix, D. et al. S$_{B^9}$: The ninth catalogue of spectroscopic binary orbits. A&A, v. 424, p. 727–732, set. 2004. Cited 2 times in pages 91 and 98.

Price-Whelan, A. M. et al. The Astropy Project: Building an Open-science Project and Status of the v2.0 Core Package. *aj*, v. 156, p. 123, set. 2018. Cited in page 58.

Puls, A. A. et al. Chemical analysis of eight giant stars of the globular cluster NGC 6366. MNRAS, v. 476, p. 690–704, maio 2018. Cited in page 68.

Ramírez, I.; Allende Prieto, C. Fundamental Parameters and Chemical Composition of Arcturus. ApJ, v. 743, p. 135, dez. 2011. Cited 3 times in pages 70, 77, and 83.

Reddy, B. E. et al. The chemical compositions of Galactic disc F and G dwarfs. MNRAS, v. 340, p. 304–340, mar. 2003. Cited in page 83.

Romero, A. D.; Campos, F.; Kepler, S. O. The age-metallicity dependence for white dwarf stars. MNRAS, v. 450, p. 3708–3723, jul. 2015. Cited in page 91.

Rossum, G. *Python Reference Manual*. Amsterdam, The Netherlands, The Netherlands, 1995. Cited in page 58.

Rousselot, P. et al. Night-sky spectral atlas of OH emission lines in the near-infrared. A&A, v. 354, p. 1134–1150, fev. 2000. Cited in page 55.

Ryde, N. et al. Detailed Abundance Analysis of a Metal-poor Giant in the Galactic Center. ApJ, v. 831, p. 40, nov. 2016. Cited in page 70.

Salaris, M.; Cassisi, S. *Evolution of Stars and Stellar Populations*. [S.l.: s.n.], 2005. 400 p. Cited 4 times in pages 23, 24, 27, and 29.

Salpeter, E. E. The Luminosity Function and Stellar Evolution. ApJ, v. 121, p. 161, jan. 1955. Cited 2 times in pages 22 and 23.

Schuler, S. C. et al. Fluorine in a Carbon-enhanced Metal-poor Star. ApJ, v. 667, p. L81–L84, set. 2007. Cited 2 times in pages 30 and 34.

Schuler, S. C. et al. Oxygen from the λ7774 High-Excitation Triplet in Open Cluster Dwarfs: Hyades. ApJ, v. 636, p. 432–444, jan. 2006. Cited 4 times in pages 85, 86, 87, and 89.

Shannon, C. Communication in the presence of noise. *Proceedings of the IRE*, Institute of Electrical and Electronics Engineers (IEEE), v. 37, n. 1, p. 10–21, jan 1949. Cited in page 36.

Shapiro, S. S.; Wilk, M. B. An analysis of variance test for normality (complete samples). *Biometrika*, Oxford University Press (OUP), v. 52, n. 3-4, p. 591–611, dec 1965. Cited in page 78.

Shetrone, M. et al. The SDSS-III APOGEE Spectral Line List for H-band Spectroscopy. ApJS, v. 221, p. 24, dez. 2015. Cited in page 70.

Smiljanic, R.; Porto de Mello, G. F.; da Silva, L. Abundance analysis of barium and mild barium stars. A&A, v. 468, p. 679–693, jun. 2007. Cited in page 100.

Smith, V. V. et al. Fluorine Abundance Variations in Red Giants of the Globular Cluster M4 and Early-Cluster Chemical Pollution. ApJ, v. 633, p. 392–397, nov. 2005. Cited in page 30.

Smith, V. V. et al. Chemical Abundances in Field Red Giants from High-resolution H-band Spectra Using the APOGEE Spectral Linelist. ApJ, v. 765, p. 16, mar. 2013. Cited 5 times in pages 70, 77, 78, 82, and 83.

Sneden, C. The nitrogen abundance of the very metal-poor star HD 122563. ApJ, v. 184, p. 839–849, set. 1973. Cited in page 68.

Sneden, C.; Cowan, J. J.; Gallino, R. Neutron-Capture Elements in the Early Galaxy. ARA&A, v. 46, p. 241–288, set. 2008. Cited in page 92.

Spitoni, E. et al. Fluorine in the solar neighborhood: Chemical evolution models. A&A, v. 612, p. A16, abr. 2018. Cited 4 times in pages 32, 79, 80, and 81.

Starkenburg, E. et al. Binarity in carbon-enhanced metal-poor stars. MNRAS, v. 441, p. 1217–1229, jun. 2014. Cited in page 90.

Takeda, Y. et al. Lithium, Carbon, and Oxygen Abundances of Hyades F-G Type Stars. PASJ, v. 65, p. 53, jun. 2013. Cited 2 times in pages 86 and 87.

Tatum, J. *Stellar Atmospheres*. 2017. Http://orca.phys.uvic.ca/ tatum/stellatm.html. Acessed on 2018.10.24. Cited in page 35.

Tinsley, B. M. Evolution of the Stars and Gas in Galaxies. Fund. Cosmic Phys., v. 5, p. 287–388, 1980. Cited in page 23.

Torres, G. On the Use of Empirical Bolometric Corrections for Stars. AJ, v. 140, p. 1158–1162, nov. 2010. Cited 2 times in pages 70 and 96.

Travaglio, C. et al. Galactic chemical evolution of heavy elements: From barium to europium. *The Astrophysical Journal*, IOP Publishing, v. 521, n. 2, p. 691–702, aug 1999. Cited in page 30.

Udry, S. et al. New CORAVEL spectroscopic-binary orbits of giant barium stars. II. A&AS, v. 131, p. 43–47, jul. 1998. Cited 3 times in pages 97, 99, and 100.

van Altena, W. F. *Astrometry for Astrophysics*. [S.l.: s.n.], 2013. Cited in page 66.

Van Eck, S. et al. More lead stars. A&A, v. 404, p. 291–299, jun. 2003. Cited 2 times in pages 93 and 95.

Vanture, A. D. The CH Stars. I. Carbon Isotrope Ratios. AJ, v. 103, p. 2035, jun. 1992. Cited 2 times in pages 93 and 95.

Vanture, A. D. The CH Stars. II. Carbon, Nitrogen, and Oxygen Abundances. AJ, v. 104, p. 1986, nov. 1992. Cited 2 times in pages 93 and 95.

Vanture, A. D. The CH Stars. III. Heavy Element Abundances. AJ, v. 104, p. 1997–2004, nov. 1992. Cited 2 times in pages 93 and 95.

Wallerstein, G.; Greenstein, J. L. The Chemical Composition of Two CH Stars, HD 26 and HD 201626. ApJ, v. 139, p. 1163, maio 1964. Cited in page 93.

Werner, K.; Rauch, T.; Kruk, J. W. Fluorine in extremely hot post-AGB stars: Evidence for nucleosynthesis. A&A, v. 433, p. 641–645, abr. 2005. Cited in page 30.

Wheeler, J. C.; Sneden, C.; Truran JR., J. W. Abundance ratios as a function of metallicity. ARA&A, v. 27, p. 279–349, 1989. Cited in page 21.

Woolf, V. M.; West, A. A. The M dwarf problem in the Galaxy. MNRAS, v. 422, p. 1489–1494, maio 2012. Cited in page 23.

Woosley, S. E.; Haxton, W. C. Supernova neutrinos, neutral currents and the origin of fluorine. Nature, v. 334, p. 45–47, jul. 1988. Cited in page 25.

Woosley, S. E.; Heger, A.; Weaver, T. A. The evolution and explosion of massive stars. *Reviews of Modern Physics*, v. 74, p. 1015–1071, nov. 2002. Cited in page 24.

Woosley, S. E.; Weaver, T. A. The Evolution and Explosion of Massive Stars. II. Explosive Hydrodynamics and Nucleosynthesis. ApJS, v. 101, p. 181, nov. 1995. Cited in page 24.

Yong, D. et al. Nitrogen Abundances in Giant Stars of the Globular Cluster NGC 6752. ApJ, v. 684, p. 1159–1169, set. 2008. Cited in page 82.

Yong, D. et al. Magnesium Isotope Ratios in Hyades Stars. ApJ, v. 603, p. 697–707, mar. 2004. Cited in page 85.

Yong, D. et al. Chemical Abundances in Giant Stars of the Tidally Disrupted Globular Cluster NGC 6712 from High-Resolution Infrared Spectroscopy. ApJ, v. 689, p. 1020–1030, dez. 2008. Cited in page 30.

Zacs, L. A Spectroscopic Analysis of Barium Stars. A&A, v. 283, p. 937, mar. 1994. Cited in page 100.

Zhang, Y.; Liu, X.-W. Fluorine Abundances in Planetary Nebulae. ApJ, v. 631, p. L61–L64, set. 2005. Cited in page 30.

Appendix

APPENDIX A – Extra tables

A.1 Line-by-line measurements

Table 15 – Line-by-line [X/Fe] abundance measurements, in dex, for the outer disc stars.

Wavelength (Å)	outer1	outer2	outer3	outer16	outer17	outer18	outer19	outer20
OH lines								
15131	···	···	···	0.11	0.19	0.35	0.12	0.29
15278	···	···	···	0.12	0.21	0.32	0.13	0.46
15281	···	···	···	···	···	0.32	···	···
15505	···	···	···	0.03	0.08	0.21	···	0.26
15568	···	···	···	0.07	···	0.35	···	···
15572	···	···	···	0.02	0.08	0.33	···	0.3
15719	···	···	···	···	0.03	0.33	no o48	0.33
15755	···	···	···	0.02	···	0.17	no o48	0.38
15756	···	···	···	···	···	0.20	no o48	0.34
16190	···	···	···	···	0.20	···	···	···
16448	···	···	···	···	···	0.22	-0.04	···
16450	···	···	···	0.10	0.16	0.25	0.03	0.43
16909	···	···	···	0.06	0.12	0.24	···	0.37
C I and CO lines								
15784	···	···	···	-0.24	-0.21	-0.02	···	-0.04
16159	···	···	···	···	-0.22	···	···	···
16831	···	···	···	···	···	···	···	···
16890	···	···	···	-0.18	-0.06	0.09	-0.24	-0.01
23106	···	···	···	-0.27	-0.03	0.12	-0.11	···
23109	···	···	···	-0.24	-0.13	-0.06	-0.16	···
23118	···	···	···	-0.36	0.00	0.07	-0.15	···
23122	···	···	···	-0.27	-0.20	0.01	-0.19	···
23130	···	···	···	-0.34	-0.08	0.04	-0.17	···
23311	···	···	···	-0.28	-0.17	···	···	···
23329	···	···	···	-0.36	-0.11	-0.07	-0.27	···
23351	···	···	···	-0.38	-0.12	0.14	0.11	···
23362	···	···	···	-0.31	-0.11	-0.06	-0.23	···
23367	···	···	···	-0.34	-0.10	-0.05	-0.24	···
CN lines								

Continued on next page

Table 15 – continued

Wavelength	outer1	outer2	outer3	outer16	outer17	outer18	outer19	outer20
15260	···	···	···	0.28	0.06	0.10	0.14	···
15410	···	···	···	0.37	-0.06	···	0.23	···
15447	···	···	···	0.40	0.23	0.12	0.17	0.14
15466	···	···	···	0.43	0.11	0.21	0.18	···
15472	···	···	···	0.30	0.12	0.13	0.18	···
15482	···	···	···	0.36	0.07	0.21	0.19	0.08
15522	···	···	···	0.41	0.14	0.23	0.25	0.08
15563	···	···	···	0.23	0.18	0.24	0.15	···
21806	···	···	···	0.60	0.29	0.28	···	···
21810	···	···	···	0.53	···	···	0.27	···
21826	···	···	···	···	···	0.36	···	···
21847	···	···	···	···	···	···	···	···
21870	···	···	···	0.54	···	0.31	···	···
21948	···	···	···	···	···	···	···	···
22032	···	···	···	0.35	···	0.20	···	···
22075	···	···	···	0.52	···	···	···	···
HF line								
23358	0.03	-0.03	-0.12	-0.26	-0.04	0.03	-0.03	···
Na lines								
22056	0.45	0.45	0.43	···	0.59	0.54	0.78	···
23379	0.38	0.51	0.40	0.34	0.57	0.52	0.74	···
Mg Lines								
15740	···	···	···	-0.01	-0.09	0.14	···	0.48
15748	···	···	···	0.14	0.17	0.27	···	0.42
15765	···	···	···	0.03	-0.06	0.21	···	0.31
15879	···	···	···	0.11	···	0.08	···	···
15886	···	···	···	0.15	···	···	···	···
23328	0.03	0.22	0.09	0.15	0.00	0.22	0.14	···
Al line								
16763	···	···	···	0.20	-0.06	0.25	0.33	···
Si lines								
16060	···	···	···	0.39	0.26	0.40	0.28	0.42
16094	···	···	···	0.39	0.38	0.25	0.33	0.44
16828	···	···	···	···	0.44	0.12	···	0.58
15557	···	···	···	···	0.36	0.20	0.34	0.49
22537	0.27	0.14	0.37	0.26	0.19	0.26	0.35	···
21819	0.15	0.14	0.39	0.43	0.32	0.29	0.36	···
21879	-0.05	0.13	0.42	0.32	0.15	0.28	0.40	···

Continued on next page

Table 15 – continued

Wavelength	outer1	outer2	outer3	outer16	outer17	outer18	outer19	outer20
K lines								
15163	···	···	···	0.06	0.13	0.14	0.32	0.28
15168	···	···	···	0.08	0.19	0.10	0.25	0.26
15772	···	···	···	···	···	···	···	···
Ca lines								
16136	···	···	···	···	0.05	···	0.04	···
16150	···	···	···	-0.14	0.07	0.21	0.08	0.15
16155	···	···	···	···	0.02	0.05	-0.03	0.12
16157	···	···	···	···	0.07	0.26	0.15	···
22626	0.09	0.37	0.33	···	0.16	0.29	0.05	···
Sc lines								
22052	0.00	0.32	0.44	0.19	-0.14	0.36	0.19	···
22065	0.01	0.20	0.17	-0.01	-0.01	0.13	0.07	···
Ti lines								
15543	···	···	···	···	0.12	0.29	0.23	0.54
15602	···	···	···	···	0.03	···	0.19	0.45
22444	0.04	0.40	0.21	0.22	0.20	0.33	0.32	···
22632	···	···	···	···	···	···	···	···
V lines								
15567	···	···	···	···	···	···	···	···
15924	···	···	···	0.01	···	-0.13	···	···
Cr line								
15860	···	···	···	0.11	0.18	0.10	···	0.25
Mn lines								
15159	···	···	···	0.18	0.20	···	0.29	-0.10
15217	···	···	···	0.17	0.08	0.24	0.18	-0.08
15262	···	···	···	0.08	0.02	0.12	0.14	-0.10
Co line								
16757	···	···	···	-0.13	-0.10	-0.06	-0.16	0.05
Ni lines								
15555	···	···	···	···	···	-0.01	···	···
15605	···	···	···	···	0.08	···	0.13	0.21
16584	···	···	···	0.06	0.04	0.03	0.02	0.08
16589	···	···	···	0.05	···	···	0.00	0.01
16815	···	···	···	···	0.05	···	-0.08	···
16818	···	···	···	···	···	···	-0.02	···
16945	···	···	···	···	···	···	···	···
16996	···	···	···	···	···	···	···	···

Continued on next page

Table 15 – continued

Wavelength	outer1	outer2	outer3	outer16	outer17	outer18	outer19	outer20
				Ce Lines				
15277	⋯	⋯	⋯	0.13	0.23	0.00	0.23	⋯
15784	⋯	⋯	⋯	⋯	0.17	0.07	⋯	⋯
15829	⋯	⋯	⋯	0.15	⋯	⋯	⋯	⋯
16595	⋯	⋯	⋯	0.09	0.29	-0.02	0.22	⋯

Table 16 – Line-by-line [X/Fe] abundance measurements, in dex, for the open cluster stars.

Wavelength (Å)	HIP 17766	HIP 21256	HIP 19082	HIP 19316	HIP 21138	M 67 0141	M 67 0223
			OH lines				
15131	0.15	⋯	⋯	⋯	⋯	⋯	⋯
15278	0.17	-0.07	⋯	⋯	⋯	⋯	⋯
15281	⋯	⋯	⋯	⋯	⋯	⋯	⋯
15505	0.13	-0.10	⋯	⋯	⋯	⋯	⋯
15568	⋯	⋯	⋯	⋯	⋯	⋯	⋯
15572	⋯	-0.08	⋯	⋯	⋯	⋯	⋯
15719	0.08	-0.14	⋯	⋯	⋯	⋯	⋯
15755	0.14	-0.12	⋯	⋯	⋯	⋯	⋯
15756	0.12	-0.13	⋯	⋯	⋯	⋯	⋯
16190	⋯	⋯	⋯	⋯	⋯	⋯	⋯
16448	0.08	⋯	⋯	⋯	⋯	⋯	⋯
16450	0.15	-0.11	⋯	⋯	⋯	⋯	⋯
16909	0.18	⋯	⋯	⋯	⋯	⋯	⋯
			C I and CO lines				
15784	0.20	0.11	⋯	⋯	⋯	⋯	⋯
16159	⋯	⋯	⋯	⋯	⋯	⋯	⋯
16831	⋯	⋯	⋯	⋯	⋯	⋯	⋯
16890	⋯	⋯	⋯	⋯	⋯	⋯	⋯
23106	0.28	0.18	⋯	⋯	⋯	⋯	⋯
23109	0.21	⋯	⋯	⋯	⋯	⋯	⋯
23118	0.31	⋯	⋯	⋯	⋯	⋯	⋯
23122	0.30	⋯	⋯	⋯	⋯	⋯	⋯
23130	0.28	0.05	⋯	⋯	⋯	⋯	⋯
23311	⋯	⋯	⋯	⋯	⋯	⋯	⋯
23329	⋯	⋯	⋯	⋯	⋯	⋯	⋯
23351	⋯	⋯	⋯	⋯	⋯	⋯	⋯
23362	0.08	-0.02	⋯	⋯	⋯	⋯	⋯
23367	0.15	-0.05	⋯	⋯	⋯	⋯	⋯
			CN lines				

Continued on next page

Table 16 – continued

Wavelength	HIP 17766	HIP 21256	HIP 19082	HIP 19316	HIP 21138	0141	0223
15260	0.01	-0.13	...	...	...	...	...
15410	0.18	-0.15	...	...	...	...	...
15447	0.11	...	...	...	...	...	...
15466	0.17	0.00	...	...	...	...	...
15472	-0.08	-0.24	...	...	...	...	...
15482	-0.13	-0.37	...	...	...	...	...
15522	...	0.02	...	...	...	...	...
15563	0.06	-0.30	...	...	...	...	...
21806	...	...	...	...	...	...	...
21810	...	...	...	...	...	...	...
21826	...	...	...	...	...	...	...
21847	...	...	...	...	...	...	...
21870	...	...	...	...	...	...	...
21948	...	...	...	...	...	...	...
22032	...	...	...	...	...	...	...
22075	...	...	...	...	...	...	...
			HF line				
23358	0.16	0.17	0.02	0.42	0.17	0.02	...
			Na lines				
22056	...	...	...	...	...	0.32	0.40
23379	...	...	...	...	...	0.38	0.45
			Mg Lines				
15740	...	...	...	...	...	...	...
15748	...	...	...	...	...	...	...
15765	...	...	...	...	...	...	...
15879	...	...	...	...	...	...	...
15886	...	...	...	...	...	...	...
23328	...	...	...	...	...	-0.01	0.00
			Al line				
16173	...	...	...	...	...	...	...
			Si lines				
16060	...	...	...	...	...	...	...
16094	0.26	0.30	...	...	...	...	...
16828	...	0.37	...	...	...	...	...
15557	...	...	...	...	...	...	...
22537	0.28	0.18	...	...	0.17	0.28	0.34
21819	0.28	0.16	0.34	0.45	0.18	0.40	0.35
21879	...	0.13	0.32	0.24	0.06	0.24	0.22
			K lines				
15163	0.10	-0.05	...	...	...	...	...
15168	...	...	...	...	...	...	...
15772	...	...	...	...	...	...	...
			Ca lines				
16136	0.35	0.10	...	...	...	...	...

Continued on next page

Table 16 – continued

Wavelength	HIP 17766	HIP 21256	HIP 19082	HIP 19316	HIP 21138	0141	0223
16150	0.22	0.05	···	···	···	···	···
16155	···	···	···	···	···	···	···
16157	0.23	···	···	···	···	···	···
22626	···	···	0.18	···	···	0.09	0.21
Sc lines							
22052	0.32	0.00	-0.06	···	···	-0.34	-0.09
22065	0.34	0.09	···	···	···	-0.37	-0.01
Ti lines							
15543	···	-0.14	···	···	···	···	···
15602	0.27	···	···	···	···	···	···
22444	0.52	0.22	0.26	0.60	0.39	···	···
22632	0.30	···	-0.17	-0.21	···	···	···
V lines							
15567	···	···	···	···	···	···	···
15924	···	···	···	···	···	···	···
Cr line							
15860	0.32	0.20	···	···	···	···	···
Mn lines							
15159	0.34	0.32	···	···	···	···	···
15217	0.35	0.25	···	···	···	···	···
15262	···	0.20	···	···	···	···	···
Co line							
16757	0.06	···	···	···	···	···	···
Ni lines							
15555	0.38	0.33	···	···	···	···	···
15605	0.21	···	···	···	···	···	···
16584	···	···	···	···	···	···	···
16589	···	···	···	···	···	···	···
16815	···	···	···	···	···	···	···
16818	···	···	···	···	···	···	···
16945	···	···	···	···	···	···	···
16996	···	···	···	···	···	···	···
Ce Lines							
15277	···	···	···	···	···	···	···
15784	···	···	···	···	···	···	···
15829	···	···	···	···	···	···	···
16595	···	···	···	···	···	···	···

Table 17 – Line-by-line [X/Fe] abundance measurements, in dex, for the peculiar stars.

Wave-length (Å)	HR 8878	HD 210946	HD 5424	HD 5223	HD 27271	HD 26	HE 0017 +0055	HE 0310 +0059	HE 0002 +0053	HD 224959
OH lines										
15131	0.63	···	···	···	···	···	···	···	···	···
15278	0.60	···	···	···	···	···	···	···	···	···
15281	0.55	-0.07	···	···	···	0.34	···	···	···	···
15505	0.53	-0.17	···	···	···	···	···	···	···	0.54
15568	0.58	···	···	···	···	···	···	···	···	···
15572	0.51	-0.27	···	0.92	···	···	···	···	···	···
15719	···	···	···	···	···	···	···	···	···	···
15755	···	···	···	···	···	···	···	···	···	···
15756	···	···	···	···	···	···	···	···	···	···
16190	···	···	···	···	···	···	···	···	···	···
16448	···	···	···	···	···	···	···	···	···	···
16450	···	···	···	···	···	···	···	···	···	···
16909	···	···	···	···	···	···	0.87	···	···	···
C I and CO lines										
15784	0.17	-0.28	···	···	···	0.38	···	···	···	2.16
16159	···	···	···	···	···	···	···	···	···	···
16831	···	···	···	···	···	···	···	···	···	···
16890	···	0.09	···	···	-0.28	···	···	···	···	2.30
23106	···	-0.14	···	-0.31	···	···	0.87	···	···	···
23109	···	-0.15	···	-0.35	···	···	···	···	···	···
23118	···	-0.19	···	0.79	-0.37	0.88	···	0.92	···	···
23122	0.17	-0.17	···	1.01	···	0.57	···	···	···	···
23130	0.28	-0.19	···	0.72	-0.38	0.87	···	0.92	···	···
23311	0.10	···	···	1.01	···	···	···	0.92	···	···
23329	0.03	···	···	0.85	···	···	···	0.79	···	···
23351	0.18	0.20	···	0.92	-0.39	0.87	1.97	0.93	···	···
23362	0.11	-0.11	···	0.90	-0.36	0.88	···	0.95	1.10	···
23367	0.20	-0.16	···	0.92	-0.40	0.80	···	0.90	1.41	···
CN lines										
15260	···	0.21	···	···	0.07	···	···	···	···	2.00
15410	···	···	···	1.09	0.13	0.63	···	···	···	2.00
15447	···	0.29	···	···	0.30	0.57	···	···	···	···
15466	···	0.29	···	1.19	0.29	0.56	···	···	···	1.93
15472	···	0.32	···	0.85	0.35	0.67	···	···	···	···
15482	···	···	···	0.92	0.33	0.56	···	···	···	1.99
15522	···	0.27	···	1.03	0.16	···	···	···	···	···
15563	···	0.36	···	1.08	0.27	0.53	···	···	···	2.00
21806	···	0.37	···	···	0.42	···	···	1.48	···	···
21810	···	···	···	···	···	···	···	1.41	···	2.12

Continued on next page

Table 17 – continued

Wave-length	HR 8878	HD 210946	HD 5424	HD 5223	HD 27271	HD 26	HE 0017 +0055	HE 0310 +0059	HE 0002 +0053	HD 224959
21826	···	0.28	···	···	···	···	···	···	1.94	2.14
21847	···	···	···	···	···	0.85	···	···	···	···
21870	0.32	0.34	···	···	···	···	···	1.46	···	2.06
21948	···	0.54	···	···	···	···	···	···	···	···
22032	···	···	···	···	···	···	···	1.40	···	···
22075	···	0.53	···	···	···	···	···	1.48	···	···
HF line										
23358	0.10	···	···	1.42	···	···	0.57	···	···	···
Na lines										
22056	0.25	0.14	0.71	···	0.32	0.29	···	2.30	···	···
23379	0.21	0.12	0.59	0.41	0.47	0.33	···	2.24	···	···
Mg Lines										
15740	0.21	-0.12	···	0.43	···	···	···	···	···	···
15748	···	-0.07	···	···	···	···	···	···	···	···
15765	0.28	-0.17	···	0.50	-0.11	0.59	···	···	···	0.68
15879	···	···	···	···	···	···	···	···	···	···
15886	···	···	···	···	···	···	···	···	···	···
23328	···	-0.06	···	···	-0.08	···	···	···	···	···
Al line										
16763	···	0.03	···	0.07	-0.09	0.32	···	···	···	···
Si lines										
16060	···	0.22	···	0.55	0.09	0.62	···	···	···	···
16094	···	0.20	···	0.39	0.17	0.65	···	···	···	0.85
16828	···	0.16	···	0.65	0.06	0.47	···	···	···	···
15557	0.42	0.09	···	···	···	0.30	···	···	···	0.58
22537	0.26	0.27	0.08	0.67	0.31	0.44	···	1.15	···	···
21819	0.38	0.25	0.47	···	0.22	0.44	···	1.32	···	···
21879	0.22	0.34	···	···	0.30	0.46	···	···	···	···
K lines										
15163	0.22	0.21	···	-0.09	-0.09	0.54	···	···	···	···
15168	0.06	0.02	···	···	-0.11	···	···	···	···	···
15772	···	···	···	-0.09	-0.10	0.54	···	···	···	···
Ca lines										
16136	···	-0.15	···	···	···	···	···	···	···	···
16150	···	-0.21	···	···	-0.17	0.41	···	···	···	···
16155	···	···	···	0.77	-0.24	···	···	···	···	···
16157	···	···	···	···	-0.16	···	···	···	···	···
22626	0.46	0.12	0.49	···	0.03	···	···	···	···	···
Sc lines										
22052	···	···	···	···	···	···	···	···	···	···
22065	···	···	···	···	···	···	···	···	···	···
Ti lines										
15543	0.63	-0.43	···	···	-0.42	0.06	···	···	···	···

Continued on next page

Table 17 – continued

Wave-length	HR 8878	HD 210946	HD 5424	HD 5223	HD 27271	HD 26	HE 0017 +0055	HE 0310 +0059	HE 0002 +0053	HD 224959
15602	…	…	…	…	-0.33	…	…	…	…	…
22444	…	…	…	…	…	…	…	1.42	…	…
22632	0.61	…	…	…	…	…	…	…	…	…
V lines										
15567	…	…	…	…	…	…	…	…	…	…
15924	…	…	…	…	…	…	…	…	…	…
Cr line										
15860	-0.01	0.04	…	…	-0.11	…	…	…	…	…
Mn lines										
15159	-0.06	0.18	…	-0.13	-0.27	0.33	…	…	…	…
15217	0.08	-0.06	…	…	-0.16	0.12	…	…	…	…
15262	0.01	0.00	…	-0.56	-0.03	…	…	…	…	…
Co line										
16757	…	-0.19	…	…	-0.45	…	…	…	…	…
Ni lines										
15555	…	…	…	…	-0.27	…	…	…	…	…
15605	…	…	…	…	-0.25	…	…	…	…	…
16584	…	-0.10	…	…	-0.28	…	…	…	…	…
16589	…	0.00	…	…	-0.19	…	…	…	…	…
16815	…	…	…	…	-0.35	…	…	…	…	…
16818	…	-0.05	…	…	…	…	…	…	…	…
16945	…	…	…	…	…	…	…	…	…	…
16996	…	…	…	…	…	…	…	…	…	…
Ce Lines										
15277	-0.03	0.56	…	…	-0.02	1.56	…	…	…	2.21
15784	…	0.72	…	1.72	0.16	1.39	…	…	…	2.30
15829	…	0.40	…	…	0.13	1.48	…	…	…	2.16
16595	…	0.51	…	1.59	0.15	1.46	…	…	…	…

Table 18 – Line-by-line [X/Fe] abundance measurements, in dex, for Arcturus and μ Leo.

Wavelength (Å)	Arcturus	μ Leo
OH lines		
15131	0.40	…
15278	0.38	…
15281	0.39	…
15505	0.30	-0.02
15568	0.37	0.16
15572	0.35	…

Continued on next page

Table 18 – continued

Wavelength	Arcturus	μ Leo
15719	0.35	···
15755	0.31	···
15756	0.31	···
16190	0.33	···
16448	0.31	···
16450	0.30	0.04
16909	0.28	0.20
C I and CO lines		
15784	0.10	···
16159	0.02	···
16831	0.14	···
16890	0.09	-0.11
23106	0.13	···
23109	0.05	···
23118	0.10	···
23122	0.07	···
23130	0.12	···
23311	0.09	···
23329	0.05	···
23351	0.14	···
23362	0.05	···
23367	0.11	···
CN lines		
15260	-0.03	0.37
15410	0.05	0.59
15447	···	···
15466	0.06	···
15472	0.08	0.67
15482	0.04	0.55
15522	-0.17	0.59
15563	0.11	0.50
21806	0.01	···
21810	···	···
21826	-0.02	···
21847	···	···
21870	···	···
21948	0.22	···
22032	0.14	···
22075	0.14	···
HF line		
23358	-0.16	···
Na lines		
22056	···	···
23379	0.17	···

Continued on next page

Table 18 – continued

Wavelength	Arcturus	μ Leo
Mg Lines		
15740	···	···
15748	···	···
15765	···	···
15879	0.34	···
15886	0.45	···
23328	0.28	···
Al line		
16763	0.28	0.11
Si lines		
16060	0.37	-0.01
16094	0.33	0.05
16828	0.36	0.13
15557	0.38	0.18
22537	0.29	···
21819	0.36	···
21879	0.22	···
K lines		
15163	···	0.04
15168	0.20	0.05
15772	···	···
Ca lines		
16136	···	···
16150	0.12	-0.11
16155	0.06	-0.07
16157	0.16	···
22626	0.26	···
Sc lines		
22052	0.15	···
22065	0.15	···
Ti lines		
15543	0.23	0.02
15602	0.28	0.19
22444	0.38	···
22632	0.25	···
V lines		
15567	···	···
15924	0.12	···
Cr line		
15860	0.03	···
Mn lines		
15159	-0.07	0.22
15217	-0.04	0.40

Continued on next page

Table 18 – continued

Wavelength	Arcturus	μ Leo
15262	-0.10	0.57
Co line		
16757	0.09	-0.02
Ni lines		
15605	0.09	⋯
16584	0.07	0.20
16589	⋯	⋯
16815	0.01	-0.02
16818	0.00	⋯
16945	0.04	⋯
16996	0.06	⋯
Ce Lines		
15277	-0.27	-0.45
15784	-0.14	⋯
15829	-0.25	⋯
16595	⋯	-0.25

A.2 Other

Table 19 – Observed spectral intervals.

Order	λ_{min} (Å)	λ_{max} (Å)
53	14245	14445
52	14520	14720
51	14800	15000
50	15090	15300
49	15400	15615
48	15720	15930
47	16050	16270
46	16400	16625
45	16750	17000
36	21200	21470
35	21800	22080
34	22430	22730
33	23100	23400
32	23830	24125
31	24600	24900